Molecular and Developmental Asymmetries of Vertebrate Anterior Somites

HARVARD
Kenneth C. Griffin

GRADUATE SCHOOL
OF ARTS AND SCIENCES

THESIS ACCEPTANCE CERTIFICATE

The undersigned, appointed by the
Division of Medical Sciences

in the subject of Biological and Biomedical Sciences

have examined a dissertation entitled

Molecular and Developmental Asymmetries of Vertebrate Anterior Somites

presented by Jong Gwan Lee

candidate for the degree of Doctor of Philosophy and hereby certify that it is worthy of acceptance.

Signature: Matthew Harris (May 4, 2026 17:19:50 EDT)

Typed Name: Dr. Matthew Harris

Signature: MArcos Simoes-Costa (May 5, 2026 14:22:01 EDT)

Typed Name: Dr. Marcos Simoes-Costa

Signature: DTGrimes (May 5, 2026 13:32:00 PDT)

Typed Name: Dr. Daniel Grimes

Signature: Natasza Kurpios (May 8, 2026 09:32:18 EDT)

Typed Name: Dr. Natasza Kurpios

Date: May 04, 2026

Molecular and Developmental Asymmetries of Vertebrate Anterior Somites

A dissertation presented by

Jong Gwan Lee

to

The Division of Medical Sciences

in partial fulfillment of the requirements for the degree of

Doctor of Philosophy

in the subject of

Biological and Biomedical Sciences

Harvard University

Cambridge, Massachusetts

May 2026

Dissertation Advisor: Olivier Pourquié Jong Gwan Lee

Molecular and Developmental Asymmetries of Vertebrate Anterior Somites

Abstract:

Bilateral symmetry is a conserved characteristic of most animal body plans. In vertebrates, it is especially apparent in the musculoskeletal system and its embryonic precursor, the somites, in contrast to the asymmetric visceral organs. Traditionally, research on left-right (LR) asymmetry has focused on initial symmetry breaking events at the embryonic organizer and on the transfer and amplification of LR determining signaling cascades in the lateral plate mesoderm (LPM). By contrast, the paraxial mesoderm, including the somites, has been largely overlooked, as somite bilateral symmetry has been assumed to be the default state. Although recent studies suggest that somitogenesis occurs in the context of multiple sources of asymmetry, whether somites are truly symmetric, and to what extent, have remained unclear. To address this question, I characterized morphological and gene expression asymmetries in the early chick embryo. Left somites were larger and more anteriorly positioned than right somites, and gene expression underlying somitogenesis showed corresponding asymmetries. Experiments examining segmentation clock gene oscillation using the chick embryo and in vitro human cell model identified LR patterning signals, particularly NODAL, as a cause of this asymmetry. In addition, gene expression analyses and single-cell RNA sequencing uncovered a previously unrecognized molecular asymmetry of somites. The lateral parts of anterior somites express *NODAL* and an array of novel LR asymmetric genes. Leveraging this discovery, I examined developmental asymmetry of the anterior somites using GFP somite grafting and electroporation.

These approaches revealed a striking contribution of somites to the heart and showed that somite molecular laterality is important for proper cardiac development. Together, these findings provide a comprehensive characterization of morphological, molecular, and developmental asymmetries of somites, demonstrate robust directional asymmetry in the paraxial mesoderm, and expand the scope of LR asymmetry research beyond its traditional focus of tissues and genes.

Table of Contents

Acknowledgements

First, I would like to thank my PhD advisor Olivier Pourquié for giving me the opportunity to pursue my doctoral research with extraordinary patience and generosity. He taught me how to view biology and ask intriguing questions as an embryologist. He gave me right amount of freedom to explore unusual questions and build the project. At the same time, whenever I was disoriented about the next step and frustrated by the failures in the lab, his knowledge, insight, vision, and optimism repeatedly made me feel secure and helped me find the right path forward. I am especially grateful that his mentorship extended beyond discussions in the office. Some of the most memorable lessons and guidance came in the chicken room, where he showed me embryological manipulations that I was initially doubtful, but that became convincing and inspiring as I learned and thought through them alongside him.

Next, I want to thank my DAC committee members, Dr. Cliff Tabin, Dr. Matthew Harris, and Dr. Sean Megason, for their support and feedback for my project at the meetings. I would like to especially acknowledge the committee chair Dr. Cliff Tabin who not only provided me with an opportunity to rotate in his lab but also is the leader and pioneer of the topic on which my PhD project was built. His advice, support, and presence were deeply meaningful to my PhD journey. Also, I would like to thank Dr. Matthew Harris, who also provided me with an opportunity to rotate in his lab. The rotation lasted a short period of time, but I felt understood. His support, encouragement, and guidance continued throughout my PhD, which I sincerely appreciated and kept me moving forward.

I would also like to thank all the members of the Pourquié lab, past and present, for providing not only scientific support, advice, and feedback, but also a sense of home, friendship, and community. Throughout my PhD, especially during times when I felt lost and discouraged,

they were exceedingly generous with their time, encouragement, and emotional support. Their kindness repeatedly helped me regain perspective and reminded me that I was moving in the right direction. I would like to thank Charlene, who guided me during my rotation in the lab. Even though it was a virtual rotation during COVID lockdown, her kindness and enthusiasm convinced me that I wanted to join the lab. After I joined, she taught me the basics of chicken embryology, which I ended up using throughout my PhD. I would also like to thank Alessandro, who taught me so much about chick embryo work as well and gave me substantial advice in pursuing my PhD research, in addition to being a great friend and a role model. I drew a great deal of scientific inspiration and motivation from him for his passion and knowledge and was able to realize my own scientific interest, which resonated with his. I also deeply appreciate his continued friendly support, advice, and check-ins even after he left the lab. I would like to thank Kana, with whom I could discuss the questions of left-right asymmetry and develop directions of my own projects. I am also grateful to Clement, who consistently helped me see beyond my own pessimism. His support, reassurance, and patience meant a lot to me. I would like to thank Jake for his support as well and helping me get started with in vitro system. I thank Alex for inviting me to poker nights and other gatherings, which I very much enjoyed. I would also like to thank Yuchuan. Collaboration with him gave me much inspiration on how to move forward with my project. I am deeply grateful to Kongju, who is not only an amazing scientist full of knowledge, ideas, and passion, but also one of the most generous people I have met. I took far more of his time and energy than I deserve, yet he was always patient, understanding, and willing to listen to my worries and complaints. I only aspire to be like him to other people I will meet in the future. Finally, I would like to thank Ségolène, who joined the lab at exactly the right moment and brought exactly the right expertise to the lab. Whenever I was unsure how to proceed, she

supported me with her knowledge, kindness and optimism. Thanks to her, I was able to do many things in this project that I could not do on my own.

I would also like to acknowledge graduate students in the lab. I am grateful to Margarete, who generously shared her experience and advice as a senior graduate student in the lab. I was inspired not only by her achievement, drive, and vision but also by her kindness and friendliness. I would also like to thank Andrew, who helped me tremendously with coding and various data analyses. I really enjoyed game nights at Andrew's place and being able to chat with him in the lab about science, graduate school life, personal life, career, and many other things. I am also grateful to Alejandra. Both as international students, we ended up having very similar timeline from the beginning to the end of PhD, and I got so much help from her throughout PhD and, especially near the end, so much information and support for finishing PhD. Also, I would like to thank Matthew. As we were sitting next to each other, I had a lot of fun in the lab, as we were chatting about random news, investing, movies, and everything. Also, I learned a lot from the way he approaches the project, graduate school, and career.

I would like to thank my scientific advisors and mentors at Duke University. First, I would like to thank Dr. Blanche Capel for giving me an opportunity to do research in her lab. When I got initially intrigued by developmental biology at Duke, thanks to her, I was able to learn about it in one of the most creative and warm environments. I found her mentoring and approach to developmental biology and evolution truly inspirational, which reinforced my interest in research. My experience in her lab was critical for developing an idea of pursuing PhD in developmental biology. Also, I would like to thank Ceri and Corey, who introduced me to the lab, guided my research project, and gave me a lot of advice on graduate schools. Next, I would like to thank Dr. David McClay. I first became fascinated by embryos in his classes and realized

that I wanted to pursue research in developmental biology. His passion was highly contagious and shaped my own enthusiasm for embryology. I also thank Dr. Douglas Boyer. In his lab, working with 3D anatomical structures helped me cultivate my interest in shapes and morphogenesis. I am also deeply grateful for the sense of home he created by welcoming us during the holidays. In addition, I cherish the unforgettable times during the research trips in the fields of Wyoming and Montana, which critically impacted my thoughts on career and research. Lastly, I would like to thank Dr. Dan McShea. When I had only a vague interest in evolutionary biology by reading Stephen Jay Gould during my military service, I felt that I had met exactly the right mentor who truly understood me. He shaped the way I think about science, as he taught me how to think about concepts and turn them into testable hypotheses and exciting projects. I really enjoyed and learned a lot from our weekly meetings, where we discussed my projects, biology, philosophy, career, and life. He guided me with immeasurable patience and kindness, and that has become a standard I aspire to carry with me.

I would like to thank my parents for always being supportive and understanding of me. They significantly helped me stay positive and motivated throughout my PhD. I suppose that my motivation to pursue PhD was deeply influenced by my parents both consciously and unconsciously, and I am grateful for it.

Lastly, I want to thank my wife, the love of my life, Olivia. We met in my second year, since then she has been my best friend and the biggest supporter. When I didn't believe in myself, she was the one who believed in me and eventually changed me. I cannot imagine what I would be able to do without her support. She has been incredibly understanding of my irregular daily and weekly schedules, of my constant need to go to lab when she traveled for hours from New Jersey or Pennsylvania to visit me, and of unexpected situations as a graduate student that

led to cancelling our vacation plan. Our daily phone calls on my way back home and monthly visits to each other were something that allowed me to move forward and make it through every day. I feel incredibly fortunate and grateful that she came into my life.

Chapter 1

Introduction

Part 1. Development of the paraxial mesoderm

Overview of somites and their derivatives

Vertebrate bodies are organized as sequences of segmented structures along the anteroposterior axis. For instance, the axial skeleton is composed of a series of anatomical building blocks, including vertebrae and ribs, with attached soft tissue that is also segmented, such as ligaments, tendons, nerves, and muscles (1,2). During embryonic development, segmental organization is initially observed in the somites, bilateral columns of epithelial structures that flank the midline along the anteroposterior axis. Over development, signaling inputs from surrounding tissues drive the spatial and molecular compartmentalization of somites, which later give rise to different lineages including back dermis, skeletal muscles, bones, cartilages, and tendons. In addition to being embryonic precursors of the musculoskeletal system, somites establish a structural foundation for the development of other major organs, upon which the vasculature and the peripheral nervous system are stereotypically arranged across axial levels of somites (1–3). In this way, somites represent an embodiment of a fundamental design principle of the vertebrate body, where a segmented body plan emerges from a simple continuous embryo.

Embryonically, somites are a part of the paraxial mesoderm, which lies between the midline (neural tube and notochord) and the lateral plate mesoderm. Within the paraxial mesoderm, the anterior-most region is called the head mesoderm, which contributes to craniofacial muscles and whose segmentation has been debated (4,5). Posterior to the head mesoderm, bilateral sequences of somite pairs extend from the level of the hindbrain to the anterior end of the presomitic mesoderm (PSM), an unsegmented, mesenchymal, and posterior part of the paraxial mesoderm that gives rise to nascent somites.

Somites have long fascinated biologists for their dynamic formation process. While the embryonic axis elongates, a new pair of epithelial somites is sequentially formed from the anterior tip of the mesenchymal paraxial mesoderm with striking periodicity, progressing from head to tail. To explain this rhythmicity, theoretical models such as the "clock-and-wavefront model" were proposed prior to the discovery of the molecular components constituting such a model (6). Since the discovery of the core segmentation clock gene cHairy1 in the chick embryo about 30 years ago, advancements in genetic and molecular tools for both embryo and in vitro models have prompted an explosion of discoveries on the molecular and cellular mechanisms of somitogenesis, revealing the general design principle in biology that confers dynamic spatiotemporal patterns and translates them into robust structural organization (7).

In this chapter, I will describe the molecular and cellular processes underlying somitogenesis and the patterning within the somite and consequent compartmentalization leading to differentiation towards different lineages, with additional emphasis on the unique features of the anterior-most somites.

Gastrulation and the formation of different mesoderm lineages in the chick embryo

Gastrulation is a process through which pluripotent epiblast cells are segregated into three main germ layers: ectoderm, mesoderm, and endoderm. In the chick embryo, the ingression of cells primarily occurs through the structure called the primitive streak, an elongated furrow in the dorsal epiblast. The primitive streak is a transient and dynamic structure that evolves over the earliest phases of embryonic development. At around Hamburger-Hamilton (HH) stage 2-3, the early primitive streak marks the future anteroposterior axis of the developing embryo (8–10). Epiblast cells at each side of the primitive streak participate in a collective, bilaterally symmetric, counter-rotating vortex-like movement called the "polonaise movement" that leads to the

formation and elongation of the primitive streak that reaches its full extent at HH4. The anterior end of the primitive streak is an embryonic organizer called Hensen's node (HN), which functions as a signaling center that can induce an embryonic axis when grafted elsewhere (11–13). As epiblast cells ingress through the primitive streak, undergoing epithelial-to-mesenchymal transition (EMT), the AP level at which the cells ingress dictates their fate across the mediolateral axis (14,15). For instance, the most anterior primitive streak cells (e.g., cells at HN) correspond to the most axial structures such as the notochord and neural tissue and the progressively posterior primitive streak cells correspond to the paraxial mesoderm, intermediate mesoderm, lateral plate mesoderm, and extraembryonic tissue, respectively. As HN functions as a signaling center, multiple AP signaling gradients underlie the migration and segregation of mesodermal fates (9,16,17). Cells participating in the paraxial mesoderm and ultimately the somites can be found at the anterior region of the primitive streak (15).

At HH5, HN regresses posteriorly leading to shortening of the primitive streak, while accompanying the elongation of the notochord at its regressing path (14,17,18). Throughout early embryonic development, the primitive streak eventually resolves, and the posterior end of the trunk forms a new organizing center with stem-cell-like properties called the tailbud at around HH13-14 (19,20). After this stage, the tailbud becomes the primary source of nascent cells feeding into the elongating body axis.

The paraxial mesoderm lies between the ectoderm (dorsal) and endoderm (ventral), and between the neural tube and notochord (medial) and the intermediate mesoderm and lateral plate mesoderm (lateral). These mesoderm lineages express distinct transcriptional markers and participate in distinct lineages (21,22). For instance, the lateral plate mesoderm contributes to the heart, vasculature, limbs, and various other musculoskeletal structures, and the intermediate

mesoderm contributes to the urogenital system including the gonads and kidneys. The anterior most part of the paraxial mesoderm corresponds to the head mesoderm that gives rise to craniofacial muscles and skull (23,24). Posterior to the head mesoderm lie the sequences of somites, and more posteriorly the unsegmented posterior paraxial mesoderm that later undergoes mesenchymal-to-epithelial transition (MET) to form somites is called the presomitic mesoderm (PSM). Somites give rise to the majority of the musculoskeletal system including vertebrae and ribs, muscles, and back dermis. Somites along the AP axis expresses unique Hox code and undergoes corresponding developmental trajectories, so they are described as occipital, cervical, thoracic, lumbar, sacral, and caudal somites from anterior to posterior (2). The total number of somites and their subdivisions vary across species—approximately 31 in zebrafish, 42-44 in human, 55 in chicken, 65 in mouse, and over 300 in some snake species—representing the remarkable evolvability and modularity of the paraxial mesoderm (25,26).

Somite patterning by the "clock and wavefront" model

A new pair of epithelial somites buds off from the anterior tip of the mesenchymal presomitic mesoderm with a periodicity that differs across species—e.g., 30min in zebrafish, 1.5hr in chicken, 2hr in mouse, and 5hr in human. Before the discovery of the molecular components underlying somitogenesis, theoretical models explaining this striking periodicity were proposed, and the "clock-and-wavefront" model remains the most influential one (6) (**Fig.1.1**). It was posited that the presomitic mesoderm goes through oscillatory phases that confer the capacity to form epithelial somites ("clock"), with a slowly regressing front of maturation where cells can trigger changes in cell state to form a new pair of somites ("wavefront"). As the molecular identities of the key components of somitogenesis are

continuously discovered, the "clock-and-wavefront" model has also been updated as an evolving paradigm to interpret the role of newly identified molecular regulators.

Oscillating signaling pathways in the PSM

The first evidence for a molecular clock underlying somitogenesis was discovered in the chick embryo. Palmeirim and colleagues (7) observed dynamic expression patterns of *c-hairy1*—a homolog of Drosophila hairy known to be a pair-rule gene necessary for segmentation of the fly—in the PSM of the chick embryo. *c-hairy1* exhibited cyclic expression patterns, with an initially broad posterior domain that progressively refined as it traveled anteriorly (**Fig.1.1**). This "traveling wave" of *c-hairy1* is arrested at the level of the newly forming somite while simultaneously the next cycle's broad posterior band emerges. The periods of cyclic expression matched the period of new somite formation, suggesting that *c-hairy1* is indeed the "clock". In addition, they further demonstrated that the waves do not result from cells traveling anteriorly and are independent of the presence of the posterior part of PSM. These experiments revealed that these waves are "kinematic", meaning that these waves emerge from the endogenous program of PSM cells expressing *c-hairy1* in a cyclic manner.

Following works in different vertebrate species such as zebrafish and mouse showed that the members of the Hairy/enhancer of split family (*Hes/Her/Hairy*) are indeed the most conserved core cyclic genes (27,28). Genetic ablation of these genes resulted in disruption in somitogenesis in zebrafish and mouse, validating their functional significance (29). They are a family of basic helix-loop-helix (bHLH) transcription factors that are downstream targets of the Notch signaling pathway and act as repressors of their own transcription (3). This motif of a negative feedback loop underlies the basis of clock gene oscillation. The short half-life of these

factors and the time delay required for their transcription, splicing and processing, translation, nuclear transport, and accumulation to finally act as transcriptional repressors together play an important role in preventing the system from entering a steady state and ensuring the emergence of oscillations (30–32). The half-life and time delay are unique features of different species that contribute to species-specific oscillation periods (33–36). Further studies showed that other Notch pathway genes also exhibit cyclic expression patterns. For instance, Lunatic Fringe (*Lfng*)—a glycosyltransferase enzyme that modifies the Notch receptor—and Delta-like (*Dll*) ligands of the Notch signaling pathway are other examples of oscillatory Notch components that play a critical role in Notch modulation and are regulated by negative feedback loops (37–39).

Additionally, although different species exhibit different sets of cyclic genes, components of the Wnt (e.g., *Axin2*, *Dkk1*) and FGF (phospho-ERK, *Dusp*, *Spry*) signaling pathways have been shown to oscillate in amniotes (40). Like the *Hes* family, these proteins share the motif of being downstream targets and inhibitors of their respective signaling pathways, thus establishing a negative feedback loop. Interestingly, in the posterior PSM, the oscillations of Notch and FGF components are in-phase but out of phase with the Wnt pathway, suggesting coordinated crosstalk across signaling pathways (40–42). However, the precise network topology and/or the identity of the "pacemaker" or "core oscillator" of these signaling pathways remain unclear and are active areas of research. For instance, both FGF and Notch pathways activate *Hes7*, which in turn represses the transcription of FGF effectors (e.g., *Dusp*), Notch effectors (e.g., *Lfng*) and itself (43). Similarly, pulses of Notch inhibition have been shown to entrain *Axin2* oscillation (42). However, various findings suggest significant complexity in such a signaling network. For example, *Axin2* oscillation at the single cell level continues despite mutations in *Hes7* or *Dll1*, or constitutive expression of NICD although the dynamic pattern at the tissue level is disrupted

(31,41,44). Even within the Wnt pathway, the true nature of oscillation is unclear because t oscillations of the Wnt transcriptional effector β-catenin have not been observed, and even constitutive activation of the Wnt pathway does not abolish the oscillation of various Wnt and Notch components such as *Dkk1*, *Hes7*, and *Lfng* (45).

Another crucial and necessary feature of clock gene oscillation that underlies the emergence of traveling waves is coordination across neighboring cells. For traveling waves to emerge, cells in relative proximity should be in similar phases. Indeed, the Notch signaling pathway has been demonstrated to be the central mediator, naturally linking oscillation and synchronization (46). For instance, genetic ablation of the Notch pathway in zebrafish disrupts the formation of traveling waves, with neighboring cells showing uncoordinated oscillations (47,48). Another study used chimeric mouse embryos with wildtype and Notch-ligand *Dll1*-null mutant cells to demonstrate compromised synchronization of clock gene oscillations (39). This study further showed that LFNG modulates DLL1 in neighboring cells and plays a significant role in synchronization. The work of Yoshioka-Kobayashi and colleagues (49) demonstrated the fundamental link between synchronization and oscillation. Using a novel reporter line with faster maturation (*HES7*-Achilles), they showed that genetic ablation of *Lfng* leads to not only an uncoordinated "salt and pepper" pattern but also dampened *Hes7* oscillation at the individual-cell level. Co-culture experiments in which wildtype cells were placed in a majority *Lfng*-KO background showed that wildtype cells were advanced in oscillation phase, suggesting that the absence of LFNG leads to faster Notch signal transmission between neighboring cells. The authors used optogenetic activation of *Dll1* to measure Notch activation in receiver cells with or without LFNG and showed that LFNG indeed delays signal transmission. A chemical compound that increased coupling delay lengthened the oscillation period in wildtype cells and rescued the

Lfng-KO phenotype. This finding aligns with the theoretical expectation that the period of collective oscillation can differ from the average of individual oscillation and places coupling delay as a key parameter in regulating the dynamics of synchronized oscillations in the PSM, providing insight into important questions including the frequency gradient of oscillation along the AP axis and the species-specific oscillation period.

Figure 1.1. Interactions among signaling pathways underlie somitogenesis

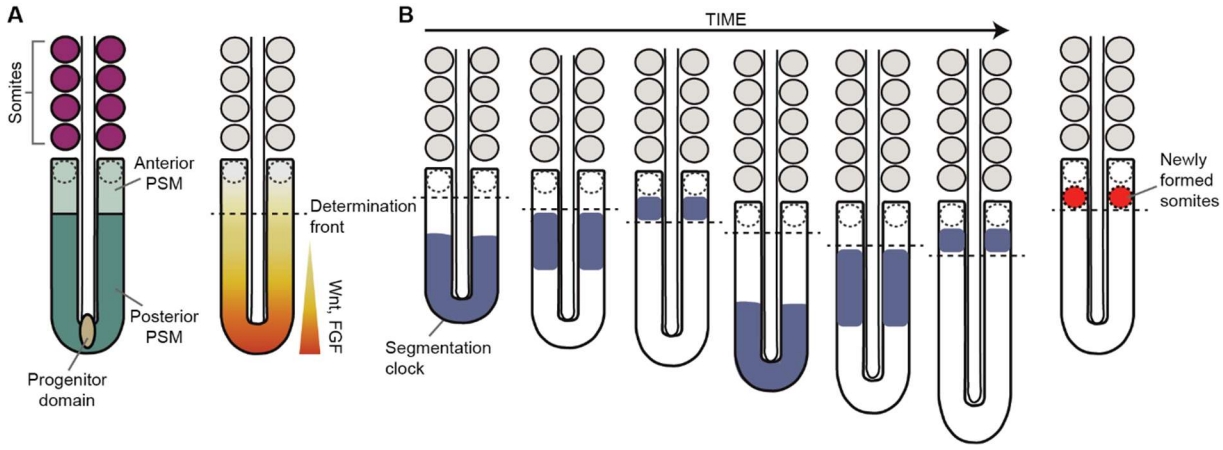

Figure 1.1. (A) Posterior-to-anterior gradients of FGF and Wnt signaling pathways in the PSM establish the AP level of the determination front at which nascent somites are specified and undergo mesenchymal-to-epithelial transition. The determination front regresses as the embryo elongates. (B) Segmentation clock genes, most notably members of the Hes/Her/Hairy family and components of the Notch signaling pathway, display periodic "traveling wave" expression patterns in the PSM. These genes are initially broadly expressed in the posterior PSM and progressively refine as the waves travel anteriorly. As traveling waves of oscillatory segmentation clock genes reach the determination front, the segmentation program is activated to specify a nascent somite. Adapted from (71), licensed under CC BY 4.0.

Signaling gradients in the PSM

The majority of PSM cells undergo rounds of oscillations but epithelial somite formation occurs only at the anterior tip of the PSM. The initial "clock and wavefront" model postulated the existence of a posteriorly regressing front at which the "clock" at the right phase can trigger

the segmentation event (6). Key findings on the molecular identity of the wavefront came from chick and zebrafish embryos. In early-stage embryos, *FGF8* expression forms a gradient in the PSM that is highest at the caudal end (50–52) (**Fig.1.1A**). Although *FGF8* mRNA can be observed from posterior to anterior in a smooth gradient, only the cells at the most posterior part of the PSM or the tailbud actively transcribe *FGF8*. Once the cells leave this caudal domain, they stop *FGF8* transcription, and the smooth gradient is formed by mRNA degradation, where the remaining mRNA level inversely correlates with the time or the distance since they left the caudal domain (51). The manipulation of FGF levels changed the extent of caudal PSM identity as well as somite size and boundary position, such that ectopic FGF8 beads resulted in smaller somites and anteriorly shifted somite boundaries, and the opposite result was obtained when FGF8 was locally inhibited, suggesting that the FGF activity level essentially functions as a determination front or molecular threshold below which clock gene oscillation can trigger somite formation (50,52).

Other key molecular gradients underlying the determination front include the Wnt and retinoic acid (RA) signaling pathways. In the PSM, the Wnt and FGF pathways positively regulate each other so that the Wnt pathway also forms a posterior-to-anterior gradient, with *Wnt3a* mRNA at the caudal end of PSM and a smooth gradient of nuclear β-catenin protein (41,53). However, the biological regulation of the Wnt gradient is likely more complex, given that the β-catenin mRNA level is relatively stable across the PSM (54). Wnt activity regulates genes associated with posterior PSM identity, such as *Msgn1*, *Tbx6*, and *Brachyury* (55–57). Mouse mutants with stabilized β-catenin display expansion of posterior PSM identity, anterior shift of determination front, and ectopic oscillations of *Lfng* and *Hes7*, demonstrating the role of the Wnt gradient in conferring posterior PSM identity and establishing the determination front

(45,58). On the other hand, the RA pathway forms an opposite gradient that is highest anteriorly through a different mechanism. The RA synthesis enzyme RALDH2 is expressed in the anterior PSM and somites, while the RA-degrading enzyme CYP26A1 is enriched in the tailbud, forming a gradient by the polarized distribution of enzymes with opposing actions (59,60). RA and FGF pathways inhibit each other and contribute to forming a sharp boundary at the determination front (61). In the PSM, exposure to RA leads to loss of FGF8 expression, and VAD quail that are deficient in vitamin A and RA during development exhibit anteriorly extended *FGF8* domains and smaller somites, similar to embryos implanted with FGF8 beads. Conversely, FGF signaling in the PSM inhibits the expression of *RALDH2*, an enzyme synthesizing RA, while upregulating Cyp26 expression.

While one of the implications of the traditional "clock and wavefront" model is that the clock and the wavefront are separate elements, some components of FGF and Wnt, two key signaling gradients that function as the wavefront, have been shown to oscillate, suggesting that the wavefront is not a statically regressing gradient but rather complexly intertwined with clock gene oscillations (40,41,43,62). A series of works in zebrafish and mouse provides an elegant model that dissects the precise roles and relationships of the "clock" and the "wavefront" (62–64). Phosphorylated ERK is a downstream effector of the FGF pathway, and its dynamic oscillatory expression pattern is crucial in specifying a group of cells corresponding to a presumptive somite to activate the segmentation program in a periodic, stepwise manner (62,63). However, genetic ablation of *Hes7* in mouse and *her1/7* in zebrafish results in smoothly regressing expression of pERK and the segmentation program gene *Mesp2*. More recent work in zebrafish further demonstrated that the main function of *her1/7* oscillation is to periodically depress double-phosphorylated ERK activity, which in turn specifies a block of presumptive

somite (64). The clock is dispensable for somite formation, as pulsatile inhibition of the FGF pathway was able to rescue somitogenesis in zebrafish mutants for *her1/7*. The resultant somites lacked proper rostro-caudal (RC) patterning. This finding suggests that segmentation is directly downstream of periodic changes in FGF activity, whereas the periodic expression of Notch/*Her* leads to inhibition of ERK triggering segment determination and establishing RC polarity (65). While the conservation of such a hierarchical relationship between *Hes/Her/Hairy* and FGF remains to be investigated, it demonstrates the depth and complexity of crosstalk among signaling pathways in the paraxial mesoderm.

Regulation of oscillation period

One of the major questions in the field is the regulation of oscillation frequency. Various biochemical and biophysical parameters underlying the kinetics of the time-delayed negative feedback loop of *Hes/Her/Hairy* have been hypothesized to be involved in the regulation of oscillation frequency. For instance, decreasing the number of introns of the *Hes7* gene in various mammalian species including the mouse embryo resulted in a faster pace of oscillation (35,66), whereas a genetic mutation in zebrafish *her6* that leads to reduced production of mature mRNA leads to a slower pace of oscillation (67). Comparative measurement of various biochemical processes in clock gene oscillation across multiple model organisms suggests that transcript processing and nuclear export are much slower and likely more rate-limiting than transcription, which is much faster (68). However, modifications to the clock's time delay often lead to premature dampening of population-level oscillation, revealing the existence of a narrow window of such parameters that enable persistent oscillation (69).

More recently, cross-species analysis combined with advancements in in vitro models has been instrumental in advancing our knowledge of the regulation of oscillation rate (33,70,71). Using human and mouse iPSCs, it was shown that swapping the *Hes7* locus between species only slightly changed the period, but the difference was not large enough to account for the period difference between 2hr in mouse and 5hr in human (34). Instead, other processes such as degradation rate and expression delay were shown to be significantly slower in human and likely underlie the oscillation rate differences between the two species based on a mathematical model. This comparative approach was further pushed to the "stem cell zoo" of several mammalian species ranging from marmoset and rabbit to human and rhinoceros (35). This approach showed that oscillation periods of different species show strong correlations with embryogenesis lengths and biochemical reaction rates for protein degradation and RNA processing, further generalizing previous findings from embryo and in vitro experiments.

Metabolism has been demonstrated to be one of the key regulatory axes governing species-specific oscillation periods (33,36). The co-culture experiment of human and mouse iPSCs showed that oscillation period is an intrinsically species-specific parameter that is unchanged by the presence of majority of neighbor cells of different species (33). While the mass-controlled metabolic rate is higher in mouse cells, modulating the electron transport chain and NAD+/NADH ratio was able to both accelerate and decelerate the oscillation period in human PSM cells, providing strong evidence for the role of metabolism in the regulation of oscillation period. The slower oscillation upon electron transport chain inhibition can be partially explained by the change in translation rate that is regulated by cellular metabolism. In addition, another study established a more specific causal link between different metabolic perturbations and different rate-limiting steps of clock gene oscillation (36). The authors showed that

inhibition of glycolysis mainly affects HES7 protein degradation and production delay (time taken for transcription and translation), whereas inhibition of the electron transport chain lengthens intron delay (mRNA processing). These findings warrant metabolism as a promising factor underlying oscillation period and developmental tempo.

Interestingly, metabolism has recently been further highlighted as crucial in PSM development. In chick and mouse embryos, glycolytic activity and expression of glycolytic enzymes form a gradient along the AP axis of the PSM (72–74). The posterior-to-anterior gradient of FGF signaling regulates elevated aerobic glycolysis of cells at the tailbud and posterior PSM, and inhibition of glycolysis leads to disruption in the cell motility gradient underlying axis elongation as well as the maintenance of the posterior-to-anterior Wnt gradient, crucial for NMP maintenance and PSM differentiation. Experiments in chick embryos and in vitro systems demonstrated that high aerobic glycolysis at the posterior is responsible for a higher intracellular pH that promotes Wnt signaling via β-catenin acetylation (73).

The highlighted roles of metabolism in regulating oscillation dynamics and establishing gradients along the PSM leads to an interesting perspective on the frequency gradient in the PSM. In the PSM, posterior PSM cells undergo faster oscillation compared to anterior PSM cells, and the mechanism underlying this frequency gradient is not known (75). The findings from human organoids give a crucial hint to this problem. Yaman and Ramanathan (76) introduced a human axial organoid composed of a neural tube and bilateral paraxial mesoderm with sequential somitogenesis. This model also mimics the posterior gradients of Wnt and FGF and stereotypic traveling waves with a frequency gradient. Global activation of FGF in this organoid abolishes the traveling waves and the frequency gradient and leads to oscillation with a uniform phase along the AP axis, demonstrating the significance of the posterior FGF gradient in

the generation of the frequency gradient. While other factors such as coupling delay may also be spatially modulated and contribute to this phenomenon (3,49,77), it is possible that the metabolic gradient downstream of FGF signaling provides a further mechanistic explanation for the differential frequency between the posterior and anterior PSM. FGF and Wnt at the posterior PSM are known to positively regulate each other, but it is worth noting that Wnt activation in a human organoid by CHIR99021 did not affect the frequency gradient (76). Instead, global Wnt activation in mouse embryonic PSM with LiCl led to slower oscillations (78). Thus, while the FGF gradient—and potentially a downstream metabolic gradient—seems to have mechanistic relevance, more comprehensive research efforts beyond a simple scheme of signaling gradients will be necessary to elucidate the emergence of the phase gradient and the traveling wave.

Epithelial somite formation and polarity establishment

While the functional and molecular details of "clock" and "wavefront" remain to be elucidated, available evidence suggests that the "clock" establishes the discrete periodicity of new segmental domain, and that the "wavefront" confers positional input at which the cells can undergo somite formation. The signaling pathways discussed earlier are integrated at the anterior PSM to activate the segmentation program by triggering expression of the *MESP* genes, a family of bHLH transcription factors (79,80) (**Fig.1.2**). *Tbx6*, a PSM marker downstream of the Wnt pathway, and Notch signaling and its effector NICD cooperatively activate the expression of *Mesp2*, particularly with TBX6 directly binding to the enhancer region of *Mesp2* (81,82). Conversely, the FGF signaling pathway represses *Mesp2* expression (62,83). In mouse, Notch (NICD) and FGF (pERK) oscillations overlap posteriorly, but, as the NICD wave refines while traveling anteriorly, pERK is periodically downregulated to allow the narrow band of NICD to

activate *Mesp2* (62). In other words, the small region of the anterior PSM that is *Tbx6*-positive and undergoes a pulse of Notch oscillation during the periodic downregulation of FGF expresses *Mesp2*. MESP2 in turn activates expression of *Ripply1/2* that downregulates *Tbx6* in that domain, thereby setting the anterior extent of the next MESP2 domain to regress posteriorly by about the length of one segment (83,84). *Ripply* genes constitute a negative feedback loop, as they repress *Mesp2* in turn, ensuring transient *Mesp2* expression and proper RC patterning (85).

Once the MESP2 domain demarcates the presumptive somite, it quickly establishes RC polarity prior to epithelial somite formation, where each rostral and caudal half of the presumptive somite express different molecular markers. For instance, MESP2 is refined to the rostral half, downregulates Notch signaling, and activates rostral markers such as *Tbx18* and *EphA4* (84,86,87). The caudal half without MESP2 expresses caudal markers such as *Dll1*, *Uncx4.1*, and *EphrinB2* (87–90). The molecular identities of the rostral and caudal halves are maintained by TBX18 and UNCX4.1, respectively (91–93). Disruptions of the genetic regulatory circuits specifying either rostral or caudal compartments lead to expansion of ectopic caudal or rostral identity within each segment (85,93). While the precise mechanism remains to be determined in different embryo models, findings in human iPSC organoid provide key mechanistic insight into how MESP2 becomes refined to the rostral compartment. The organoid models called “somitoid” and “segmentoid” simulate the differentiation and morphogenetic trajectory of paraxial mesoderm from clock gene oscillations to segmentation of somite-like structures, respectively in 2.5D and 3D (94). In this system, MESP2 is initially expressed in a “salt and pepper” manner, which is also observed in chick and mouse embryos. These cells quickly sort and segregate based on their MESP2 expression level, leading to separation of cell clusters exclusively containing MESP2-high or MESP2-low cells, each representing the rostral

and caudal compartment. Although this sorting behavior has not yet been validated in vivo with live imaging, it likely provides an important hint about the morphogenetic mechanism underlying the establishment of RC polarity.

The molecular RC polarity is soon translated into physical boundary formation initially via the Ephrin-Eph pathway, a signaling pathway mediated by membrane-bound ligands and receptors of the receptor tyrosine kinase family with a well-known function in cell-cell repulsion and boundary formation (88,95–97). MESP2 in the rostral compartment activates expression of the EphA4 receptor at the presumptive anterior border (90,98,99). Then, EphA4-expressing cells induce EphrinB2-reverse signaling in the juxtaposed cells of the presumptive posterior boundary, which is sufficient to form a boundary (90). This signaling then downregulates CDC42—a GTPase protein of the Rho subfamily that regulates the actin cytoskeleton—activity to enable MET (100). Rho GTPase proteins such as CDC42 and Rac1 play a crucial role in the proper epithelialization of somites. In the chick embryo, overexpression and inhibition of *CDC42* lead to failure in epithelialization and hyper-epithelialization, respectively, while experimental modulation of RAC1 activity also leads to failure in proper epithelialization. In addition, while the inter-somitic fissure is formed by Ephrin-Eph signaling and downstream actin cytoskeleton remodeling via CDC42 and RAC1, the extracellular matrix plays a crucial role in the formation and maintenance of this boundary. In the forming boundary, integrin (*itga5*) is upregulated downstream of Ephrin-Eph signaling and forms clusters that drive fibronectin assembly (101,102). Experiments in the chick embryo showed that the overlying ectoderm is the major source of fibronectin (103–105). Integrins are transmembrane proteins that anchor cells to the extracellular matrix, such as fibronectin, laminin, and collagen, and form focal adhesion points functioning as centers for cell-substrate interaction and signaling cascades. In zebrafish, mutant

embryos for either *fn* (fibronectin) or *itga5* (integrina5) can form a boundary but fail to maintain it (102). Mouse mutants without focal adhesion kinase—an intracellular protein tyrosine kinase that mediates signaling downstream of integrin-fibronectin interaction—do not form proper somites, suggesting a crucial role of cell-substrate interaction in epithelial somite formation (106). Curiously, although the molecular circuit underlying RC polarity establishment and boundary formation are tightly associated, these two processes are genetically dissociable. For instance, mouse mutants with a hypomorphic *MESP* allele fail to establish proper RC polarity but somite boundaries as well as some genes underlying boundary formation are normal (99). Similarly, mouse mutants overexpressing NICD form caudalized somites, but boundary formation still occurs (44). Lastly, a human iPSC organoid model that forms somite-like epithelial rosettes ("somitoid") also shows normal epithelialization of somite-like structures despite genetic ablation of *MESP2* (94). Thus, RC polarity establishment is not necessary for boundary formation, and further investigation is needed to elucidate the precise regulatory circuit connecting these two processes.

Paraxis (TCF15) is a core bHLH transcription factor underlying MET that orchestrates modulations of the cytoskeleton, extracellular matrix, cell-cell and cell-ECM adhesion (107,108). During epithelialization, somite cells become elongated and polarized such that the outer surface forms a basal lamina layer composed of laminin and collagen (109,110). Eventually, the resultant somite is composed of a pseudostratified epithelial layer and an inner cavity (somitocoel) with a small population of mesenchymal cells at the apical side. Paraxis is expressed by formed somites and the anterior PSM, and mutant mice without Paraxis fail to form epithelial somites and to

maintain RC polarity (111). WNT6 emanating from overlying ectoderm is necessary for the proper expression of Paraxis and epithelialization of somites (112). Additionally, transcription factors MEOX1/2, and PAX3 are also necessary for epithelialization.

Figure 1.2. Activation of segmentation program and establishment of somite RC polarity

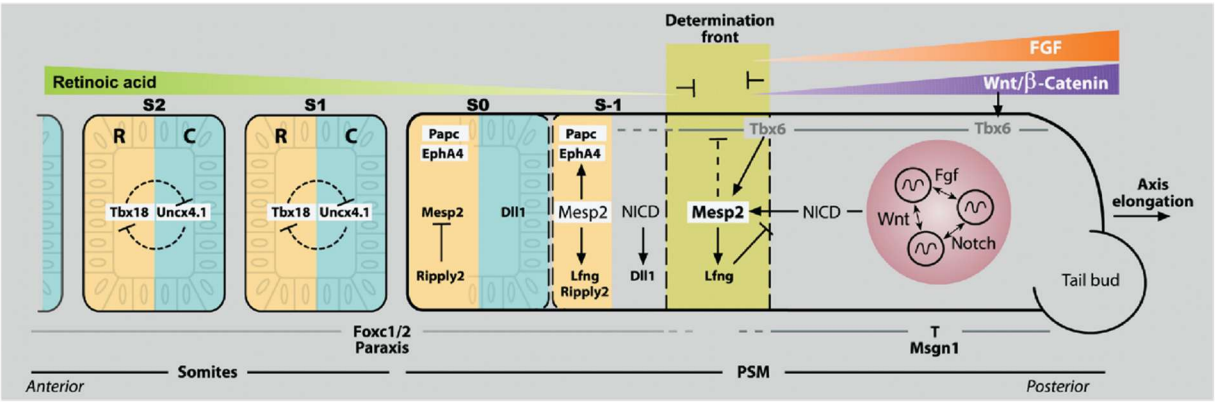

Figure 1.2. The posterior FGF and Wnt signaling gradients confer posterior PSM identity, underlying the expression of posterior PSM markers TBX6 and MSGN1. The antagonistic interaction between the anterior RA and posterior FGF gradients sets the determination front, at which TBX6 and periodic Notch activity driven by the segmentation clock cooperatively activate the segmentation gene MESP2. MESP2 downregulates TBX6, ensuring stepwise specification of presumptive segmental domains. MESP2 is soon restricted to the rostral half of the presumptive somite and confers rostral identity, activating its downstream targets, including TBX18, EPHA4, LFNG, RIPPLY1/2, and PAPC. The antagonistic interaction between the rostral determinants (e.g., TBX18) and caudal determinants (e.g., UNCX4.1) underlies the maintenance of the RC polarity. Adapted from (109), with permission from Cold Spring Harbor Laboratory Press.

Somite patterning and compartmentalization

The formed somite is subdivided into multiple compartments that are morphologically and molecularly distinct. These compartments form the basis for the different anatomical lineages derived from the somite. Tissues surrounding the somite, such as the lateral plate mesoderm, neural tube, and ectoderm, play a crucial role in this process as they provide inductive signaling cues that drive specification of different fates. The ventral part of the somite,

as well as the somitocoel cells, forms the sclerotome, while the dorsal part remains epithelial and forms the dermomyotome. The sclerotome gives rise to vertebrae and ribs, vertebral discs, part of the skull, tendons, smooth muscles of the aorta, and the pectoral girdle and scapula; the dermomyotome gives rise to the dermis of the back, and the muscles of the limb, tongue, and abdominal wall, and brown fat (2,24,109). All parts of the somites contribute to the endothelial cell lineage (2).

While the precise timing of differentiation may vary along the AP axis, for trunk somites, the ventral part downregulates PAX3 and 7 while activating PAX1 and 9, marking the establishment of dorsoventral (DV) polarity and the specification of the sclerotome fate (109,113). The two most recently formed somites are not committed and exhibit plasticity, as a somite rotation experiment along the DV axis led to normal development of dorsal dermomyotome and ventral sclerotome (114). Conversely, DV rotation of more differentiated somites led to ectopic somite compartments. On the other hand, rotation of nascent somites along the RC axis always leads to ectopic RC polarity, revealing different timelines for the establishment of DV and RC polarity.

Signals emanating from the floor plate of the neural tube and from the notochord play a central role in the specification of the sclerotome fate (113,115–117). Sonic hedgehog, produced by the notochord and floor plate, activates the expression of the sclerotome markers *PAX1* and *PAX9*. Noggin and Chordin are produced by the notochord, and they antagonize BMP4 emanating from the lateral plate mesoderm. BMP4 from the lateral plate mesoderm plays a key role in establishing mediolateral polarity. For instance, a high level of BMP4 can transform paraxial mesoderm into lateral plate mesoderm, and a low level induces the expression of the

lateral somite marker Sim1 (118–120). BMP4 also represses *PAX1* expression (121), so Noggin and Chordin ensure sclerotome differentiation in the ventromedial part of the somites.

The ventral part of the somite expands ventromedially and undergoes EMT (2). The mesenchymal sclerotome is morphologically divided into rostral and caudal compartments by the von Ebner fissure. The rostral and caudal halves exhibit distinct profiles regarding not only molecular markers but also extracellular matrix composition and cell density (122). For instance, the caudal half has higher cell density and expresses extracellular matrix components like chondroitin-6-sulfate and signaling factors like Ephrin ligands and F-spondin that inhibit neural crest migration (89,123–125). These differences make only the rostral half a permissive environment for neural crest and axon migration, as well as dorsal root ganglion formation, exemplifying a mechanism by which the somite imposes segmentation on other organs such as the peripheral nervous system. Later, the sclerotome continues to expand ventromedially to encircle the notochord and gives rise to the vertebral column through resegmentation, where the rostral half of a somite joins with the caudal half of the anteriorly adjacent somite to form a single vertebra (2,109).

The dorsal half of the somite forms the dermomyotome, which later gives rise to the dermis of the back, skeletal muscle, connective tissue, endothelium, and brown fat. As in the sclerotome, signals emanating from neighboring tissues including the ectoderm, neural tube, and lateral plate mesoderm play crucial roles in the establishment of the dermomyotome lineage and the diversification of developmental trajectories. As the ventral part of the somite undergoes EMT and upregulates PAX1 and 9 at the expense of PAX3 and PAX7, the dorsal portion remains epithelial expressing PAX3 and 7 expression. Paraxis, a key transcription factor for epithelialization, is also retained only in the dermomyotome. Wnt signaling from the dorsal

ectoderm and neural tube activates the dermomyotome markers PAX3 and 7 (126,127). SHH from the floor plate and notochord counteracts Wnt signaling by activating the Wnt inhibitor SFRP2 (128). Similarly, Wnt activates the Shh inhibitor GAS1 in the dorsal somite to prevent ectopic sclerotome formation and to form sharp DV polarity through mutual inhibition (129).

Morphologically, the dermomyotome is a rectangular epithelial sheet over the sclerotome extending diagonally from the dorsomedial side to the ventrolateral side. All four edges of the rectangular dermomyotome adopt lip-like structures and function as sites of production for myocytes of the myotome (130). The dermomyotome can be subdivided into three major sub-compartments that are molecularly, morphogenetically, and developmentally significant: the dorsomedial lip, central dermomyotome, and ventrolateral lip. The dorsomedial lip is both marked and maintained by WNT11, after the initial specification by Wnt signals from the dorsal neural tube (131). The ventrolateral lip, marked by SIM1, is specified by WNT6 from the overlying ectoderm and contained laterally by WNT11 antagonism. This subdivision of the dermomyotome represents an important checkpoint for major muscle lineages because the myotome generated from the dorsomedial lip gives rise to the epaxial muscles—muscles of the back—whereas that from the ventrolateral lip contribute to hypaxial muscles—muscles of the abdominal wall, limb, tongue, and diaphragm (130,132). Cells at the lips of the dermomyotome undergo EMT and contribute to the immature myofibers underneath the dermomyotome, forming the myotome. The central dermomyotome gives rise to the dermis of the back while also contributing to both the DML and VML.

Special features of anterior somite

Somites give rise to anatomical structures characteristic of their axial level, forming the basis of different axial identities of somites: from rostral to caudal, occipital, cervical, thoracic, lumbar, sacral, and coccygeal (2). Different species have unique numbers of total somites as well as numbers of somites corresponding to each axial group. For instance, in the chick embryo, it is described that somites 1-5 are occipital, 5-19 cervical, 19-26 thoracic, 26-30 lumbar, 30-39 sacral, and 39-52 coccygeal (2,133,134). Most of our knowledge of somitogenesis and somite development, however, has derived from experiments and observations performed in cervical, thoracic, or lumbar somites, for reasons including the convenience of access and embryonic manipulation or the fragility of embryos at earlier stages. For example, the first molecular identities of the segmentation clock gene (*c-hairy1*) and the determination front (*FGF8*) were discovered with chick embryos at stages producing cervical-to-thoracic somites, and one of the widely accepted staging schemes for somite development is also largely based on thoracic-to-lumbar somites (2,134). However, different features of somite development can vary across axial levels, including formation and maturation dynamics, gene expression profiles, and interactions with neighboring tissues.

Occipital somites (1st-5th in chick) are the rostral-most somites between the head mesoderm and the cervical somites. Traditional fate-mapping experiments in which quail occipital somites were grafted into chick hosts at the corresponding axial level showed that they give rise to the caudal part of the skull (supraoccipital, exoccipital, basioccipital); parts of the atlas and axis; various neck, glossal, hypoglossal, and laryngeal muscles; occipital and dorso-cervical dermis; and meninges (24,135). They represent one of the least understood classes of somites, as they exhibit several unique features in development compared to other somites. One

major difference is that, as they lie at the head-neck transition zone, occipital somites give rise to the caudal part of the skull, which is not overtly segmented (24,135). Only the last occipital somite (5th) gives rise to parts of the first two vertebrae (atlas and axis). Thus, it is possible that the RC polarity of the somite has different functional relevance or even is differentially established. A finding that supports this idea is that dorsal root ganglia do not form in any part of the occipital somites, which at the trunk level develop specifically at the rostral half of the somite (136,137). In other words, one of the major functional consequences of RC polarity, the segmentation of the peripheral nervous system, is not relevant to occipital somites. The most revealing evidence comes from the examination of RC marker expression in the chick embryo (138). When expression patterns of various Notch components that are specific to either the rostral or caudal halves of trunk somites were analyzed, 1st-3rd somites did not express any of these RC-polarity markers, and 4th-9th somites expressed only a subset of such markers. These findings strongly suggest that the nature of RC polarity and, more generally, the molecular profile of occipital somites differ from those of trunk somites.

Moreover, evidence from various model organisms suggests that there might be differences in somitogenesis between the rostral-most somites and trunk somites. The periodicity of somite formation is variable across axial levels in different organisms, where the period is generally faster in rostral somites and slower in caudal ones (139). In the chick embryo, the period of occipital somite formation is 60-75 min, while the clock-gene oscillation is indeed coupled to somite segmentation (140). From the 6th somite onward, the period converges to the approximately known period of 90 min. In addition, multiple mouse and zebrafish mutants with disruptions in somite formation show varying anterior or posterior extents of the disruption phenotype. For instance, multiple mouse mutants with defective axis elongation and PSM

development still form 8-10 anterior-most somites (141). More specifically, zebrafish mutants for Notch signaling components including *her7*, *notch1a*, and *deltaD* have defects in trunk somites but normally form 5-6 rostral-most somites (134,138,142–145). These mutants have varying anterior limits of defect, and combinations of these mutants often exhibit anterior expansion of defective somites but fail to affect the anterior-most somites. On the other hand, the zebrafish *her1* mutation only affects formation of the 1st-3rd somites (29). Similarly, zebrafish mutations in *itga5* lead to somitogenesis defects for only the anterior-most somites (101). Although the conservation of this phenomenon in different vertebrate species, including chicken, remains to be established, these findings raise the hypothesis that the molecular mechanisms by which anterior-most somites form might be, to some extent, different from those of posterior somites.

Besides the formation process, the maturation and developmental dynamics of occipital somites are also different from those of thoracic/lumbar somites. In chick trunk somites, molecular markers for the sclerotome and dermomyotome—*PAX1* and *MYOD1*, respectively—are activated in two rounds of segmentation, and mesenchymal sclerotome formation takes place in about seven rounds of segmentation (134). Also, such compartmentalization of somites proceeds sequentially from rostral to caudal. Conversely, for occipital somites, *PAX1* and *MYOD1* expression are much delayed and rather simultaneously activated in all five occipital somites. Development of the myotome in the chick embryo also shows similar dynamics (146,147). These findings indicate not only that the timeline of differentiation and compartmentalization is distinct for occipital somites but also that occipital somites have an extended window of a plastic, undifferentiated state. Indeed, a classic transplant experiment demonstrates remarkable plasticity of the occipital somite (148). When grafted to a different axial level, non-occipital somites maintain their Hox gene profile and morphogenetic program,

such that transplantation of a thoracic somite to the cervical level would result in ectopic ribs at the neck (149). However, when 1st-4th somites, which do not form vertebrae, are transplanted to the trunk level, they indeed form mostly normal but incomplete vertebrae without activating Hox genes for the destination axial level (148).

Then, what could be the mechanistic explanation for such distinctive characteristics of the occipital somites? The definitive answer is not yet known, but the developmental origin of the anterior-most somites may contribute to answering this question. For instance, single-cell RNA sequencing of E6.5-8.5 embryos identifies a distinct transcriptional trajectory for anterior-most somites versus more posterior somites, although these trajectories ultimately converge toward a shared paraxial mesoderm identity (150). It is proposed that the precursors of the anterior-most somites arise from the same region of the primitive streak as those for cardiac/lateral plate and cranial mesoderm and ingress in a T/Brachyury-independent manner along with other anterior mesoderm precursors (150,151). As a result, the transcriptional trajectory for anterior somites exhibits elevated expression of lateral plate mesoderm marker genes, which might molecularly discriminate anterior-most somites from posterior ones. Another possible explanation is that the occipital somites are exposed to a different signaling environment. While there are multiple signaling gradients that define the dynamics of somitogenesis and paraxial mesoderm maturation, it is possible that in early stages such gradients are not fully established or stable. Alternatively, the occipital somites can be uniquely exposed to certain signaling gradients that are only present in the early embryo. A signaling pathway that spatially and temporally overlaps with the anterior-most somites but not with posterior somites is the left-right (LR) determining pathway. In the next chapter, the overview and mechanism of the LR determining pathway will be described. Importantly, the possible

intersection between the LR pathway and the paraxial mesoderm will be highlighted, which will be the main question of this thesis.

Part 2. Left-right determination in the early vertebrate embryo

Overview of LR patterning and symmetry breaking in vertebrates

Bilateria is the largest clade of metazoans, characterized by a body plan with bilateral symmetry along the AP axis. Species of Bilateria, however, exhibit varying modes and extents of asymmetry. The bilateral symmetry of vertebrates comes mainly from the musculoskeletal system, which contrasts with asymmetric internal organs. For instance, the heart is located on the left side, and its asymmetric development appears in the very early embryo. Moreover, various endoderm-derived organs such as the stomach, lung, and liver, as well as the brain, are stereotypically asymmetric in their position and/or morphology. Proper LR patterning of these organs is critical for human health, as disruption in LR patterning is highly associated with various congenital diseases (152,153).

The establishment of LR asymmetry in embryogenesis follows a general sequence: bilateral symmetry is broken and leads to asymmetric gene expression, which in turn activates a lateralized morphogenetic program (152). The best-characterized symmetry breaking events occur at the LR organizer (e.g., Kupffer's vesicle in zebrafish, HN in chick, the node in mouse) of early embryonic stages during gastrulation and neurulation. However, the "true" origin of asymmetry (e.g., a chiral molecule that instructs robust symmetry breaking) and the earliest symmetry breaking event remain topics of active debate and research (152).

An intriguing theme of LR determination is that the core machineries driving the patterning process are very well conserved, whereas the upstream processes leading to activation of such machineries are rather divergent. For instance, the Nodal signaling pathway, a member of the TGF-β family, is a left determining factor whose function is conserved in species from diverse phyla, including snails, sea urchins, and all vertebrates (154,155). While Nodal is not

utilized in some major model organisms such as Drosophila and C. elegans, phylogenetic analyses suggest that a Nodal-based mechanism was likely present in the earliest bilaterians, although it was lost and replaced by other mechanisms in some lineages (155–157). A recurring motif is that a divergent upstream process triggers transient expression of Nodal, mostly on the left side of the LR organizer, which in turn activates Pitx genes, homeobox transcription factors driving cascades of molecular events underlying LR determination and morphogenesis. The precise role and downstream targets of the Nodal-Pitx axis are active areas of research and remain poorly understood.

In vertebrates, a major class of symmetry breaking mechanism involves directional fluid flow generated by motile cilia in the LR organizer, although it is not conserved in some mammals (e.g., pig), birds, and reptiles. For instance, in the mouse embryo, node cells have motile cilia that rotate in a clockwise direction, driven by dynein motor proteins (158,159). While the morphology of the node resembles a pit, the apical surface of nodal cells is dome-like. In addition, the basal body of these motile cilia is located posteriorly in each node cell, resulting in posterior tilt of the motile cilia (159,160). Such geometric properties of cilia and nodal cells and the clockwise rotation altogether generate a leftward flow of extraembryonic fluid that is necessary for proper LR patterning of an embryo (161). For instance, artificial rightward flow is sufficient to invert the situs of the mouse embryo (162). It is proposed that immotile cilia at the edge of the node respond to the mechanical force generated by the flow or that signaling molecules and lipid vesicles are carried with the leftward flow (163–166). Recent works in zebrafish and mouse demonstrate that immotile cilia indeed function as mechanosensors that trigger calcium signals and downstream signaling cascades on the left side of the node (167,168). Besides, works in mouse and frog also suggest that R-spondin 2, Pkd1l1, and Mmp21 are

transported leftward by the ciliary flow and play a crucial role in proper symmetry breaking (169–171). These findings suggest that the two proposed functions of ciliary flow likely work in parallel. Such directional fluid flow by motile cilia is conserved in a diversity of vertebrate species including frog, zebrafish and, likely, humans, and plays a crucial role in the establishment of LR asymmetry, although details regarding the dynamics of flow and geometry of cilia and the LR organizer vary across species (155,172–175). However, it should be noted that the position and function of ciliary flow in the comprehensive context of LR asymmetry remain to be elucidated, as, for instance, human patients with primary ciliary dyskinesia—a genetic disorder with dysfunctional motile cilia—show randomized visceral situs but have normal handedness and brain asymmetry (176–178).

Even though ciliary flow represents one of the best characterized processes leading to LR determination and is critical for robust laterality in some vertebrate species, it most probably does not represent the earliest LR determining mechanism (152). For instance, various proteins and mRNAs that are relevant to LR asymmetry show asymmetric distribution in early stages before ciliary flow, even in species whose laterality depends on ciliary flow (179–183). Thus, an alternative approach seeks the earliest, deeper origin of LR asymmetry from the chirality of cytoskeletal elements (184,185), which asymmetrically localize ion transporters (e.g., K^+ channels, H^+ pumps) throughout the earliest cleavage events of the embryo (152,186,187). Chemical and bioelectric gradients downstream of asymmetric ion transporters are then translated into robust gradients of charged molecules that play critical roles in lateralized gene expression. While such a model is not mutually exclusive with the role of ciliary flow, the conservation and functional relationship of these two mechanisms require further investigation (152,155,178).

Symmetry breaking in the chick embryo

While the seminal discoveries on the molecular and genetic components of the LR pathway were made in chick, the chick embryo—along with pig, other birds, and likely reptiles—does not utilize a mechanism involving ciliary flow (188–190). HN of the chick embryo does not have motile cilia but displays very early morphological asymmetry. At HH4, HN is seemingly tilted to the left, so that the forming notochord is rooted to the right side of HN, and the right side of the node is thicker than the left side (191,192). Initially, at HH4, *SHH* and *FGF8* are symmetrically expressed at HN. As HN regresses posteriorly and forms the notochord, *SHH* is progressively lateralized on the left side of HN, and *FGF8* on the right side (193,194). Cells at the *SHH* expression domain around HN engage in a counterclockwise movement toward the left side of HN (190,195). This cell rearrangement is necessary for proper asymmetric gene expression because both the insertion of hair and surgical separation result in bilaterally symmetric gene expression. Also, this process is downstream of the actin cytoskeleton, as drugs inhibiting Myosin II and Rho kinase resulted in symmetric expression of *SHH* and *FGH8* (190).

Another key signaling pathway that is asymmetrically expressed is activin signaling, a member of the TGF-β superfamily. The Activin B ligand and Act-RIIa receptor are asymmetrically expressed on the right side and activate right-sided expression of BMP4 (193,196–198). BMP4 activates FGF8 on the right side of HN and is involved in mutual repression with SHH, ensuring the sharp separation of left- and right-specific gene expression domains. Ultimately, signaling cascades at the left and right sides of HN culminate with the asymmetric expression of NODAL on the left side of HN at HH5-6. Indeed, SHH has been shown to be both necessary and sufficient for NODAL expression at HN, as implantation of cells expressing SHH, as well as treatment with the SHH agonist SAG, induced ectopic NODAL

expression, while implanting beads soaked in anti-SHH antibody suppresses NODAL expression (193,199,200).

Yet another parallel mechanism toward left-sided NODAL expression involving the Notch signaling pathway has been described. In the early chick embryo at HH3, prior to asymmetric gene expression, cells on the left side of HN are depolarized compared to those on the right side (201). This difference in membrane voltage potential is one of the earliest known features of LR asymmetry in the chick embryo and is established by the asymmetric activity of the H^+/K^+-ATPase pump. Treatment of the early chick embryo with drugs targeting this pump not only affects the membrane voltage gradient but also the expression of key asymmetric genes such as *SHH* and *NODAL*, placing this gradient upstream of asymmetric gene expression at HN. A similar result regarding asymmetric gene expression is also observed upon perturbation of the H^+-V-ATPase pump at a similar stage (186). In addition, the H^+/K^+-ATPase establishes a Ca^{2+} gradient in the chick embryo around the time NODAL is activated, in a way that extracellular Ca^{2+} is elevated on the left side of HN (202). Ca^{2+} levels modulate the activity of the Notch signaling pathway, which in turn activates NODAL via Notch-responsive RBPjk-binding sites in the *NODAL* promoter (203). It is proposed that the local hyperactivation of Notch signaling on the left side of HN downstream of the Ca^{2+} gradient is directly responsible for the left peri-nodal activation of NODAL. While the H^+/K^+-ATPase activity gradient is upstream of both SHH and Ca^{2+}/Notch asymmetry, modulating SHH does not alter Notch activity, suggesting that SHH is not upstream of Notch asymmetry (203).

As in many other model organisms, the “true” origin or earliest instance of LR asymmetry in the chick embryo is not known. For instance, it is not known how the asymmetric membrane voltage gradient is established (201). In addition, a recent work that elegantly

described the early “polonaise movement” underlying primitive streak formation at HH3 revealed striking asymmetry in cell behavior (204). When the left and right counterrotating cell flows are traced and compared via live imaging and particle image velocimetry, the cell flow on the right side was more “dominant,” with higher speed and vorticity. The functional relationship between this novel asymmetry in cell movement and other known features of LR asymmetry remains to be elucidated.

Propagation of LR identity in the chick embryo

In different vertebrate species, early symmetry breaking mechanisms are highly divergent, but the activation of the Nodal-Pitx2 axis in the left lateral plate mesoderm is conserved. The consequences of symmetry breaking at the LR organizer should be relayed to the lateral plate mesoderm, through the paraxial mesoderm in between. Although NODAL is known to activate itself via positive autoregulation (205), a series of explant experiments suggests that a secondary signal from paraxial tissue is necessary for peri-nodal SHH to induce NODAL in the lateral plate mesoderm (199). The signaling molecule responsible for the propagation of NODAL is Caronte/CER1, a member of the Cer/Dan family of BMP antagonists (206,207). *CER1* is a paralog to *Dand5* in other vertebrate species including mouse and zebrafish, a primary target of ciliary flow that leads to degradation of *Dand5* mRNA on the left side of the LR organizer and specifically represses *Nodal* on the right side (208–213). *CER1* is activated by SHH and repressed by FGF8. *CER1* is initially symmetrically expressed around the HN but starts to be downregulated on the right side of the embryo (206). At HH7-8, *CER1* is asymmetrically expressed in the paraxial mesoderm and lateral plate mesoderm on the left side. The main function of *CER1* is to inhibit BMP signaling, which is broadly expressed in both the left and right LPM and inhibits *NODAL* expression. As BMP is inhibited by CER1, NODAL is

propagated to and transiently amplified in the left lateral plate mesoderm by HH7-8. NODAL is a secreted factor of the TGF-β superfamily that triggers downstream signal transduction via interaction with EGF-CFC proteins that function as co-receptors for NODAL, Cripto, and Cryptic (214). As the NODAL ligand binds TGF-β receptors with EGF-CFC co-receptors, it triggers phosphorylation of Smad2/3, which in turn associates with Smad4 and functions as a transcription factor for downstream targets. A conserved NODAL target in LR patterning is PITX2, a left determining transcription factor mediating a downstream morphogenetic program in various organs (215–219). NODAL expression initially spans broadly across the left LPM at HH8, inducing *PITX2* in an overlapping region in the left LPM, but regresses to a small posterior domain in the left LPM by HH9-10 and disappears (193).

A core component of the Nodal regulatory circuit, which ensures the spatial and temporal specificity of Nodal signaling and the downstream left determining program, is LEFTY1/2, a member of the TGF-β superfamily. LEFTY1/2 is activated by NODAL but inhibits NODAL by either directly intercepting the NODAL ligand or competitively binding to EGF-CFC co-receptors, thus forming a negative feedback loop (206,214,220–225). The diffusion rates of both LEFTY proteins are faster than that of NODAL, so the combination of the short-range activator NODAL and the long-range inhibitor LEFTY establishes a classic example of the reaction-diffusion model (224,226–229). This mechanism critically underlies the function of LEFTY1/2 in spatially and temporally confining NODAL signaling. LEFTY1 and LEFTY2, however, display distinct expression patterns in early LR patterning. LEFTY1 is primarily expressed at the left side of the floorplate, notochord, and paraxial and lateral plate mesoderm. Its expression pattern in the paraxial and lateral plate mesoderm largely overlaps with that of NODAL (229,230). Importantly, LEFTY1 expression at the midline functions as a midline barrier that

prevents the diffusion of left determining signals to the right side. For instance, the loss of LEFTY1 results in bilateral expression of PITX2 (231). LEFTY2, on the other hand, is primarily expressed in the left LPM around an overlapping domain with NODAL. As a feedback inhibitor of NODAL, LEFTY2 also plays a similar role in limiting the range and temporal window of NODAL activation in the left LPM. Mutation of *Lefty2* in mouse results in prolonged NODAL expression and ectopic PITX2 expression on the right side (226).

While NODAL expression is rather transient, asymmetric PITX2 expression lasts over organogenesis and orchestrates lateralized morphogenesis. For instance, overexpression of PITX2 on the right side of the mouse embryo leads to defective heart and gut looping, as well as reversed body turning (215). The precise gene regulatory network and morphogenetic mechanism by which PITX2 instructs asymmetric development remain an active area of research. For instance, in avian gut development, PITX2 is asymmetrically expressed in the dorsal mesentery, a derivative of the LPM that anchors the gut tube to the posterior abdominal wall (232–234). PITX2 suppresses BMP4 on the left side of the dorsal mesentery, while right-sided BMP4 promotes hyaluronan-dependent tissue expansion (234,235). In response to this tissue deformation, PITX2 is upregulated via mechanosensitive TGF-β signaling and elevates tissue stiffness, which functions as a “brake” ensuring the proper gut tilting angle (234). This left-specific modulation of tissue stiffness is mediated by the PITX2 downstream effector formin DAAM2, which polymerizes the actin cytoskeleton and promotes cell-cell adhesion (236). As such, PITX2 orchestrates LR asymmetric morphogenesis, although its precise and comprehensive function in various organ-specific contexts is not fully understood.

Intersection of paraxial mesoderm and LR asymmetry

Bilateral symmetry has been assumed to be the default state of somitogenesis and somites (7,237–241). However, recent works on somite bilateral symmetry suggest that somitogenesis occurs in the context of multiple sources of asymmetry, which need to be buffered via various mechanisms to attain bilateral symmetry. For instance, a recent work in zebrafish suggests that nascent somites exhibit variability in anterior-posterior (AP) length and position and thus are asymmetric (242). Over maturation, pairs of contralateral somites gradually achieve more precise symmetry via shape adjustment based on tissue surface tension. This study reports a case of fluctuating asymmetry—that is, directionally unbiased, random deviation from perfect symmetry—introduced by developmental noise (243).

In addition, a series of works have investigated the role of the RA signaling pathway in ensuring symmetric somitogenesis despite the asymmetric signaling environment of LR patterning (244–248). In vertebrates, via yet unclear mechanisms, the absence of RA signaling results in a directionally biased defect in somitogenesis and somite asymmetry—a case of directional asymmetry—as the molecular processes in the PSM are exposed to the effect of LR patterning machineries. For instance, mutant mice for *Raldh2*, an enzyme synthesizing RA, result in LR desynchronization of somitogenesis where the right PSM displays delayed somite formation, manifested as fewer somites and an extended, occasionally right-biased, *Fgf8* mRNA domain (244). In addition, double mutants for *Raldh2* and *iv*, whose mutation randomizes situs, display somite formation defects on either the left or right side, demonstrating that the directionality of the somite formation defect upon RA deficiency is indeed downstream of LR determining signals (245,249). These findings suggest that bilateral symmetry is not the default state of somitogenesis but must be actively maintained by various mechanisms against various sources of asymmetry.

One reason somitogenesis and somites have been assumed to be symmetric is that asymmetric gene expression underlying LR patterning is most apparent in the LR organizer and the LPM, on which traditional research on LR patterning mainly focused. However, early somite development in the chick embryo spatially, temporally, and molecularly overlaps with LR patterning. Indeed, there are known, yet largely overlooked, instances of molecular asymmetry in the paraxial mesoderm that are exceedingly pertinent to somite development. For instance, Caronte/CER1 is a key signaling molecule in the LR pathway responsible for the propagation of NODAL to the left LPM, whose main function is BMP inhibition. While explant experiments showed that paraxial mesoderm tissue is necessary for peri-nodal SHH to induce NODAL in the LPM, CER1 is asymmetrically expressed by both the paraxial mesoderm and the LPM (199,206,207). This finding not only evidences molecular asymmetry of the paraxial mesoderm but also indicates that the left and right paraxial mesoderm are exposed to distinct signaling environments. For instance, the left paraxial mesoderm of the chick embryo experiences SHH and NODAL signaling as well as BMP inhibition by CER1. BMP signaling plays a critical role in mediolateral patterning of the somite and mesoderm in general (118–120). Thus, it is conceivable that the anterior-most somites, as well as the LPM at the same level, on the left side form before or during CER1 activation under weaker lateralizing effects due to BMP inhibition. In addition, one of the earliest traveling waves of Notch signaling oscillation has been shown to be asymmetric and crucial for the induction of NODAL at the HN (202,203). Specifically, the fifth traveling wave of *LFNG*, proposed to underlie the patterning of one of the occipital somites, is apparently asymmetric, as the left expression domain is more anteriorly positioned (203,250), and this asymmetry is lost upon treatments that perturb the upstream H^+/K^+-ATPase activity gradient (202). This finding provides strong evidence for not only the molecular asymmetry of

early somitogenesis but also the fundamental link between mechanisms underlying somitogenesis and LR patterning. However, the consequences of asymmetries in the molecular profile, signaling environment, and patterning of early somites have not been investigated.

Furthermore, the fact that most derivatives of the somite are apparently symmetric reinforced the assumption that somites are bilaterally symmetric. Indeed, the asymmetry of midline structures poses unique challenges to both observation and measurement, compared to bilaterally separate structures. However, various approaches have been taken to quantitatively analyze the asymmetry of somite-derived musculoskeletal structures (251–258). For instance, morphometric analysis of unaffected human thoracic vertebrae demonstrated a right bias in vertebral rotation and a left bias in pedicle length (252,257). The human sacrum also exhibits significant directional asymmetry in various morphometric parameters (258). As such, population-level directional asymmetry has been reported in human midline skeletal structures. In addition, idiopathic scoliosis, a major type of human spine deformity displaying curvature, is predominantly right-curved at the thoracic level, suggesting an intrinsic directional bias of the vertebrae (259,260). Interestingly, scoliosis patients whose organ situs are completely reversed (situs inversus) due to primary ciliary dyskinesia exhibit left-biased thoracic curvature, demonstrating that the convexity of idiopathic scoliosis correlates with the situs of the body (253). Although their developmental origin is yet unclear, directional asymmetries identified in both unaffected and scoliosis vertebrae strongly argue against the notion of symmetric vertebrae as the default state.

Thesis overview and roadmap

The findings described in the earlier chapter strongly suggest that bilateral symmetry is not the default state. Early somitogenesis proceeds with various sources of asymmetry. As such, beyond the traditional sets of organs and cell types, somites have the potential to serve as a paradigm for how bilateral symmetry is regulated in biology. Traditionally, however, somite bilateral symmetry has been studied only when it is obviously perturbed, and often with qualitative descriptions. In other words, with the assumption that somites are bilaterally symmetric, "whether" somites are symmetric has been primarily asked under specific perturbation conditions. Thus, whether somites are *actually* symmetric, or, more precisely, how symmetric somites are, is unknown.

The current thesis aims to provide a comprehensive characterization of bilateral asymmetry in the paraxial mesoderm and elucidate the modes by which LR asymmetry is regulated in the paraxial mesoderm. To this end, the asymmetry of the paraxial mesoderm will be operationalized and highlighted from multiple angles, including morphometry, gene expression, and developmental trajectories. This work is expected to provide a novel framework and foundation for future research in LR asymmetry while expanding the scope of LR asymmetry research beyond its traditional set of tissues and genes.

In the following chapters, first, morphological asymmetry of left and right somites, as well as gene expression asymmetry underlying somite patterning, will be measured to identify reproducible patterns of asymmetry in the wildtype chick embryo. Asking "how symmetric" with the view of symmetry as a continuum will be critical, as it will not only provide a more detailed, quantitative description of the system but also enable research on asymmetry in wildtype models. Next, the link between the LR determining pathway and somitogenesis will be determined. The effect of LR patterning signals on somite asymmetry patterns and somitogenesis dynamics will

be evaluated using both the chick embryo and an in vitro human iPSC model. Then, the molecular asymmetry of the early paraxial mesoderm will be demonstrated. Single-cell RNA sequencing and HCR RNA-FISH of the chick embryo are complementarily employed to identify novel gene expression asymmetry in the paraxial mesoderm. Finally, the asymmetry in developmental trajectories of the left and right somites will be demonstrated through side-specific fate mapping experiments using the chick embryo. The significance of the molecular laterality of the somite in the proper development of the embryo and in fate contribution will be additionally tested, leveraging the discoveries on somite molecular asymmetry.

REFERENCES

1. Pourquié O. Segmentation of the vertebrate spine: from clock to scoliosis. Cell. 2011 May 27;145(5):650–63. doi:10.1016/j.cell.2011.05.011 PubMed PMID: 21620133; PubMed Central PMCID: PMC3164975.

2. Christ B, Ordahl CP. Early stages of chick somite development. Anat Embryol. 1995 May 1;191(5):381–96. doi:10.1007/BF00304424

3. Miao Y, Pourquié O. Cellular and molecular control of vertebrate somitogenesis. Nat Rev Mol Cell Biol. 2024 Jul;25(7):517–33. doi:10.1038/s41580-024-00709-z

4. Kuratani S. Is the vertebrate head segmented?—evolutionary and developmental considerations. Integr Comp Biol. 2008 Nov 1;48(5):647–57. doi:10.1093/icb/icn015

5. Kuratani S, Schilling T. Head segmentation in vertebrates. Integr Comp Biol. 2008 Nov;48(5):604–10. doi:10.1093/icb/icn036 PubMed PMID: 20607135; PubMed Central PMCID: PMC2895339.

6. Cooke J, Zeeman EC. A clock and wavefront model for control of the number of repeated structures during animal morphogenesis. Journal of Theoretical Biology. 1976 Jan 1;58(2):455–76. doi:10.1016/S0022-5193(76)80131-2

7. Palmeirim I, Henrique D, Ish-Horowicz D, Pourquié O. Avian hairy Gene Expression Identifies a Molecular Clock Linked to Vertebrate Segmentation and Somitogenesis. Cell. 1997 Nov 28;91(5):639–48. doi:10.1016/S0092-8674(00)80451-1

8. Hamburger V, Hamilton HL. A series of normal stages in the development of the chick embryo. J Morphol. 1951 Jan;88(1):49–92. doi:10.1002/jmor.1050880104

9. Voiculescu O, Bertocchini F, Wolpert L, Keller RE, Stern CD. The amniote primitive streak is defined by epithelial cell intercalation before gastrulation. Nature. 2007 Oct;449(7165):1049–52. doi:10.1038/nature06211

10. Serrano Nájera G, Weijer CJ. Cellular processes driving gastrulation in the avian embryo. Mechanisms of Development. 2020 Sep 1;163:103624. doi:10.1016/j.mod.2020.103624

11. Waddington CH. III. Experiments on the development of chick and duck embryos, cultivated in vitro. Philos Trans R Soc Lond B Biol Sci. 1932 Jan 1;221(474–482):179–230. doi:10.1098/rstb.1932.0003

12. Waddington CH. Induction by the Primitive Streak and its Derivatives in the Chick. J Exp Biol. 1933 Jan 1;10(1):38–46. doi:10.1242/jeb.10.1.38

13. Stern CD. Hensen's Node: The Amniote Equivalent of Spemann's Organizer. In: Zagris N, Duprat AM, Durston A, editors. Organization of the Early Vertebrate Embryo [Internet].

Boston, MA: Springer US; 1995 [cited 2026 Mar 2]. p. 139–47. Available from: https://doi.org/10.1007/978-1-4899-1618-1_13 doi:10.1007/978-1-4899-1618-1_13

14. Selleck MAJ, Stern CD. Fate mapping and cell lineage analysis of Hensen's node in the chick embryo. Development. 1991 Jun 1;112(2):615–26. doi:10.1242/dev.112.2.615

15. Psychoyos D, Stern CD. Fates and migratory routes of primitive streak cells in the chick embryo. Development. 1996 May 1;122(5):1523–34. doi:10.1242/dev.122.5.1523

16. Yang X, Dormann D, Münsterberg AE, Weijer CJ. Cell Movement Patterns during Gastrulation in the Chick Are Controlled by Positive and Negative Chemotaxis Mediated by FGF4 and FGF8. Developmental Cell. 2002 Sep 1;3(3):425–37. doi:10.1016/S1534-5807(02)00256-3

17. Serrano Nájera G, Weijer CJ. Cellular processes driving gastrulation in the avian embryo. Mechanisms of Development. 2020 Sep 1;163:103624. doi:10.1016/j.mod.2020.103624

18. Gray SD, Dale JK. Notch signalling regulates the contribution of progenitor cells from the chick Hensen's node to the floor plate and notochord. Development. 2010 Feb 15;137(4):561–8. doi:10.1242/dev.041608

19. Schoenwolf GC. Histological and ultrastructural observations of tail bud formation in the chick embryo. The Anatomical Record. 1979;193(1):131–47. doi:10.1002/ar.1091930108

20. Beck CW. Development of the vertebrate tailbud. WIREs Developmental Biology. 2015;4(1):33–44. doi:10.1002/wdev.163

21. Prummel KD, Nieuwenhuize S, Mosimann C. The lateral plate mesoderm. Development. 2020 Jun 19;147(12):dev175059. doi:10.1242/dev.175059 PubMed PMID: 32561665; PubMed Central PMCID: PMC7328003.

22. Davidson AJ, Lewis P, Przepiorski A, Sander V. Turning mesoderm into kidney. Seminars in Cell & Developmental Biology. 2019 Jul 1;Craniofacial development91:86–93. doi:10.1016/j.semcdb.2018.08.016

23. Bothe I, Tenin G, Oseni A, Dietrich S. Dynamic control of head mesoderm patterning. Development. 2011 Jul 1;138(13):2807–21. doi:10.1242/dev.062737

24. Couly GF, Coltey PM, Le Douarin NM. The triple origin of skull in higher vertebrates: a study in quail-chick chimeras. Development. 1993 Feb 1;117(2):409–29. doi:10.1242/dev.117.2.409

25. Gomez C, Özbudak EM, Wunderlich J, Baumann D, Lewis J, Pourquié O. Control of segment number in vertebrate embryos. Nature. 2008 Jul;454(7202):335–9. doi:10.1038/nature07020

26. Kaplan KM, Spivak JM, Bendo JA. Embryology of the spine and associated congenital abnormalities. The Spine Journal. 2005 Sep 1;5(5):564–76. doi:10.1016/j.spinee.2004.10.044 PubMed PMID: 16153587.

27. Holley SA, Geisler R, Nüsslein-Volhard C. Control of her1 expression during zebrafish somitogenesis by a Delta-dependent oscillator and an independent wave-front activity. Genes Dev. 2000 Jan 7;14(13):1678–90. doi:10.1101/gad.14.13.1678 PubMed PMID: 10887161.

28. Bessho Y, Sakata R, Komatsu S, Shiota K, Yamada S, Kageyama R. Dynamic expression and essential functions of *Hes7* in somite segmentation. Genes Dev. 2001 Oct 15;15(20):2642–7. doi:10.1101/gad.930601

29. Henry CA, Urban MK, Dill KK, Merlie JP, Page MF, Kimmel CB, et al. Two linked hairy/Enhancer of split-related zebrafish genes, her1 and her7, function together to refine alternating somite boundaries. Development. 2002 Aug 1;129(15):3693–704. doi:10.1242/dev.129.15.3693

30. Lewis J. Autoinhibition with Transcriptional Delay: A Simple Mechanism for the Zebrafish Somitogenesis Oscillator. Current Biology. 2003 Aug 19;13(16):1398–408. doi:10.1016/S0960-9822(03)00534-7

31. Hirata H, Bessho Y, Kokubu H, Masamizu Y, Yamada S, Lewis J, et al. Instability of Hes7 protein is crucial for the somite segmentation clock. Nat Genet. 2004 Jul;36(7):750–4. doi:10.1038/ng1372 PubMed PMID: 15170214.

32. Oates AC. Waiting on the Fringe: cell autonomy and signaling delays in segmentation clocks. Current Opinion in Genetics & Development. 2020 Aug 1;Developmental Mechanisms, patterning and evolution63:61–70. doi:10.1016/j.gde.2020.04.008

33. Diaz-Cuadros M, Miettinen TP, Skinner OS, Sheedy D, Díaz-García CM, Gapon S, et al. Metabolic regulation of species-specific developmental rates. Nature. 2023 Jan 19;613(7944):550-5,557A-557T. doi:10.1038/s41586-022-05574-4

34. Matsuda M, Hayashi H, Garcia-Ojalvo J, Yoshioka-Kobayashi K, Kageyama R, Yamanaka Y, et al. Species-specific segmentation clock periods are due to differential biochemical reaction speeds. Science. 2020 Sep 18;369(6510):1450–5. doi:10.1126/science.aba7668

35. Lázaro J, Costanzo M, Sanaki-Matsumiya M, Girardot C, Hayashi M, Hayashi K, et al. A stem cell zoo uncovers intracellular scaling of developmental tempo across mammals. Cell Stem Cell. 2023 Jul 6;30(7):938-949.e7. doi:10.1016/j.stem.2023.05.014 PubMed PMID: 37343565.

36. Matsuda M, Lázaro J, Ebisuya M. Metabolic activities are selective modulators for individual segmentation clock processes. Nat Commun. 2025 Jan 20;16(1):845. doi:10.1038/s41467-025-56120-5

37. McGrew MJ, Dale JK, Fraboulet S, Pourquié O. The *lunatic Fringe* gene is a target of the molecular clock linked to somite segmentation in avian embryos. Current Biology. 1998 Aug 27;8(17):979–82. doi:10.1016/S0960-9822(98)70401-4

38. Morales AV, Yasuda Y, Ish-Horowicz D. Periodic *Lunatic fringe* Expression Is Controlled during Segmentation by a Cyclic Transcriptional Enhancer Responsive to Notch Signaling. Developmental Cell. 2002 Jul 1;3(1):63–74. doi:10.1016/S1534-5807(02)00211-3

39. Shimojo H, Isomura A, Ohtsuka T, Kori H, Miyachi H, Kageyama R. Oscillatory control of Delta-like1 in cell interactions regulates dynamic gene expression and tissue morphogenesis. Genes Dev. 2016 Jan 1;30(1):102–16. doi:10.1101/gad.270785.115 PubMed PMID: 26728556; PubMed Central PMCID: PMC4701973.

40. Dequéant ML, Glynn E, Gaudenz K, Wahl M, Chen J, Mushegian A, et al. A Complex Oscillating Network of Signaling Genes Underlies the Mouse Segmentation Clock. Science. 2006 Dec 8;314(5805):1595–8. doi:10.1126/science.1133141 PubMed PMID: 17095659.

41. Aulehla A, Wehrle C, Brand-Saberi B, Kemler R, Gossler A, Kanzler B, et al. Wnt3a plays a major role in the segmentation clock controlling somitogenesis. Dev Cell. 2003 Mar;4(3):395–406. doi:10.1016/s1534-5807(03)00055-8 PubMed PMID: 12636920.

42. Sonnen KF, Lauschke VM, Uraji J, Falk HJ, Petersen Y, Funk MC, et al. Modulation of Phase Shift between Wnt and Notch Signaling Oscillations Controls Mesoderm Segmentation. Cell. 2018 Feb 22;172(5):1079-1090.e12. doi:10.1016/j.cell.2018.01.026 PubMed PMID: 29474908; PubMed Central PMCID: PMC5847172.

43. Niwa Y, Masamizu Y, Liu T, Nakayama R, Deng CX, Kageyama R. The Initiation and Propagation of Hes7 Oscillation Are Cooperatively Regulated by Fgf and Notch Signaling in the Somite Segmentation Clock. Developmental Cell. 2007 Aug 7;13(2):298–304. doi:10.1016/j.devcel.2007.07.013

44. Feller J, Schneider A, Schuster-Gossler K, Gossler A. Noncyclic Notch activity in the presomitic mesoderm demonstrates uncoupling of somite compartmentalization and boundary formation. Genes Dev. 2008 Aug 15;22(16):2166–71. doi:10.1101/gad.480408 PubMed PMID: 18708576.

45. Aulehla A, Wiegraebe W, Baubet V, Wahl MB, Deng C, Taketo M, et al. A β-catenin gradient links the clock and wavefront systems in mouse embryo segmentation. Nat Cell Biol. 2008 Feb;10(2):186–93. doi:10.1038/ncb1679

46. Venzin OF, Oates AC. What are you synching about? Emerging complexity of Notch signaling in the segmentation clock. Developmental Biology. 2020 Apr 1;Systems Biology of Pattern Formation460(1):1. doi:10.1016/j.ydbio.2019.06.024

47. Jiang YJ, Aerne BL, Smithers L, Haddon C, Ish-Horowicz D, Lewis J. Notch signalling and the synchronization of the somite segmentation clock. Nature. 2000 Nov;408(6811):6811. doi:10.1038/35044091

48. Özbudak EM, Lewis J. Notch Signalling Synchronizes the Zebrafish Segmentation Clock but Is Not Needed To Create Somite Boundaries. PLOS Genetics. 2008 Spring;4(2):e15. doi:10.1371/journal.pgen.0040015

49. Yoshioka-Kobayashi K, Matsumiya M, Niino Y, Isomura A, Kori H, Miyawaki A, et al. Coupling delay controls synchronized oscillation in the segmentation clock. Nature. 2020 Apr;580(7801):119–23. doi:10.1038/s41586-019-1882-z

50. Dubrulle J, McGrew MJ, Pourquié O. FGF Signaling Controls Somite Boundary Position and Regulates Segmentation Clock Control of Spatiotemporal Hox Gene Activation. Cell. 2001 Jul 27;106(2):219–32. doi:10.1016/S0092-8674(01)00437-8

51. Dubrulle J, Pourquié O. fgf8 mRNA decay establishes a gradient that couples axial elongation to patterning in the vertebrate embryo. Nature. 2004 Jan 29;427(6973):419–22. doi:10.1038/nature02216 PubMed PMID: 14749824.

52. Sawada A, Shinya M, Jiang YJ, Kawakami A, Kuroiwa A, Takeda H. Fgf/MAPK signalling is a crucial positional cue in somite boundary formation. Development. 2001 Dec 1;128(23):4873–80. doi:10.1242/dev.128.23.4873

53. Stulberg MJ, Lin A, Zhao H, Holley SA. Crosstalk between Fgf and Wnt signaling in the zebrafish tailbud. Developmental Biology. 2012 Sep 15;369(2):298–307. doi:10.1016/j.ydbio.2012.07.003

54. Aulehla A, Pourquié O. Signaling Gradients during Paraxial Mesoderm Development. Cold Spring Harb Perspect Biol. 2010 Jan 2;2(2):a000869. doi:10.1101/cshperspect.a000869 PubMed PMID: 20182616.

55. Wittler L, Shin E ha, Grote P, Kispert A, Beckers A, Gossler A, et al. Expression of Msgn1 in the presomitic mesoderm is controlled by synergism of WNT signalling and Tbx6. EMBO Rep. 2007 Aug;8(8):784–9. doi:10.1038/sj.embor.7401030 PubMed PMID: 17668009; PubMed Central PMCID: PMC1978083.

56. White PH, Farkas DR, Chapman DL. Regulation of Tbx6 expression by Notch signaling. genesis. 2005;42(2):61–70. doi:10.1002/gene.20124

57. Yamaguchi TP, Bradley A, McMahon AP, Jones S. A Wnt5a pathway underlies outgrowth of multiple structures in the vertebrate embryo. Development. 1999 Mar 15;126(6):1211–23. doi:10.1242/dev.126.6.1211

58. Dunty WC Jr, Biris KK, Chalamalasetty RB, Taketo MM, Lewandoski M, Yamaguchi TP. Wnt3a/β-catenin signaling controls posterior body development by coordinating mesoderm formation and segmentation. Development. 2008 Jan 1;135(1):85–94. doi:10.1242/dev.009266

59. Niederreither K, McCaffery P, Dräger UC, Chambon P, Dollé P. Restricted expression and retinoic acid-induced downregulation of the retinaldehyde dehydrogenase type 2 (RALDH-

2) gene during mouse development. Mechanisms of Development. 1997 Feb 1;62(1):67–78. doi:10.1016/S0925-4773(96)00653-3

60. Sakai Y, Meno C, Fujii H, Nishino J, Shiratori H, Saijoh Y, et al. The retinoic acid-inactivating enzyme CYP26 is essential for establishing an uneven distribution of retinoic acid along the anterio-posterior axis within the mouse embryo. Genes Dev. 2001 Jan 15;15(2):213–25. doi:10.1101/gad.851501 PubMed PMID: 11157777.

61. del Corral RD, Olivera-Martinez I, Goriely A, Gale E, Maden M, Storey K. Opposing FGF and Retinoid Pathways Control Ventral Neural Pattern, Neuronal Differentiation, and Segmentation during Body Axis Extension. Neuron. 2003 Sep 25;40(1):65–79. doi:10.1016/S0896-6273(03)00565-8

62. Niwa Y, Shimojo H, Isomura A, González A, Miyachi H, Kageyama R. Different types of oscillations in Notch and Fgf signaling regulate the spatiotemporal periodicity of somitogenesis. Genes Dev. 2011 Jan 6;25(11):1115–20. doi:10.1101/gad.2035311 PubMed PMID: 21632822.

63. Akiyama R, Masuda M, Tsuge S, Bessho Y, Matsui T. An anterior limit of FGF/Erk signal activity marks the earliest future somite boundary in zebrafish. Development. 2014 Mar 1;141(5):1104–9. doi:10.1242/dev.098905

64. Simsek MF, Chandel AS, Saparov D, Zinani OQH, Clason N, Özbudak EM. Periodic inhibition of Erk activity drives sequential somite segmentation. Nature. 2023 Jan;613(7942):153–9. doi:10.1038/s41586-022-05527-x

65. Dias AS, de Almeida I, Belmonte JM, Glazier JA, Stern CD. Somites Without a Clock. Science. 2014 Feb 14;343(6172):791–5. doi:10.1126/science.1247575

66. Harima Y, Takashima Y, Ueda Y, Ohtsuka T, Kageyama R. Accelerating the tempo of the segmentation clock by reducing the number of introns in the Hes7 gene. Cell Rep. 2013 Jan 31;3(1):1–7. doi:10.1016/j.celrep.2012.11.012 PubMed PMID: 23219549.

67. Schröter C, Oates AC. Segment Number and Axial Identity in a Segmentation Clock Period Mutant. Current Biology. 2010 Jul 27;20(14):1254–8. doi:10.1016/j.cub.2010.05.071

68. Hoyle NP, Ish-Horowicz D. Transcript processing and export kinetics are rate-limiting steps in expressing vertebrate segmentation clock genes. Proceedings of the National Academy of Sciences. 2013 Nov 12;110(46):E4316–24. doi:10.1073/pnas.1308811110

69. Takashima Y, Ohtsuka T, González A, Miyachi H, Kageyama R. Intronic delay is essential for oscillatory expression in the segmentation clock. Proc Natl Acad Sci U S A. 2011 Feb 22;108(8):3300–5. doi:10.1073/pnas.1014418108 PubMed PMID: 21300886; PubMed Central PMCID: PMC3044385.

70. Diaz-Cuadros M, Wagner DE, Budjan C, Hubaud A, Tarazona OA, Donelly S, et al. In vitro characterization of the human segmentation clock. Nature. 2020 Apr;580(7801):113–8. doi:10.1038/s41586-019-1885-9

71. Diaz-Cuadros M, Pourquie O. In vitro systems: A new window to the segmentation clock. Development, Growth & Differentiation. 2021;63(2):140–53. doi:10.1111/dgd.12710

72. Oginuma M, Moncuquet P, Xiong F, Karoly E, Chal J, Guevorkian K, et al. A Gradient of Glycolytic Activity Coordinates FGF and Wnt Signaling during Elongation of the Body Axis in Amniote Embryos. Developmental Cell. 2017 Feb 27;40(4):342-353.e10. doi:10.1016/j.devcel.2017.02.001 PubMed PMID: 28245921.

73. Oginuma M, Harima Y, Tarazona OA, Diaz-Cuadros M, Michaut A, Ishitani T, et al. Intracellular pH controls WNT downstream of glycolysis in amniote embryos. Nature. 2020 Aug;584(7819):98–101. doi:10.1038/s41586-020-2428-0

74. Bulusu V, Prior N, Snaebjornsson MT, Kuehne A, Sonnen KF, Kress J, et al. Spatiotemporal Analysis of a Glycolytic Activity Gradient Linked to Mouse Embryo Mesoderm Development. Dev Cell. 2017 Feb 27;40(4):331-341.e4. doi:10.1016/j.devcel.2017.01.015 PubMed PMID: 28245920; PubMed Central PMCID: PMC5337618.

75. Hubaud A, Pourquié O. Signalling dynamics in vertebrate segmentation. Nat Rev Mol Cell Biol. 2014 Nov;15(11):11. doi:10.1038/nrm3891

76. Yaman YI, Ramanathan S. Controlling human organoid symmetry breaking reveals signaling gradients drive segmentation clock waves. Cell. 2023 Feb 2;186(3):513-527.e19. doi:10.1016/j.cell.2022.12.042

77. Liao BK, Jörg DJ, Oates AC. Faster embryonic segmentation through elevated Delta-Notch signalling. Nat Commun. 2016 Jun 15;7(1):11861. doi:10.1038/ncomms11861

78. González A, Manosalva I, Liu T, Kageyama R. Control of Hes7 Expression by Tbx6, the Wnt Pathway and the Chemical Gsk3 Inhibitor LiCl in the Mouse Segmentation Clock. PLoS One. 2013 Jan 9;8(1):e53323. doi:10.1371/journal.pone.0053323 PubMed PMID: 23326414; PubMed Central PMCID: PMC3541138.

79. Haraguchi S, Kitajima S, Takagi A, Takeda H, Inoue T, Saga Y. Transcriptional regulation of *Mesp1* and *Mesp2* genes: differential usage of enhancers during development. Mechanisms of Development. 2001 Oct 1;108(1):59–69. doi:10.1016/S0925-4773(01)00478-6

80. Saga Y, Hata N, Koseki H, Taketo MM. Mesp2: a novel mouse gene expressed in the presegmented mesoderm and essential for segmentation initiation. Genes Dev. 1997 Jul 1;11(14):1827–39. doi:10.1101/gad.11.14.1827 PubMed PMID: 9242490.

81. Yasuhiko Y, Haraguchi S, Kitajima S, Takahashi Y, Kanno J, Saga Y. Tbx6-mediated Notch signaling controls somite-specific Mesp2 expression. Proc Natl Acad Sci U S A. 2006 Mar

7;103(10):3651–6. doi:10.1073/pnas.0508238103 PubMed PMID: 16505380; PubMed Central PMCID: PMC1450137.

82. Yasuhiko Y, Kitajima S, Takahashi Y, Oginuma M, Kagiwada H, Kanno J, et al. Functional importance of evolutionally conserved Tbx6 binding sites in the presomitic mesoderm-specific enhancer of Mesp2. Development. 2008 Nov 1;135(21):3511–9. doi:10.1242/dev.027144

83. Oginuma M, Niwa Y, Chapman DL, Saga Y. Mesp2 and Tbx6 cooperatively create periodic patterns coupled with the clock machinery during mouse somitogenesis. Development. 2008 Aug 1;135(15):2555–62. doi:10.1242/dev.019877

84. Morimoto M, Takahashi Y, Endo M, Saga Y. The Mesp2 transcription factor establishes segmental borders by suppressing Notch activity. Nature. 2005 May;435(7040):354–9. doi:10.1038/nature03591

85. Morimoto M, Sasaki N, Oginuma M, Kiso M, Igarashi K, Aizaki K ichi, et al. The negative regulation of Mesp2 by mouse Ripply2 is required to establish the rostro-caudal patterning within a somite. Development. 2007 Apr 15;134(8):1561–9. doi:10.1242/dev.000836

86. Takahashi Y, Koizumi K ichi, Takagi A, Kitajima S, Inoue T, Koseki H, et al. Mesp2 initiates somite segmentation through the Notch signalling pathway. Nat Genet. 2000 Aug;25(4):390–6. doi:10.1038/78062

87. Takahashi Y, Yasuhiko Y, Kitajima S, Kanno J, Saga Y. Appropriate suppression of Notch signaling by Mesp factors is essential for stripe pattern formation leading to segment boundary formation. Developmental Biology. 2007 Apr 15;304(2):593–603. doi:10.1016/j.ydbio.2007.01.007

88. Durbin L, Brennan C, Shiomi K, Cooke J, Barrios A, Shanmugalingam S, et al. Eph signaling is required for segmentation and differentiation of the somites. Genes Dev. 1998 Jan 10;12(19):3096–109. doi:10.1101/gad.12.19.3096

89. Baker RK, Antin PB. Ephs and ephrins during early stages of chick embryogenesis. Developmental Dynamics. 2003;228(1):128–42. doi:10.1002/dvdy.10354

90. Watanabe T, Sato Y, Saito D, Tadokoro R, Takahashi Y. EphrinB2 coordinates the formation of a morphological boundary and cell epithelialization during somite segmentation. PNAS. 2009 May 5;106(18):7467–72. doi:10.1073/pnas.0902859106 PubMed PMID: 19380726.

91. Kraus F, Haenig B, Kispert A. Cloning and expression analysis of the mouse T-box gene *Tbx18*. Mechanisms of Development. 2001 Jan 1;100(1):83–6. doi:10.1016/S0925-4773(00)00494-9

92. Neidhardt LM, Kispert A, Herrmann BG. A mouse gene of the paired-related homeobox class expressed in the caudal somite compartment and in the developing vertebral column,

kidney and nervous system. Dev Gene Evol. 1997 Nov 1;207(5):330–9. doi:10.1007/s004270050120

93. Bussen M, Petry M, Schuster-Gossler K, Leitges M, Gossler A, Kispert A. The T-box transcription factor Tbx18 maintains the separation of anterior and posterior somite compartments. Genes & development. 2004 Jun 1;18:1209–21. doi:10.1101/gad.300104

94. Miao Y, Djeffal Y, De Simone A, Zhu K, Lee JG, Lu Z, et al. Reconstruction and deconstruction of human somitogenesis in vitro. Nature. 2022 Dec 21;1–9. doi:10.1038/s41586-022-05655-4

95. Barrios A, Poole RJ, Durbin L, Brennan C, Holder N, Wilson SW. Eph/Ephrin Signaling Regulates the Mesenchymal-to-Epithelial Transition of the Paraxial Mesoderm during Somite Morphogenesis. Current Biology. 2003 Sep 16;13(18):1571–82. doi:10.1016/j.cub.2003.08.030

96. Naganathan SR, Oates AC. Patterning and mechanics of somite boundaries in zebrafish embryos. Seminars in Cell & Developmental Biology. 2020 Nov 1;1. Cyclins edited by Josep Clotet107:170–8. doi:10.1016/j.semcdb.2020.04.014

97. Dahmann C, Oates AC, Brand M. Boundary formation and maintenance in tissue development. Nat Rev Genet. 2011 Jan;12(1):43–55. doi:10.1038/nrg2902

98. Nakajima Y, Morimoto M, Takahashi Y, Koseki H, Saga Y. Identification of Epha4 enhancer required for segmental expression and the regulation by Mesp2. Development. 2006 Jul 1;133(13):2517–25. doi:10.1242/dev.02422

99. Nomura-Kitabayashi A, Takahashi Y, Kitajima S, Inoue T, Takeda H, Saga Y. Hypomorphic Mesp allele distinguishes establishment of rostrocaudal polarity and segment border formation in somitogenesis. Development. 2002 May 15;129(10):2473–81. doi:10.1242/dev.129.10.2473

100. Nakaya Y, Kuroda S, Katagiri YT, Kaibuchi K, Takahashi Y. Mesenchymal-Epithelial Transition during Somitic Segmentation Is Regulated by Differential Roles of Cdc42 and Rac1. Developmental Cell. 2004 Sep 1;7(3):425–38. doi:10.1016/j.devcel.2004.08.003 PubMed PMID: 15363416.

101. Jülich D, Mould AP, Koper E, Holley SA. Control of extracellular matrix assembly along tissue boundaries via Integrin and Eph/Ephrin signaling. Development. 2009 Sep 1;136(17):2913–21. doi:10.1242/dev.038935

102. Koshida S, Kishimoto Y, Ustumi H, Shimizu T, Furutani-Seiki M, Kondoh H, et al. Integrinα5-Dependent Fibronectin Accumulation for Maintenance of Somite Boundaries in Zebrafish Embryos. Developmental Cell. 2005 Apr 1;8(4):587–98. doi:10.1016/j.devcel.2005.03.006 PubMed PMID: 15809040.

103. Palmeirim I, Dubrulle J, Henrique D, Ish-Horowicz D, Pourquié O. Uncoupling segmentation and somitogenesis in the chick presomitic mesoderm. Developmental

Genetics. 1998;23(1):77–85. doi:10.1002/(SICI)1520-6408(1998)23:1<77::AID-DVG8>3.0.CO;2-3

104. Correia KM, Conlon RA. Surface ectoderm is necessary for the morphogenesis of somites. Mechanisms of Development. 2000 Mar 1;91(1):19–30. doi:10.1016/S0925-4773(99)00260-9

105. Rifes P, Carvalho L, Lopes C, Andrade RP, Rodrigues G, Palmeirim I, et al. Redefining the role of ectoderm in somitogenesis: a player in the formation of the fibronectin matrix of presomitic mesoderm. Development. 2007 Sep 1;134(17):3155–65. doi:10.1242/dev.003665

106. Llić D, Furuta Y, Kanazawa S, Takeda N, Sobue K, Nakatsuji N, et al. Reduced cell motility and enhanced focal adhesion contact formation in cells from FAK-deficient mice. Nature. 1995 Oct;377(6549):539–44. doi:10.1038/377539a0

107. Burgess R, Rawls A, Brown D, Bradley A, Olson EN. Requirement of the paraxis gene for somite formation and musculoskeletal patterning. Nature. 1996 Dec;384(6609):570–3. doi:10.1038/384570a0

108. Rowton M, Ramos P, Anderson DM, Rhee JM, Cunliffe HE, Rawls A. Regulation of mesenchymal-to-epithelial transition by PARAXIS during somitogenesis. Dev Dyn. 2013 Nov;242(11):1332–44. doi:10.1002/dvdy.24033 PubMed PMID: 24038871.

109. Chal J, Pourquié O. Patterning and differentiation of the vertebrate spine. The Skeletal System. 2009 Jan 1;41–116. doi:10.1101/087969825.53.41

110. Duband JL, Thiery JP. Distribution of laminin and collagens during avian neural crest development. Development. 1987 Nov 1;101(3):461–78. doi:10.1242/dev.101.3.461

111. Johnson J, Rhee J, Parsons SM, Brown D, Olson EN, Rawls A. The Anterior/Posterior Polarity of Somites Is Disrupted in Paraxis-Deficient Mice. Developmental Biology. 2001 Jan 1;229(1):176–87. doi:10.1006/dbio.2000.9969

112. Linker C, Lesbros C, Gros J, Burrus LW, Rawls A, Marcelle C. β-Catenin-dependent Wnt signalling controls the epithelial organisation of somites through the activation of paraxis. Development. 2005 Sep 1;132(17):3895–905. doi:10.1242/dev.01961

113. Ebensperger C, Wilting J, Brand-Saberi B, Mizutani Y, Christ B, Balling R, et al. Pax-1, a regulator of sclerotome development is induced by notochord and floor plate signals in avian embryos. Anat Embryol. 1995 Apr 1;191(4):297–310. doi:10.1007/BF00534682

114. Aoyama H, Asamoto K. Determination of somite cells: independence of cell differentiation and morphogenesis. Development. 1988 Sep 1;104(1):15–28. doi:10.1242/dev.104.1.15

115. Brand-Saberi B, Ebensperger C, Wilting J, Balling R, Christ B. The ventralizing effect of the notochord on somite differentiation in chick embryos. Anat Embryol. 1993 Sep 1;188(3):239–45. doi:10.1007/BF00188215

116. Pourquié O, Coltey M, Teillet MA, Ordahl C, Le Douarin NM. Control of dorsoventral patterning of somitic derivatives by notochord and floor plate. Proceedings of the National Academy of Sciences. 1993 Jun;90(11):5242–6. doi:10.1073/pnas.90.11.5242

117. Dockter J, Ordahl CP. Dorsoventral axis determination in the somite: a re-examination. Development. 2000 May 15;127(10):2201–6. doi:10.1242/dev.127.10.2201

118. Tonegawa A, Funayama N, Ueno N, Takahashi Y. Mesodermal subdivision along the mediolateral axis in chicken controlled by different concentrations of BMP-4. Development. 1997 May 15;124(10):1975–84. doi:10.1242/dev.124.10.1975

119. Pourquié O, Coltey M, Bréant C, Le Douarin NM. Control of somite patterning by signals from the lateral plate. Proceedings of the National Academy of Sciences. 1995 Apr 11;92(8):3219–23. doi:10.1073/pnas.92.8.3219

120. Pourquié O, Fan CM, Coltey M, Hirsinger E, Watanabe Y, Bréant C, et al. Lateral and Axial Signals Involved in Avian Somite Patterning: A Role for BMP4. Cell. 1996 Feb 9;84(3):461–71. doi:10.1016/S0092-8674(00)81291-X

121. Monsoro-Burq AH, Duprez D, Watanabe Y, Bontoux M, Vincent C, Brickell P, et al. The role of bone morphogenetic proteins in vertebral development. Development. 1996 Nov 1;122(11):3607–16. doi:10.1242/dev.122.11.3607

122. Bronner-Fraser M. 9 Rostrocaudal Differences within the Somites Confer Segmental Pattern to Trunk Neural Crest Migration. In: Current Topics in Developmental Biology [Internet]. Academic Press; 1999 [cited 2026 Apr 19]. p. 279–96. Available from: https://www.sciencedirect.com/science/chapter/bookseries/abs/pii/S0070215308607280 doi:10.1016/S0070-2153(08)60728-0

123. Oakley RA, Tosney KW. Peanut agglutinin and chondroitin-6-sulfate are molecular markers for tissues that act as barriers to axon advance in the avian embryo. Developmental Biology. 1991 Sep 1;147(1):187–206. doi:10.1016/S0012-1606(05)80017-X

124. Landolt RM, Vaughan L, Winterhalter KH, Zimmermann DR. Versican is selectively expressed in embryonic tissues that act as barriers to neural crest cell migration and axon outgrowth. Development. 1995 Aug 1;121(8):2303–12. doi:10.1242/dev.121.8.2303

125. Debby-Brafman A, Burstyn-Cohen T, Klar A, Kalcheim C. F-Spondin, Expressed in Somite Regions Avoided by Neural Crest Cells, Mediates Inhibition of Distinct Somite Domains to Neural Crest Migration. Neuron. 1999 Mar 1;22(3):475–88. doi:10.1016/S0896-6273(00)80703-5 PubMed PMID: 10197528.

126. Fan CM, Tessier-Lavigne M. Patterning of mammalian somites by surface ectoderm and notochord: Evidence for sclerotome induction by a hedgehog homolog. Cell. 1994 Dec 30;79(7):1175–86. doi:10.1016/0092-8674(94)90009-4

127. Fan CM, Lee CS, Tessier-Lavigne M. A Role for WNT Proteins in Induction of Dermomyotome. Developmental Biology. 1997 Nov 1;191(1):160–5. doi:10.1006/dbio.1997.8713

128. Lee CS, Buttitta LA, May NR, Kispert A, Fan CM. SHH-N upregulates Sfrp2 to mediate its competitive interaction with WNT1 and WNT4 in the somitic mesoderm. Development. 2000 Jan 1;127(1):109–18. doi:10.1242/dev.127.1.109

129. Lee CS, Buttitta L, Fan CM. Evidence that the WNT-inducible growth arrest-specific gene 1 encodes an antagonist of sonic hedgehog signaling in the somite. Proceedings of the National Academy of Sciences. 2001 Sep 25;98(20):11347–52. doi:10.1073/pnas.201418298

130. Gros J, Scaal M, Marcelle C. A Two-Step Mechanism for Myotome Formation in Chick. Developmental Cell. 2004 Jun 1;6(6):875–82. doi:10.1016/j.devcel.2004.05.006 PubMed PMID: 15177035.

131. Geetha-Loganathan P, Nimmagadda S, Huang R, Christ B, Scaal M. Regulation of ectodermal Wnt6 expression by the neural tube is transduced by dermomyotomal Wnt11: a mechanism of dermomyotomal lip sustainment. Development. 2006 Aug 1;133(15):2897–904. doi:10.1242/dev.02464

132. Christ B, Scaal M. Formation and Differentiation of Avian Somite Derivatives. In: Maroto M, Whittock NV, editors. Somitogenesis [Internet]. New York, NY: Springer; 2009 [cited 2026 Apr 19]. p. 1–41. Available from: https://doi.org/10.1007/978-0-387-09606-3_1 doi:10.1007/978-0-387-09606-3_1

133. Christ B, Huang R, Wilting J. The development of the avian vertebral column. Anat Embryol. 2000 Aug 1;202(3):179–94. doi:10.1007/s004290000114

134. Maschner A, Krück S, Draga M, Pröls F, Scaal M. Developmental dynamics of occipital and cervical somites. J Anat. 2016 Nov;229(5):601–9. doi:10.1111/joa.12516 PubMed PMID: 27380812; PubMed Central PMCID: PMC5055085.

135. Huang R, Zhi Q, Patel K, Wilting J, Christ B. Contribution of single somites to the skeleton and muscles of the occipital and cervical regions in avian embryos. Anat Embryol. 2000 Oct 1;202(5):375–83. doi:10.1007/s004290000131

136. Lim TM, Lunn ER, Keynes RJ, Stern CD. The differing effects of occipital and trunk somites on neural development in the chick embryo. Development. 1987 Jul 1;100(3):525–33. doi:10.1242/dev.100.3.525

137. Pu Q, Bai Z, Haque Z, Wang J, Huang R. Occipital somites guide motor axons of the accessory nerve in the avian embryo. Neuroscience. 2013 Aug 29;246:22–7. doi:10.1016/j.neuroscience.2013.04.039

138. Rodrigues S, Santos J, Palmeirim I. Molecular characterization of the rostral-most somites in early somitic stages of the chick embryo. Gene Expression Patterns. 2006 Oct 1;6(7):673–7. doi:10.1016/j.modgep.2006.01.004

139. Tam PPL. The control of somitogenesis in mouse embryos. Development. 1981 Oct 1;65(Supplement):103–28. doi:10.1242/dev.65.Supplement.103

140. Maia-Fernandes AC, Martins-Jesus A, Borralho-Martins N, Pais-de-Azevedo T, Magno R, Duarte I, et al. Spatio-temporal dynamics of early somite segmentation in the chicken embryo. PLoS One. 2024 Apr 18;19(4):e0297853. doi:10.1371/journal.pone.0297853 PubMed PMID: 38635504; PubMed Central PMCID: PMC11025740.

141. Chalamalasetty RB, Garriock RJ, Dunty WC Jr, Kennedy MW, Jailwala P, Si H, et al. Mesogenin 1 is a master regulator of paraxial presomitic mesoderm differentiation. Development. 2014 Nov 15;141(22):4285–97. doi:10.1242/dev.110908

142. Oates AC, Rohde LA, Ho RK. Generation of segment polarity in the paraxial mesoderm of the zebrafish through a T-box-dependent inductive event. Developmental Biology. 2005 Jul 1;283(1):204–14. doi:10.1016/j.ydbio.2005.04.012

143. Oates AC, Ho RK. Hairy/E(spl)-related (Her) genes are central components of the segmentation oscillator and display redundancy with the Delta/Notch signaling pathway in the formation of anterior segmental boundaries in the zebrafish. Development. 2002 Jun 15;129(12):2929–46. doi:10.1242/dev.129.12.2929

144. Therapontos C, Vargesson N. Zebrafish notch signalling pathway mutants exhibit trunk vessel patterning anomalies that are secondary to somite misregulation. Developmental dynamics : an official publication of the American Association of Anatomists. 2010 Oct 1;239:2761–8. doi:10.1002/dvdy.22410

145. Freitas C, Rodrigues S, Charrier JB, Teillet MA, Palmeirim I. Evidence for medial/lateral specification and positional information within the presomitic mesoderm. Development. 2001 Dec 15;128(24):5139–47. doi:10.1242/dev.128.24.5139

146. Borman WH, Urlakis JR. KJ, Yorde DE. Analysis of the in vivo myogenic status of chick somites by desmin expression in vitro. Developmental Dynamics. 1994;199(4):268–79. doi:10.1002/aja.1001990403

147. Borman WH, Yorde DE. Analysis of chick somite myogenesis by in situ confocal microscopy of desmin expression. J Histochem Cytochem. 1994 Feb 1;42(2):265–72. doi:10.1177/42.2.8288867

148. Kant R, Goldstein RS. Plasticity of axial identity among somites: cranial somites can generate vertebrae without expressing Hox genes appropriate to the trunk. Dev Biol. 1999 Dec 15;216(2):507–20. doi:10.1006/dbio.1999.9512 PubMed PMID: 10642789.

149. Kieny M, Mauger A, Sengel P. Early regionalization of the somitic mesoderm as studied by the development of the axial skeleton of the chick embryo. Developmental Biology. 1972 May 1;28(1):142–61. doi:10.1016/0012-1606(72)90133-9

150. Guibentif C, Griffiths JA, Imaz-Rosshandler I, Ghazanfar S, Nichols J, Wilson V, et al. Diverse Routes toward Early Somites in the Mouse Embryo. Dev Cell. 2021 Jan 11;56(1):141-153.e6. doi:10.1016/j.devcel.2020.11.013 PubMed PMID: 33308481; PubMed Central PMCID: PMC7808755.

151. Kinder SJ, Tsang TE, Quinlan GA, Hadjantonakis AK, Nagy A, Tam PPL. The orderly allocation of mesodermal cells to the extraembryonic structures and the anteroposterior axis during gastrulation of the mouse embryo. Development. 1999 Nov 1;126(21):4691–701. doi:10.1242/dev.126.21.4691

152. Vandenberg LN, Levin M. A unified model for left–right asymmetry? Comparison and synthesis of molecular models of embryonic laterality. Developmental Biology. 2013 Jul 1;379(1):1–15. doi:10.1016/j.ydbio.2013.03.021

153. Peeters H, Devriendt K. Human laterality disorders. European Journal of Medical Genetics. 2006 Sep 1;49(5):349–62. doi:10.1016/j.ejmg.2005.12.003

154. Grande C, Patel NH. Nodal signalling is involved in left–right asymmetry in snails. Nature. 2009 Feb;457(7232):1007–11. doi:10.1038/nature07603

155. Grimes DT. Making and breaking symmetry in development, growth and disease. Development. 2019 Aug 15;146(16):dev170985. doi:10.1242/dev.170985

156. Chea HK, Wright CV, Swalla BJ. Nodal signaling and the evolution of deuterostome gastrulation. Developmental Dynamics. 2005;234(2):269–78. doi:10.1002/dvdy.20549

157. Blum M, Feistel K, Thumberger T, Schweickert A. The evolution and conservation of left-right patterning mechanisms. Development. 2014 Apr 15;141(8):1603–13. doi:10.1242/dev.100560

158. Nonaka S, Tanaka Y, Okada Y, Takeda S, Harada A, Kanai Y, et al. Randomization of Left–Right Asymmetry due to Loss of Nodal Cilia Generating Leftward Flow of Extraembryonic Fluid in Mice Lacking KIF3B Motor Protein. Cell. 1998 Dec 11;95(6):829–37. doi:10.1016/S0092-8674(00)81705-5

159. Nonaka S, Yoshiba S, Watanabe D, Ikeuchi S, Goto T, Marshall WF, et al. De Novo Formation of Left–Right Asymmetry by Posterior Tilt of Nodal Cilia. PLoS Biol. 2005 Aug;3(8):e268. doi:10.1371/journal.pbio.0030268 PubMed PMID: 16035921; PubMed Central PMCID: PMC1180513.

160. Okada Y, Takeda S, Tanaka Y, Belmonte JCI, Hirokawa N. Mechanism of Nodal Flow: A Conserved Symmetry Breaking Event in Left-Right Axis Determination. Cell. 2005 May 20;121(4):633–44. doi:10.1016/j.cell.2005.04.008 PubMed PMID: 15907475.

161. Cartwright JHE, Piro O, Tuval I. Fluid-dynamical basis of the embryonic development of left-right asymmetry in vertebrates. Proceedings of the National Academy of Sciences. 2004 May 11;101(19):7234–9. doi:10.1073/pnas.0402001101

162. Nonaka S, Shiratori H, Saijoh Y, Hamada H. Determination of left–right patterning of the mouse embryo by artificial nodal flow. Nature. 2002 Jul;418(6893):96–9. doi:10.1038/nature00849

163. McGrath J, Somlo S, Makova S, Tian X, Brueckner M. Two populations of node monocilia initiate left-right asymmetry in the mouse. Cell. 2003 Jul 11;114(1):61–73. doi:10.1016/s0092-8674(03)00511-7 PubMed PMID: 12859898.

164. Tabin CJ, Vogan KJ. A two-cilia model for vertebrate left-right axis specification. Genes Dev. 2003 Jan 1;17(1):1–6. doi:10.1101/gad.1053803 PubMed PMID: 12514094.

165. Tanaka Y, Okada Y, Hirokawa N. FGF-induced vesicular release of Sonic hedgehog and retinoic acid in leftward nodal flow is critical for left–right determination. Nature. 2005 May;435(7039):172–7. doi:10.1038/nature03494

166. Hirokawa N, Tanaka Y, Okada Y, Takeda S. Nodal Flow and the Generation of Left-Right Asymmetry. Cell. 2006 Apr 7;125(1):33–45. doi:10.1016/j.cell.2006.03.002 PubMed PMID: 16615888.

167. Katoh TA, Omori T, Mizuno K, Sai X, Minegishi K, Ikawa Y, et al. Immotile cilia mechanically sense the direction of fluid flow for left-right determination. Science. 2023 Jan 6;379(6627):66–71. doi:10.1126/science.abq8148

168. Djenoune L, Mahamdeh M, Truong TV, Nguyen CT, Fraser SE, Brueckner M, et al. Cilia function as calcium-mediated mechanosensors that instruct left-right asymmetry. Science. 2023 Jan 6;379(6627):71–8. doi:10.1126/science.abq7317

169. Lee H, Camuto CM, Niehrs C. R-Spondin 2 governs Xenopus left-right body axis formation by establishing an FGF signaling gradient. Nat Commun. 2024 Feb 2;15(1):1003. doi:10.1038/s41467-024-44951-7

170. Tanaka Y, Morozumi A, Hirokawa N. Nodal flow transfers polycystin to determine mouse left-right asymmetry. Developmental Cell. 2023 Aug 21;58(16):1447-1461.e6. doi:10.1016/j.devcel.2023.06.002 PubMed PMID: 37413993.

171. Ott T, Brugger A, Szenker-Ravi E, Kurrle Y, Aberle O, Tisler M, et al. MMP21 behaves as a fluid flow transported morphogen to impart laterality during development [Internet]. bioRxiv; 2024 [cited 2026 Apr 20]. p. 2024.10.13.618030. Available from: https://www.biorxiv.org/content/10.1101/2024.10.13.618030v2 doi:10.1101/2024.10.13.618030

172. Kreiling JA, Prabhat, Williams G, Creton R. Analysis of Kupffer's vesicle in zebrafish embryos using a cave automated virtual environment. Developmental Dynamics. 2007;236(7):1963–9. doi:10.1002/dvdy.21191

173. Okabe N, Xu B, Burdine RD. Fluid dynamics in zebrafish Kupffer's vesicle. Developmental Dynamics. 2008;237(12):3602–12. doi:10.1002/dvdy.21730

174. Essner JJ, Amack JD, Nyholm MK, Harris EB, Yost HJ. Kupffer's vesicle is a ciliated organ of asymmetry in the zebrafish embryo that initiates left-right development of the brain, heart and gut. Development. 2005 Mar 15;132(6):1247–60. doi:10.1242/dev.01663

175. Schweickert A, Weber T, Beyer T, Vick P, Bogusch S, Feistel K, et al. Cilia-Driven Leftward Flow Determines Laterality in Xenopus. Current Biology. 2007 Jan 9;17(1):60–6. doi:10.1016/j.cub.2006.10.067 PubMed PMID: 17208188.

176. Afzelius BA. A Human Syndrome Caused by Immotile Cilia. Science. 1976;193(4250):317–9.

177. McManus IC, Martin N, Stubbings GF, Chung EMK, Mitchison HM. Handedness and situs inversus in primary ciliary dyskinesia. Proc Biol Sci. 2004 Dec 22;271(1557):2579–82. doi:10.1098/rspb.2004.2881

178. Vandenberg LN, Levin M. Perspectives and open problems in the early phases of left–right patterning. Seminars in Cell & Developmental Biology. 2009 Jun 1;The Molecular and Cellular Mechanisms in the Development of Addiction20(4):456–63. doi:10.1016/j.semcdb.2008.11.010

179. Bunney TD, De Boer AH, Levin M. Fusicoccin signaling reveals 14-3-3 protein function as a novel step in left-right patterning during amphibian embryogenesis. Development. 2003 Oct 15;130(20):4847–58. doi:10.1242/dev.00698

180. Kramer KL, Barnette JE, Yost HJ. PKCγ Regulates Syndecan-2 Inside-Out Signaling during *Xenopus* Left-Right Development. Cell. 2002 Dec 27;111(7):981–90. doi:10.1016/S0092-8674(02)01200-X

181. Ohkawara B, Niehrs C. An ATF2-based luciferase reporter to monitor non-canonical Wnt signaling in xenopus embryos. Developmental Dynamics. 2011;240(1):188–94. doi:10.1002/dvdy.22500

182. Aw S, Adams DS, Qiu D, Levin M. H,K-ATPase protein localization and Kir4.1 function reveal concordance of three axes during early determination of left–right asymmetry. Mechanisms of Development. 2008 Mar 1;125(3):353–72. doi:10.1016/j.mod.2007.10.011

183. Fukumoto T, Kema IP, Levin M. Serotonin Signaling Is a Very Early Step in Patterning of the Left-Right Axis in Chick and Frog Embryos. Current Biology. 2005 May 10;15(9):794–803. doi:10.1016/j.cub.2005.03.044 PubMed PMID: 15886096.

184. Hozumi S, Maeda R, Taniguchi K, Kanai M, Shirakabe S, Sasamura T, et al. An unconventional myosin in Drosophila reverses the default handedness in visceral organs. Nature. 2006 Apr;440(7085):798–802. doi:10.1038/nature04625

185. Thitamadee S, Tuchihara K, Hashimoto T. Microtubule basis for left-handed helical growth in Arabidopsis. Nature. 2002 May;417(6885):193–6. doi:10.1038/417193a

186. Adams DS, Robinson KR, Fukumoto T, Yuan S, Albertson RC, Yelick P, et al. Early, H+-V-ATPase-dependent proton flux is necessary for consistent left-right patterning of non-mammalian vertebrates. Development. 2006 May 1;133(9):1657–71. doi:10.1242/dev.02341

187. Qiu D, Cheng SM, Wozniak L, McSweeney M, Perrone E, Levin M. Localization and loss-of-function implicates ciliary proteins in early, cytoplasmic roles in left-right asymmetry. Developmental Dynamics. 2005;234(1):176–89. doi:10.1002/dvdy.20509

188. Shylo NA, Smith SE, Price AJ, Guo F, McClain M, Trainor PA. Morphological changes and two Nodal paralogs drive left-right asymmetry in the squamate veiled chameleon (C. calyptratus). Front Cell Dev Biol. 2023 Apr 11;11. doi:10.3389/fcell.2023.1132166

189. Kajikawa E, Horo U, Ide T, Mizuno K, Minegishi K, Hara Y, et al. Nodal paralogues underlie distinct mechanisms for visceral left–right asymmetry in reptiles and mammals. Nat Ecol Evol. 2020 Feb;4(2):261–9. doi:10.1038/s41559-019-1072-2

190. Gros J, Feistel K, Viebahn C, Blum M, Tabin CJ. Cell Movements at Hensen's Node Establish Left/Right Asymmetric Gene Expression in the Chick. Science. 2009 May 15;324(5929):941–4. doi:10.1126/science.1172478

191. Cooke J. Vertebrate embryo handedness. Nature. 1995 Apr;374(6524):681–681. doi:10.1038/374681a0

192. Dathe V, Gamel A, Männer J, Brand-Saberi B, Christ B. Morphological left-right asymmetry of Hensen's node precedes the asymmetric expression of Shh and Fgf8 in the chick embryo. Anatomy and Embryology. 2002 Oct 1;205(5–6):343–54. doi:10.1007/s00429-002-0269-2

193. Levin M, Johnson RL, Stern CD, Kuehn M, Tabin C. A molecular pathway determining left-right asymmetry in chick embryogenesis. Cell. 1995 Sep 8;82(5):803–14. doi:10.1016/0092-8674(95)90477-8

194. Boettger T, Wittler L, Kessel M. FGF8 functions in the specification of the right body side of the chick. Current Biology. 1999 Mar 11;9(5):277–80. doi:10.1016/S0960-9822(99)80119-5 PubMed PMID: 10074453.

195. Cui C, Little CD, Rongish BJ. Rotation of organizer tissue contributes to left-right asymmetry. Anat Rec (Hoboken). 2009 Apr;292(4):557–61. doi:10.1002/ar.20872 PubMed PMID: 19301278; PubMed Central PMCID: PMC2714534.

196. Levin M, Pagan S, Roberts DJ, Cooke J, Kuehn MR, Tabin CJ. Left/Right Patterning Signals and the Independent Regulation of Different Aspects of*Situs*in the Chick Embryo. Developmental Biology. 1997 Sep 1;189(1):57–67. doi:10.1006/dbio.1997.8662

197. Monsoro-Burq AH, Le Douarin N. Left-right asymmetry in BMP4 signalling pathway during chick gastrulation. Mechanisms of Development. 2000 Oct 1;97(1):105–8. doi:10.1016/S0925-4773(00)00417-2

198. Monsoro-Burq AH, Le Douarin NM. BMP4 Plays a Key Role in Left–Right Patterning in Chick Embryos by Maintaining Sonic Hedgehog Asymmetry. Molecular Cell. 2001 Apr 1;7(4):789–99. doi:10.1016/S1097-2765(01)00223-4

199. Pagán-Westphal SM, Tabin CJ. The Transfer of Left-Right Positional Information during Chick Embryogenesis. Cell. 1998 Apr 3;93(1):25–35. doi:10.1016/S0092-8674(00)81143-5

200. Negretti MI, Böse N, Petri N, Kremnyov S, Tsikolia N. Nodal asymmetry and hedgehog signaling during vertebrate left–right symmetry breaking. Front Cell Dev Biol. 2022 Sep 12;10:957211. doi:10.3389/fcell.2022.957211 PubMed PMID: 36172285; PubMed Central PMCID: PMC9511907.

201. Levin M, Thorlin T, Robinson KR, Nogi T, Mercola M. Asymmetries in H+/K+-ATPase and Cell Membrane Potentials Comprise a Very Early Step in Left-Right Patterning. Cell. 2002 Oct 4;111(1):77–89. doi:10.1016/S0092-8674(02)00939-X PubMed PMID: 12372302.

202. Raya Á, Kawakami Y, Rodríguez-Esteban C, Ibañes M, Rasskin-Gutman D, Rodríguez-León J, et al. Notch activity acts as a sensor for extracellular calcium during vertebrate left–right determination. Nature. 2004 Jan;427(6970):6970. doi:10.1038/nature02190

203. Raya Á, Kawakami Y, Rodríguez-Esteban C, Büscher D, Koth CM, Itoh T, et al. Notch activity induces Nodal expression and mediates the establishment of left–right asymmetry in vertebrate embryos. Genes Dev. 2003 May 15;17(10):1213–8. doi:10.1101/gad.1084403 PubMed PMID: 12730123; PubMed Central PMCID: PMC196060.

204. Asai R, Sinha S, Prakash VN, Mikawa T. Bilateral cellular flows display asymmetry prior to left–right organizer formation in amniote gastrulation. Proceedings of the National Academy of Sciences. 2025 Feb 11;122(6):e2414860122. doi:10.1073/pnas.2414860122

205. Meno C, Gritsman K, Ohishi S, Ohfuji Y, Heckscher E, Mochida K, et al. Mouse Lefty2 and Zebrafish Antivin Are Feedback Inhibitors of Nodal Signaling during Vertebrate Gastrulation. Molecular Cell. 1999 Sep 1;4(3):287–98. doi:10.1016/S1097-2765(00)80331-7 PubMed PMID: 10518210.

206. Esteban CR, Capdevila J, Economides AN, Pascual J, Ortiz Á, Belmonte JCI. The novel Cer-like protein Caronte mediates the establishment of embryonic left–right asymmetry. Nature. 1999 Sep;401(6750):6750. doi:10.1038/45738

207. Yokouchi Y, Vogan KJ, Pearse RV, Tabin CJ. Antagonistic Signaling by Caronte, a Novel Cerberus-Related Gene, Establishes Left–Right Asymmetric Gene Expression. Cell. 1999 Sep 3;98(5):573–83. doi:10.1016/S0092-8674(00)80045-8

208. Nakamura T, Hamada H. Left-right patterning: conserved and divergent mechanisms. Development. 2012 Sep 15;139(18):3257–62. doi:10.1242/dev.061606

209. Bell E, Muñoz-Sanjuán I, Altmann CR, Vonica A, Brivanlou AH. Cell fate specification and competence by Coco, a maternal BMP, TGFβand Wnt inhibitor. Development. 2003 Apr 1;130(7):1381–9. doi:10.1242/dev.00344

210. Vonica A, Brivanlou AH. The left–right axis is regulated by the interplay of Coco, Xnr1 and derrière in *Xenopus* embryos. Developmental Biology. 2007 Mar 1;303(1):281–94. doi:10.1016/j.ydbio.2006.09.039

211. Schweickert A, Vick P, Getwan M, Weber T, Schneider I, Eberhardt M, et al. The Nodal Inhibitor Coco Is a Critical Target of Leftward Flow in Xenopus. Current Biology. 2010 Apr 27;20(8):738–43. doi:10.1016/j.cub.2010.02.061 PubMed PMID: 20381352.

212. Hojo M, Takashima S, Kobayashi D, Sumeragi A, Shimada A, Tsukahara T, et al. Right-elevated expression of charon is regulated by fluid flow in medaka Kupffer's vesicle. Development, Growth & Differentiation. 2007;49(5):395–405. doi:10.1111/j.1440-169X.2007.00937.x

213. Blum M, Vick P. Left–Right Asymmetry: Cilia and Calcium Revisited. Current Biology. 2015 Mar 2;25(5):R205–7. doi:10.1016/j.cub.2015.01.031 PubMed PMID: 25734272.

214. Barnes RM, Black BL. Nodal Signaling and Congenital Heart Defects. In: Nakanishi T, Markwald RR, Baldwin HS, Keller BB, Srivastava D, Yamagishi H, editors. Etiology and Morphogenesis of Congenital Heart Disease: From Gene Function and Cellular Interaction to Morphology [Internet]. Tokyo: Springer; 2016 [cited 2026 Feb 22]. Available from: http://www.ncbi.nlm.nih.gov/books/NBK500272/ PubMed PMID: 29787126.

215. Logan M, Pagán-Westphal SM, Smith DM, Paganessi L, Tabin CJ. The Transcription Factor Pitx2 Mediates Situs-Specific Morphogenesis in Response to Left-Right Asymmetric Signals. Cell. 1998 Aug 7;94(3):307–17. doi:10.1016/S0092-8674(00)81474-9

216. Piedra ME, Icardo JM, Albajar M, Rodriguez-Rey JC, Ros MA. Pitx2 Participates in the Late Phase of the Pathway Controlling Left-Right Asymmetry. Cell. 1998 Aug 7;94(3):319–24. doi:10.1016/S0092-8674(00)81475-0 PubMed PMID: 9708734.

217. Ryan AK, Blumberg B, Rodriguez-Esteban C, Yonei-Tamura S, Tamura K, Tsukui T, et al. Pitx2 determines left–right asymmetry of internal organs in vertebrates. Nature. 1998 Aug;394(6693):6693. doi:10.1038/29004

218. Amand TRSt, Ra J, Zhang Y, Hu Y, Baber SI, Qiu M, et al. Cloning and Expression Pattern of Chicken*Pitx2:*A New Component in the SHH Signaling Pathway Controlling Embryonic Heart Looping. Biochemical and Biophysical Research Communications. 1998 Jun 9;247(1):100–5. doi:10.1006/bbrc.1998.8740

219. Yoshioka H, Meno C, Koshiba K, Sugihara M, Itoh H, Ishimaru Y, et al. Pitx2, a Bicoid-Type Homeobox Gene, Is Involved in a Lefty-Signaling Pathway in Determination of Left-Right Asymmetry. Cell. 1998 Aug 7;94(3):299–305. doi:10.1016/S0092-8674(00)81473-7

220. Bisgrove BW, Essner JJ, Yost HJ. Regulation of midline development by antagonism of lefty and nodal signaling. Development. 1999 Jul 15;126(14):3253–62. doi:10.1242/dev.126.14.3253

221. Cheng AMS, Thisse B, Thisse C, Wright CVE. The lefty-related factor Xatv acts as a feedback inhibitor of Nodal signaling in mesoderm induction and L-R axis development in Xenopus. Development. 2000 Mar 1;127(5):1049–61. doi:10.1242/dev.127.5.1049

222. Cheng SK, Olale F, Brivanlou AH, Schier AF. Lefty Blocks a Subset of TGFβ Signals by Antagonizing EGF-CFC Coreceptors. PLOS Biology. 2004 17;2(2):e30. doi:10.1371/journal.pbio.0020030

223. Meno C, Saijoh Y, Fujii H, Ikeda M, Yokoyama T, Yokoyama M, et al. Left-right asymmetric expression of the TGF beta-family member lefty in mouse embryos. Nature. 1996 May 9;381(6578):151–5. doi:10.1038/381151a0 PubMed PMID: 8610011.

224. Saijoh Y, Adachi H, Sakuma R, Yeo CY, Yashiro K, Watanabe M, et al. Left–Right Asymmetric Expression of *lefty2* and *nodal* Is Induced by a Signaling Pathway that Includes the Transcription Factor FAST2. Molecular Cell. 2000 Jan 1;5(1):35–47. doi:10.1016/S1097-2765(00)80401-3

225. Yamamoto M, Mine N, Mochida K, Sakai Y, Saijoh Y, Meno C, et al. Nodal signaling induces the midline barrier by activating Nodalexpression in the lateral plate. Development. 2003 May 1;130(9):1795–804. doi:10.1242/dev.00408

226. Meno C, Takeuchi J, Sakuma R, Koshiba-Takeuchi K, Ohishi S, Saijoh Y, et al. Diffusion of Nodal Signaling Activity in the Absence of the Feedback Inhibitor Lefty2. Developmental Cell. 2001 Jul 1;1(1):127–38. doi:10.1016/S1534-5807(01)00006-5 PubMed PMID: 11703930.

227. Müller P, Rogers KW, Jordan BM, Lee JS, Robson D, Ramanathan S, et al. Differential Diffusivity of Nodal and Lefty Underlies a Reaction-Diffusion Patterning System. Science. 2012 May 11;336(6082):721–4. doi:10.1126/science.1221920

228. Kuhn T, Landge AN, Mörsdorf D, Coßmann J, Gerstenecker J, Čapek D, et al. Single-molecule tracking of Nodal and Lefty in live zebrafish embryos supports hindered diffusion model. Nat Commun. 2022 Oct 15;13(1):6101. doi:10.1038/s41467-022-33704-z

229. Juan H, Hamada H. Roles of nodal-lefty regulatory loops in embryonic patterning of vertebrates. Genes to Cells. 2001;6(11):923–30. doi:10.1046/j.1365-2443.2001.00481.x

230. Ishimaru Y, Yoshioka H, Tao H, Thisse B, Thisse C, V.E. Wright C, et al. Asymmetric expression of *antivin/lefty1* in the early chick embryo. Mechanisms of Development. 2000 Jan 1;90(1):115–8. doi:10.1016/S0925-4773(99)00232-4

231. Meno C, Shimono A, Saijoh Y, Yashiro K, Mochida K, Ohishi S, et al. lefty-1 Is Required for Left-Right Determination as a Regulator of lefty-2 and nodal. Cell. 1998 Aug 7;94(3):287–97. doi:10.1016/S0092-8674(00)81472-5

232. Kurpios NA, Ibañes M, Davis NM, Lui W, Katz T, Martin JF, et al. The direction of gut looping is established by changes in the extracellular matrix and in cell:cell adhesion. Proceedings of the National Academy of Sciences. 2008 Jun 24;105(25):8499–506. doi:10.1073/pnas.0803578105

233. Davis NM, Kurpios NA, Sun X, Gros J, Martin JF, Tabin CJ. The Chirality of Gut Rotation Derives from Left-Right Asymmetric Changes in the Architecture of the Dorsal Mesentery. Developmental Cell. 2008 Jul 8;15(1):134–45. doi:10.1016/j.devcel.2008.05.001 PubMed PMID: 18606147.

234. Sanketi BD, Zuela-Sopilniak N, Bundschuh E, Gopal S, Hu S, Long J, et al. Pitx2 patterns an accelerator-brake mechanical feedback through latent TGFβ to rotate the gut. Science. 2022 Sep 23;377(6613):eabl3921. doi:10.1126/science.abl3921

235. Sivakumar A, Mahadevan A, Lauer ME, Narvaez RJ, Ramesh S, Demler CM, et al. Midgut Laterality Is Driven by Hyaluronan on the Right. Developmental Cell. 2018 Sep 10;46(5):533-551.e5. doi:10.1016/j.devcel.2018.08.002 PubMed PMID: 30174180.

236. Welsh IC, Thomsen M, Gludish DW, Alfonso-Parra C, Bai Y, Martin JF, et al. Integration of Left-Right Pitx2 Transcription and Wnt Signaling Drives Asymmetric Gut Morphogenesis via Daam2. Developmental Cell. 2013 Sep 30;26(6):629–44. doi:10.1016/j.devcel.2013.07.019 PubMed PMID: 24091014.

237. Rida PCG, Le Minh N, Jiang YJ. A Notch feeling of somite segmentation and beyond. Developmental Biology. 2004 Jan 1;265(1):2–22. doi:10.1016/j.ydbio.2003.07.003

238. Oates AC, Morelli LG, Ares S. Patterning embryos with oscillations: structure, function and dynamics of the vertebrate segmentation clock. Development. 2012 Feb 15;139(4):625–39. doi:10.1242/dev.063735 PubMed PMID: 22274695.

239. Stickney HL, Barresi MJF, Devoto SH. Somite development in zebrafish. Developmental Dynamics. 2000;219(3):287–303. doi:10.1002/1097-0177(2000)9999:9999<::AID-DVDY1065>3.0.CO;2-A

240. Tam PPL, Trainor PA. Specification and segmentation of the paraxial mesoderm. Anat Embryol. 1994 Apr 1;189(4):275–305. doi:10.1007/BF00190586

241. Bellairs R. The segmentation of somites in the chick embryo. Bollettino di zoologia. 1980 Jan 1;47(3–4):245–52. doi:10.1080/11250008009438682

242. Naganathan SR, Popović M, Oates AC. Left–right symmetry of zebrafish embryos requires somite surface tension. Nature. 2022 May;605(7910):516–21. doi:10.1038/s41586-022-04646-9

243. Graham JH, Raz S, Hel-Or H, Nevo E. Fluctuating Asymmetry: Methods, Theory, and Applications. Symmetry. 2010 Jun;2(2):2. doi:10.3390/sym2020466

244. Vermot J, Llamas JG, Fraulob V, Niederreither K, Chambon P, Dollé P. Retinoic Acid Controls the Bilateral Symmetry of Somite Formation in the Mouse Embryo. Science. 2005 Apr 22;308(5721):563–6. doi:10.1126/science.1108363

245. Vermot J, Pourquié O. Retinoic acid coordinates somitogenesis and left–right patterning in vertebrate embryos. Nature. 2005 May;435(7039):7039. doi:10.1038/nature03488

246. Kawakami Y, Raya Á, Raya RM, Rodríguez-Esteban C, Belmonte JCI. Retinoic acid signalling links left–right asymmetric patterning and bilaterally symmetric somitogenesis in the zebrafish embryo. Nature. 2005 May;435(7039):7039. doi:10.1038/nature03512

247. Vilhais-Neto GC, Maruhashi M, Smith KT, Vasseur-Cognet M, Peterson AS, Workman JL, et al. Rere controls retinoic acid signalling and somite bilateral symmetry. Nature. 2010 Feb;463(7283):953–7. doi:10.1038/nature08763

248. Brend T, Holley SA. Balancing segmentation and laterality during vertebrate development. Seminars in Cell & Developmental Biology. 2009 Jun 1;The Molecular and Cellular Mechanisms in the Development of Addiction20(4):472–8. doi:10.1016/j.semcdb.2008.11.009

249. Brueckner M, D'Eustachio P, Horwich AL. Linkage mapping of a mouse gene, iv, that controls left-right asymmetry of the heart and viscera. Proceedings of the National Academy of Sciences. 1989 Jul;86(13):5035–8. doi:10.1073/pnas.86.13.5035

250. Jouve C, Iimura T, Pourquie O. Onset of the segmentation clock in the chick embryo: evidence for oscillations in the somite precursors in the primitive streak. Development. 2002 Mar 1;129(5):1107–17. doi:10.1242/dev.129.5.1107

251. Brink RC, Schlösser TPC, Colo D, Vincken KL, van Stralen M, Hui SCN, et al. Asymmetry of the Vertebral Body and Pedicles in the True Transverse Plane in Adolescent Idiopathic Scoliosis: A CT-Based Study. Spine Deform. 2017 Jan 1;5(1):37–45. doi:10.1016/j.jspd.2016.08.006

252. Sevastik B, Xiong B, Sevastik J, Hedlund R, Suliman I. Vertebral rotation and pedicle length asymmetry in the normal adult spine. Eur Spine J. 1995 Apr 1;4(2):95–7. doi:10.1007/BF00278919

253. Schlösser TPC, Semple T, Carr SB, Padley S, Loebinger MR, Hogg C, et al. Scoliosis convexity and organ anatomy are related. Eur Spine J. 2017 Jun 1;26(6):1595–9. doi:10.1007/s00586-017-4970-5

254. Zhu F, Chu WC wing, Sun G, Zhu Z zhang, Wang W jun, Cheng JCY, et al. Rib length asymmetry in thoracic adolescent idiopathic scoliosis: is it primary or secondary? Eur Spine J. 2011 Feb 1;20(2):254–9. doi:10.1007/s00586-010-1637-x

255. Abbott EN, Reddy AP, Coleman A, Brandt MV, Sandler KL, Maxwell PG, et al. Quantification of Chest Wall Asymmetry in Healthy Females Using Standardized Computed Tomography–Derived Curve Modeling: A Proof of Concept. Aesthet Surg J Open Forum. 2025 Jan 1;7:ojaf116. doi:10.1093/asjof/ojaf116

256. González-Ruiz JM, Pérez-Núñez MI, García-Alfaro MD, Bastir M. Geometric morphometrics of adolescent idiopathic scoliosis: a prospective observational study. Eur Spine J. 2021 Mar 1;30(3):612–9. doi:10.1007/s00586-020-06583-5

257. Taylor JR. Scoliosis and Growth: Patterns of Asymmetry in Normal Vertebral Growth. Acta Orthopaedica Scandinavica. 1983 Jan 1;54(4):596–602. doi:10.3109/17453678308992896 PubMed PMID: 6422693.

258. Plochocki JH. Directional bilateral asymmetry in human sacral morphology. International Journal of Osteoarchaeology. 2002;12(5):349–55. doi:10.1002/oa.633

259. Ren BO, Dumaine AM, Du JY, Hedequist DJ, Glotzbecker MP, Harms Study Group. Left-sided thoracic curves in adolescent idiopathic scoliosis: are the outcomes different? Spine Deform. 2025 Jul 1;13(4):1067–74. doi:10.1007/s43390-025-01069-0

260. Rinsky LA, Gamble JG. Adolescent Idiopathic Scoliosis. West J Med. 1988 Feb;148(2):182–91. PubMed PMID: 3279708; PubMed Central PMCID: PMC1026057.

Chapter 2

Somite Asymmetry and its Regulation in the Early Chick Embryo

Author contributions: Jong Gwan Lee and Olivier Pourquié conceptualized the study. Jong Gwan Lee performed the experiments and analyzed the data. Andrew Silberfeld assisted in the somite volume asymmetry analysis. Jong Gwan Lee and Olivier Pourquié wrote the manuscript. Olivier Pourquié supervised the project.

INTRODUCTION

Bilateral symmetry is one of the fundamental features of most metazoans and defines the Bilateria clade. In vertebrates, this bilateral symmetry is largely conferred by the musculoskeletal system, in contrast to the asymmetry of visceral organs such as the lungs, heart, and spleen. In human health, the proper regulation of both symmetry and asymmetry in the body is critical. For instance, loss of bilateral symmetry in the vertebral column leads to scoliosis. Conversely, while patients with complete inversion of organ situs (situs inversus totalis) generally do not display major health issues, those with partial inversion of situs (heterotaxy) often suffer from a range of medical complications due to impaired coordination across organs and reduced life expectancy (1,2). However, the etiology of many laterality-related diseases remains poorly understood.

Somites are embryonic precursors of most of the vertebrate musculoskeletal system, including the vertebrae and skeletal muscles. Somites have long fascinated biologists because of their sequential and rhythmic formation. For instance, every 1.5 hr in the chick embryo and every 5 hr in the human embryo, a new pair of somites buds off from the anterior tip of the unsegmented, mesenchymal paraxial mesoderm, called the presomitic mesoderm (PSM) (3,4). The complex interplay among signaling pathways and transcription factors underlying this striking rhythmicity has long been an active area of research. Another feature of somites that is widely noted but rather poorly understood is their bilateral symmetry. Somites have long been considered one of the earliest hallmarks of bilateral symmetry, as they emerge as bilateral columns of epithelial spheres flanking the midline.

Recent studies of somite bilateral symmetry have challenged the view that bilateral symmetry is the default state, instead suggesting that somitogenesis occurs in the context of multiple sources of asymmetry. For instance, in zebrafish, nascent somites display fluctuating

asymmetry—an asymmetry without consistent directionality—in anteroposterior (AP) position and length, which gradually converges toward symmetry through shape adjustment (5). Furthermore, studies in multiple vertebrate model organisms have demonstrated that the retinoic acid (RA) pathway is crucial for ensuring bilateral symmetry of somitogenesis, functioning as a buffer against the Left-Right (LR) determination pathway (6–8). When RA signaling is perturbed, LR coordination of gene expression underlying somite patterning is disrupted, leading to directional defects in somitogenesis. Together, these findings suggest that bilateral symmetry of somites is actively achieved through multiple regulatory mechanisms.

Traditionally, symmetry in somites has been evaluated qualitatively as a binary feature, and such approaches naturally limit research to the few perturbation conditions in which somite bilateral symmetry is visibly compromised. Consequently, bilateral symmetry under wildtype conditions has not been thoroughly investigated, and the extent to which somites are symmetric remains unclear. Without a proper characterization of somite bilateral symmetry under wildtype conditions, it is difficult to accurately assess the effects of factors that either compromise or promote bilateral symmetry.

The current work presents a systematic and quantitative characterization of somite bilateral symmetry in the wildtype chick embryo, identifying a novel directional asymmetry both in the morphology of anterior somites and in the gene expression patterns underlying somitogenesis. This novel directional asymmetry is driven by signals involved in LR determination. Using both the chick embryo and a human iPSC in vitro model, we show that Nodal signaling, a member of the TGF-β superfamily, accelerates the dynamics of somitogenesis. We recapitulated the interaction between Nodal and RA signaling pathways in vitro to demonstrate that NODAL accelerates somitogenesis only under RA inhibition. Thus, our results

not only provide a foundation for the study of bilateral symmetry in wildtype somites but also establish a mechanistic link between LR determination and RA signaling pathways in the context of somitogenesis.

RESULTS

Morphological asymmetry of somites

To quantify somite bilateral symmetry, we first compared the volume of bilateral somite pairs. Chick embryos at HH8-9 were stained with hybridization chain reaction (HCR) RNA-FISH using the somite marker *MEOX1* mRNA to visualize and segment the somites (9). We next compared the volume of each somite from contralateral pairs (**Fig.2.1A**). This analysis uncovered a novel directional asymmetry, in which the left anterior somites are larger than the right ones (**Fig.2.1B**). For instance, the 2nd somite (counting from the most anterior, first-formed somite to indicate the rostral-to-caudal axial level) on the left side was on average 17% larger than the contralateral somite on the right side ($\text{Log}(L/R) = 0.06987$; $L/R \sim 1.175$).

Next, using chick embryos at the 5-13 somite stage (Hamburger Hamilton (HH) stage 8-10), we compared the AP position of left and right somites to evaluate asymmetry in somite alignment (**Fig.2.1.C**). Somite posterior boundaries were identified by marking the two endpoints of each boundary and determining its midpoint. These midpoints were then projected onto an abstracted midline manually drawn along the dorsal midline of the neural tube, and the relative AP positions of contralateral pairs were compared. Embryos with less than 5 somites were not included because they often did not exhibit a clear dorsal midline due to the wide opening of the neural tube. The analysis revealed another previously unrecognized directional asymmetry, in which the left anterior somites are more anteriorly positioned than their right

counterparts (**Fig.2.1.D**). For instance, the left 5th and 6th somites were on average more anteriorly positioned than their right counterparts by 14μm. Notably, this leftward bias increased progressively from the first to the fifth somite before declining, raising the possibility that somite AP position asymmetry is progressively amplified at the level of the occipital somites during successive rounds of somitogenesis (an "augmenting phase"). Wildtype embryos imaged in culture in vitro and GFP embryos imaged in ovo showed a nearly identical trend, indicating that this directional asymmetry is not strain-dependent nor an artifact of the culture conditions (**Fig.2.1.D'**) (10). Binning embryos by somite stage revealed that the left bias is most pronounced at early stages. The left bias in AP position of both formed and nascent somites gradually resolves toward symmetry over development (**Fig.2.1.D"**).

Figure 2.1. Morphological asymmetry of the anterior somites

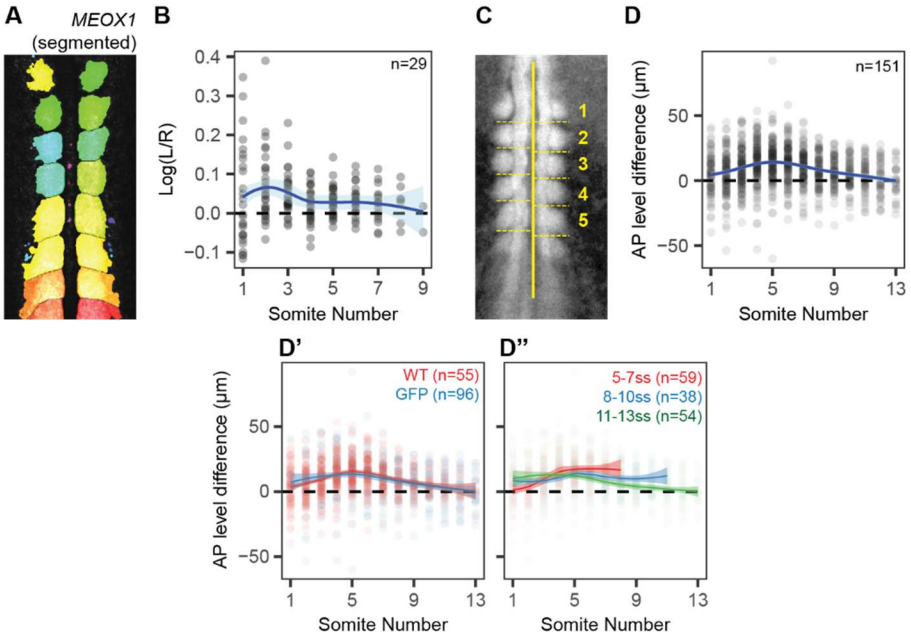

Figure 2.1. (A) A 7-somite stage chick embryo labeled with HCR RNA-FISH for the somite marker *MEOX1*. Automatic segmentation based on the thresholded *MEOX1* signal was used to calculate the volume of individual somites. (B) Left anterior somites are larger than the right ones in early chick embryos (5- to 9-somite stage). As the plot represents Log(L/R), a positive value means that the left somites are larger. The left bias in volume is most pronounced in the 2nd somite and decreases in more posterior somites. (C) Measurement of somite AP boundary position asymmetry. (D) Left anterior somites are more anteriorly positioned than the right ones. A positive value means that the left somite boundary is more anterior. The analysis of early chick embryos (5- to 13-somite stage) displays a trend where the left bias increases from the 1st to the 5th somite. (D') Such asymmetry is nearly identical between wildtype and GFP embryos. (D'') Somite AP position asymmetry is most pronounced in early-stage embryos (5-to-7-somite stage) and decreases later.

Gene expression asymmetry underlying somitogenesis

To understand the origin of this somite asymmetry, we analyzed asymmetry in gene expression underlying somitogenesis. Traditionally, somite formation is described with the "clock and wavefront model" positing the interaction between the oscillatory phases of PSM cells ("clock") and the slowly regressing front of maturation ("wavefront"), which triggers somite formation (11). LR desynchronization of these components can be translated into misalignment of somite positions. To determine the asymmetry in "wavefront" positioning, we compared the mRNA expression patterns of the posterior PSM markers *MSGN1* and *FGF8* on the left and right sides using HCR RNA-FISH (**Fig.2.2.A,C**) (12,13). For these genes, we drew ROIs parallel to the midline along the PSM to quantify left and right gene expression gradients. The analysis revealed that the expression patterns of these genes were more extended anteriorly on the left side during the 1- to 5-somite stage. This suggests an asymmetric expansion of the posterior PSM identity (**Fig.2.2.B,D**). The left bias in *MSGN1* expression resolves over development. At the 11+ somite stage, the *MSGN1* gradient is nearly symmetric (**Fig.2.2.D,K,L**).

The cyclic genes regulated by the segmentation clock are expressed as periodic traveling waves sweeping across the unsegmented PSM (3). The waves are first expressed in a broad posterior domain of the PSM, and they progressively narrow while traveling anteriorly. Loss of coordination between LR traveling waves can manifest as differences in AP position and/or length of the expression domain, which together indicate differences in oscillation phase (**Fig.2.2.E**). Analysis of the cyclic gene lunatic fringe (*LFNG*) during the 1- to 5-somite stage revealed a directional asymmetry (14,15): the left *LFNG* traveling waves are more anteriorly positioned, and the AP length of their domain is smaller than the right ones (**Fig.2.2.F-H**). This analysis suggests that the segmentation clock phase is more advanced on the left side. These

asymmetries persist until the 5- to 6-somite stage and progressively resolve later, such that the traveling wave is symmetric after the 11-somite stage (**Fig.2.2.F,G,K,L**). Analysis of the segmentation gene *MESP2* (16), which appears as stripes at the level of determination front, also showed a similar asymmetric pattern (**Fig.2.2.I-L**). In short, occipital somites demonstrate robust and extensive asymmetries in both their morphology and the gene expression patterns underlying their formation.

Figure 2.2. Gene expression patterns underlying somitogenesis show corresponding asymmetry

Figure 2.2. (A) Measurement of *MSGN1* asymmetry. Parallel ROIs along the left and right PSM were drawn to identify the AP position at which the left and right *MSGN1* signals reach a common, normalized threshold. (B) *MSGN1* is more anteriorly extended on the left side during the augmenting phase (1- to 5-somite stage), whereas this asymmetry is resolved to symmetric *MSGN1* expression at later stages (11+ somite stage). A positive value means that left *MSGN1* is more anteriorly extended. The right panel shows *MSGN1* asymmetry from the 1- to 13-somite stage. (C) Measurement of *FGF8* asymmetry. The same approach as for *MSGN1* was applied. (D) *FGF8* in the PSM extends more anteriorly on the left side during the augmenting phase. (E) Measurement of *LFNG* asymmetry. AP levels over which *LFNG* signals exceed a common, normalized threshold represent the *LFNG* expression domain. Midpoints and the AP length of left and right *LFNG* domains were extracted to analyze *LFNG* asymmetry. (F) Left *LFNG* traveling waves are more anteriorly positioned than the right ones in early stages. A positive value means that left *LFNG* is more anteriorly positioned than the right one. This early left bias is maintained throughout the augmenting phase and decreases later. (G) Left *LFNG* traveling waves are shorter than the right ones in early stages. A negative value means that the left *LFNG* traveling wave is shorter than the right one. Similarly, the asymmetry in the length of *LFNG* traveling waves decreases later. (H) Left-advanced *LFNG* traveling waves in wildtype HH7-8 chick embryos. (I) Measurement of *MESP2* asymmetry. The peaks of *MESP2* signal represent the AP position of the *MESP2* expression domain. (J) *MESP2* expression shows similar left bias in AP position. A positive value means that left *MESP2* is more anteriorly positioned. (K) HCR RNA-FISH of *LFNG*, *MSGN1* and *MESP2* at an early stage demonstrates striking asymmetry, compared to the later stage (L). Statistics are unpaired two-sided t-test. * is $p < 0.05$; ** is $p < 0.01$. Scale bar = 100μm

Figure 2.2. (continued)

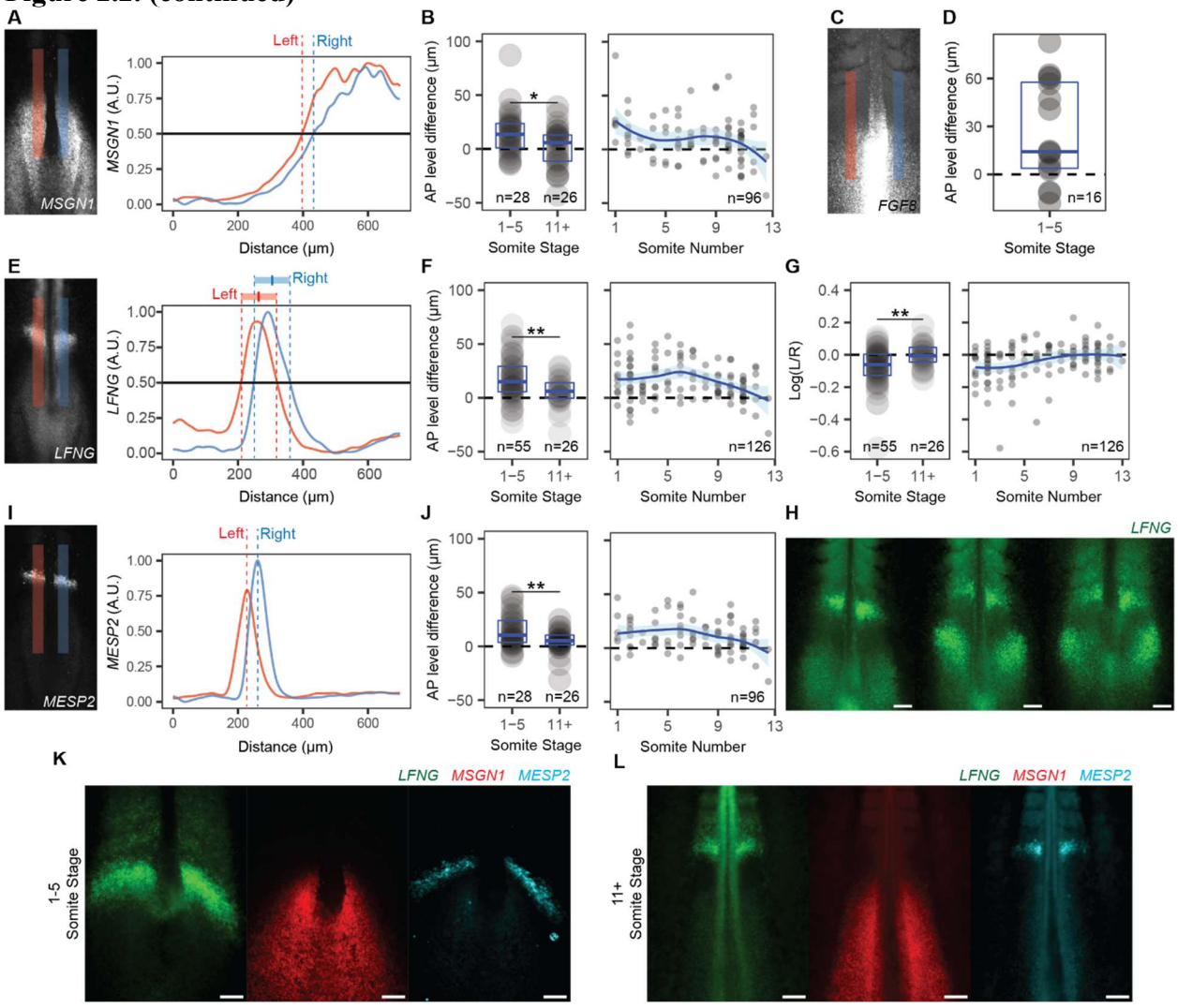

LR determining signals cause somite asymmetry

During the earliest rounds of segmentation clock gene oscillations specifying occipital somites, Sonic hedgehog (SHH) is asymmetrically expressed on the left side of the HN (HH4-5) and activates NODAL (HH5-6), a conserved determinant of the vertebrate left side (17). Soon, NODAL is transferred to and transiently amplified in the LPM to activate a downstream signaling cascade that confers left identity. In early somite stages, the posterior PSM is exposed to the asymmetric signals emanating from the HN (**Fig.2.3.A**). Therefore, to explain the directional asymmetry in somitogenesis, we hypothesized that signaling factors involved in the LR determination pathway asymmetrically affect gene expression underlying somite formation. To test this hypothesis, we applied various treatments that perturb LR determination (**Fig.2.3.B**). For instance, we placed a bead soaked in SAG on the right side of the HN at HH4 to induce ectopic NODAL expression on the right side of the embryo. Conversely, to preempt the activation of NODAL on either side, we treated embryos at HH4 with the SHH inhibitor cyclopamine. In addition, we also used beads soaked in human recombinant NODAL protein placed along the right paraxial mesoderm to induce ectopic NODAL expression on the right side of the embryo. The success of these treatments was assessed by the *NODAL* expression pattern. All these treatments were highly effective in eliciting the expected outcomes. For instance, in a pool of embryos treated with SAG beads (200-500μM), cyclopamine (100uM), or NODAL beads (50μg/ml), the *NODAL* expression pattern was altered as predicted in 50/65 (77%), 51/51 (100%), and 39/48 (81%) of embryos, respectively.

To test the role of LR patterning signals on the morphological asymmetry of occipital somites, we analyzed somite volume asymmetry upon cyclopamine treatment. We observed a decrease in volume asymmetry at the occipital level, most significantly for the 2nd somite

(**Fig.2.3.C**). Similarly, we measured somite AP position asymmetry after perturbing of LR determination with cyclopamine, SAG bead, and NODAL bead treatments. All these treatments modified the left bias in somite AP position, with somites becoming almost symmetric or even right biased. **(Fig.2.3.D)**

To test whether the modulation of somite asymmetry is mediated by the effect of LR determining signals on the patterning process, we evaluated the asymmetry of gene expression underlying somitogenesis **(Fig.2.3.E,H)**. The asymmetry analysis of the cyclic gene *LFNG* displayed significant shifts toward symmetry in both the AP position and the length of the expression stripes (**Fig.2.3.F,G**). On the other hand, the left bias in the expression pattern of the posterior PSM marker *MSGN1* was not affected by SAG bead treatment on the right side of the HN. This suggests that posterior PSM identity is likely not the target of modulation by LR patterning signals (**Fig.2.3.I**). Altogether, these results suggest that LR determining signals primarily act on the dynamic expression of cyclic genes to generate somite asymmetry in the wildtype chick embryo.

Figure 2.3. Asymmetries in somites and gene expression patterns are modulated by LR determining signals

Figure 2.3. (A) During the early somite stages (HH7), *NODAL* is expressed in the anterior PSM adjacent to the HN and in the left LPM. Early somitogenesis spatially and temporally overlaps with LR determination. (B) Treatments perturbing LR determination. The success of each treatment is determined by the *NODAL* expression. (C) Cyclopamine treatment decreases the volume asymmetry of the 2nd somite. (D) Somite AP position asymmetry is modulated by cyclopamine, SAG bead, and NODAL bead treatments. Upon these treatments, anterior somites become either near symmetric or even right biased. The right panel shows the shift toward symmetry of the 4th, 5th, and 6th somite upon these treatments. (E) *LFNG* traveling waves in the augmenting phase upon NODAL and SAG bead treatment. (F) AP position asymmetry and (G) length asymmetry of *LFNG* traveling waves are altered upon treatments perturbing LR determination. (H) *MSGN1* expression upon SAG bead treatment. (I) *MSGN1* asymmetry in the augmenting phase is not affected by SAG bead treatment. Statistics are unpaired two-sided t-test. * is $p < 0.05$; ** is $p < 0.01$; *** is $p < 0.001$. Scale bar = 100μm

Figure 2.3. (continued)

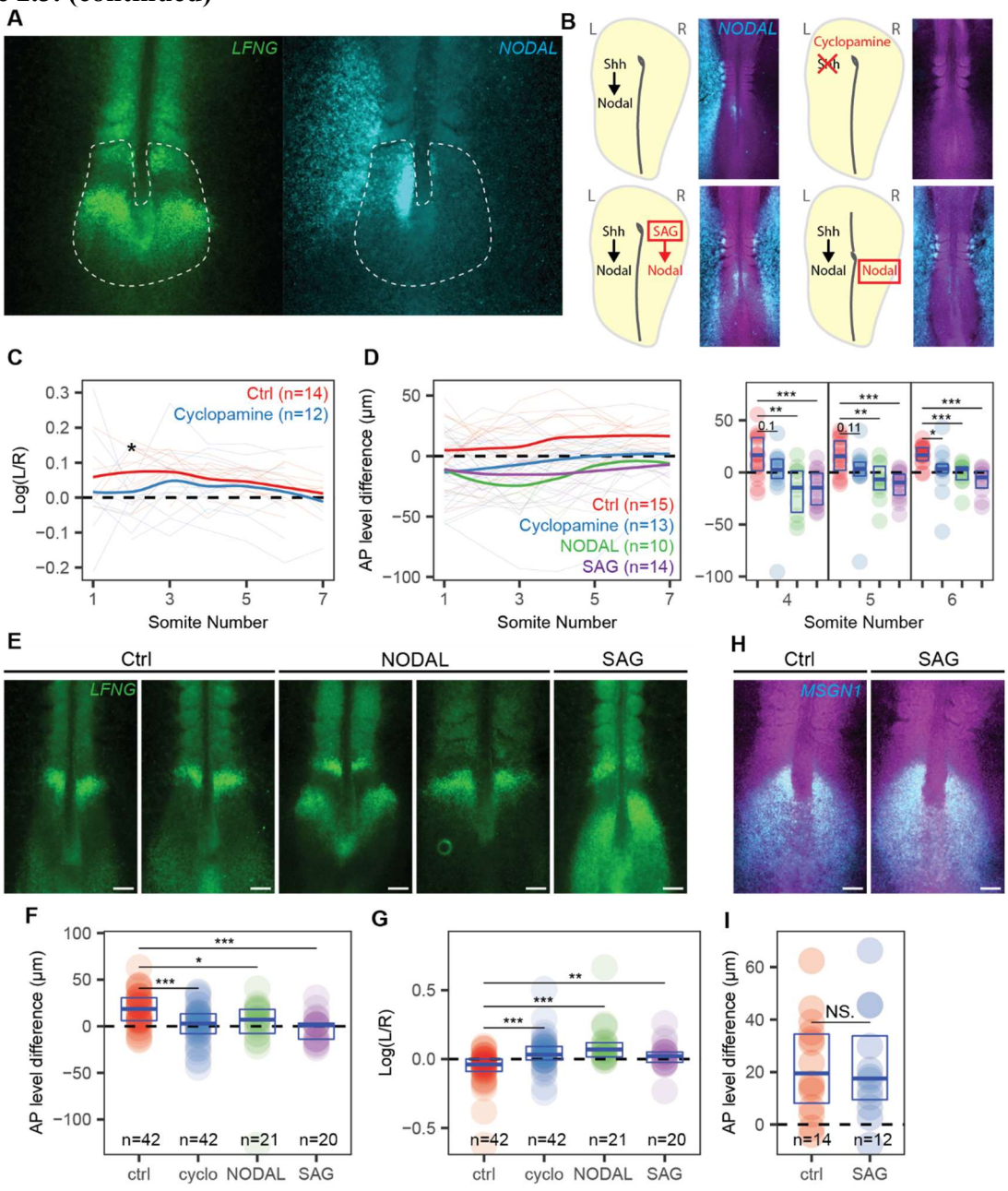

NODAL accelerates clock gene oscillation under RA inhibition

Our observations and experiments in the chick embryo uncovered a novel directional asymmetry of somite and identified LR determining signals as the underlying cause. However, precisely dissecting how the oscillation is affected by LR determining signals is difficult in chick embryos due to the lack of tools to analyze segmentation clock oscillation in real time. To address this limitation, we took advantage of a human iPSC fluorescent reporter line, which can be differentiated into posterior-PSM-like cells to image cyclic gene oscillations in vitro (**Fig.2.4.A**) (4). In these experiments, human iPSCs were cultured for 2 days in DMEM/F12 supplemented with a WNT agonist (Chir) and a BMP inhibitor (LDN) for 2 days and replated into an ibidi 24-well imaging plate at 500k/well in the so-called "clock medium" containing a WNT agonist (Chir), a BMP inhibitor (LDN), FGF4 protein, ROCK inhibitor (Y-27632), and the RA inverse agonist (BMS493). Using a human cell line with a segmentation clock reporter (HES7-Achilles), the oscillation of HES7 can be observed for over 2 days.

To test the effect of NODAL on oscillation dynamics, we added human recombinant NODAL protein to the clock medium and assessed oscillation dynamics. Interestingly, addition of NODAL to a final concentration of 0.2μg/ml (B+N+) and 0.5μg/ml (B+N++) to the regular clock medium (B+) decreased the oscillation period of HES7 up to 4.6% and 5.6%, respectively (B+:4.679hr; B+N+:4.463hr; B+N++: 4.417hr) (**Fig.2.4.B,B'**). This suggests that NODAL can accelerate the oscillations of the cyclic genes on the left side, resulting in the left traveling waves of the cyclic genes to appear more advanced on the left than on the right side. Thus, our data demonstrate that NODAL can accelerate clock gene oscillations in vitro.

Previous experiments demonstrated that the LR determination pathway can interact with somitogenesis and generate lateralized somite asymmetry when RA signaling is inhibited (6–8).

For instance, in mouse and zebrafish mutants for the RA biosynthetic enzyme RALDH2, somitogenesis is advanced on the left side, compared to the right side. However, the precise role of RA in buffering against an asymmetric signaling environment has remained elusive. In our experiments, the RA inverse agonist BMS493, which inhibits RA signaling, was included as it is a component of the "clock medium", which enhances segmentation clock oscillations (4). Removal of BMS493 from the clock medium led to an ~1.7-fold increase in RA target *RARB* mRNA expression and did not affect the maintenance of HES7-Achilles oscillations (**Fig.2.4.C,E,F**). Surprisingly, we observed that when RA signaling was not inhibited by BMS493, NODAL failed to accelerate the clock (**Fig.2.4.D**). When the detrended mean HES7-Achilles oscillation traces were compared, NODAL addition under RA inhibition caused clear divergence between conditions (B+ vs. B+N+) (**Fig.2.4.E,F**). In contrast, when the RA pathway was left unperturbed, the average oscillation traces with and without NODAL remained closely aligned, showing little phase divergence between conditions (B- vs. B-N+) (**Fig.2.4.E',F'**).

Figure 2.4. Segmentation clock gene oscillation is accelerated by NODAL under RA inhibition

Figure 2.4. (A) Protocol to differentiate human iPSCs into a posterior-PSM-like state. At 48hr, cells are replated with clock medium including NODAL and/or BMS493. (B) Addition of human recombinant NODAL protein (N+: 0.2μg/ml; N++: 0.5μg/ml) to the clock medium (B+: BMS493 2.5μM) accelerates HES7-Achilles oscillations. The right panel represents the same data normalized to the average period of B+. (C) Removal of BMS493 from the clock medium significantly increases *RARB* mRNA expression determined by qPCR after 24hr in clock medium. n=6 for each condition. (D) NODAL (N+: 0.2μg/ml) accelerates HES7 oscillations under RA inhibition by BMS493 (B+: 2.5μM). Without RA inhibition, NODAL does not accelerate the clock. The right panel represents the same data normalized to the average period of B+. (E,F) Detrended mean HES7-Achilles oscillation traces from representative individual sets of experiments show that under RA inhibition NODAL treatment accelerates HES7 oscillations (B+ vs. B+N+). (E',F') By contrast, without RA inhibition, oscillations remain closely aligned regardless of the addition of NODAL (B- vs. B-N+). Statistics are unpaired two-sided t-test. * is $p < 0.05$; ** is $p < 0.01$; *** is $p < 0.001$.

Figure 2.4. (continued)

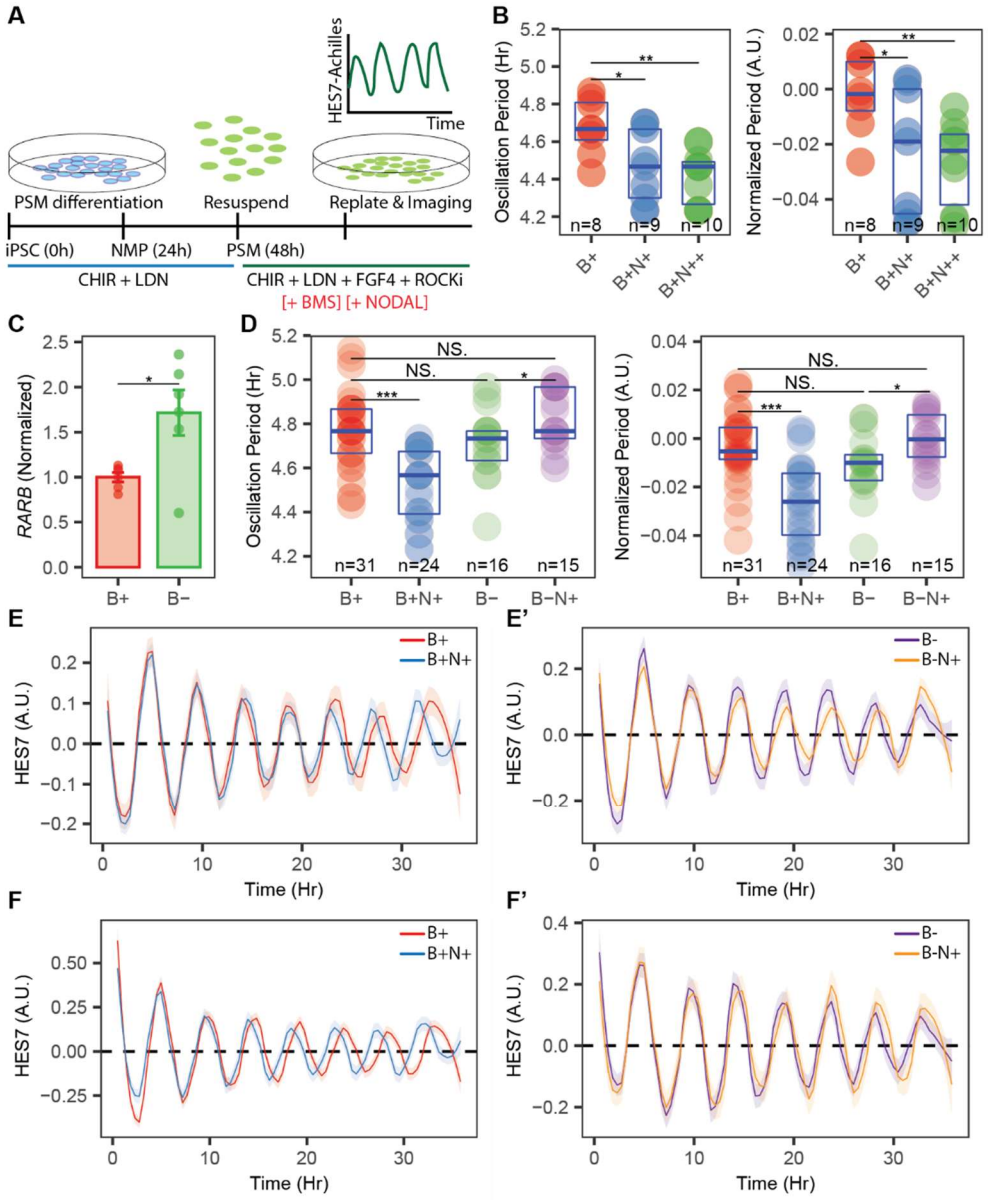

qPCR analysis of *NODAL* expression in NODAL-treated culture conditions revealed strong upregulation under RA inhibition by BMS493 (B+N+) at 12hr after treatment (**Fig.2.5.A**). At 24hr after treatment, *NODAL* expression was significantly upregulated in all three conditions (B+N+, B-, and B-N+) compared to the base clock medium (B+), with the highest expression in the B-N+ condition (**Fig.2.5.A'**). The *NODAL* gene locus contains a highly conserved retinoic acid response element and is regulated by both activation and inhibition of the RA pathway (18–23). This result indicates that RA might modulate the response kinetics of NODAL signaling. In addition, the gene expression levels of posterior PSM markers at 24hr— *MSGN1*, *TBX6*, *FGF8*, and *DUSP6*—were mostly unaffected by the treatments (**Fig.2.5.B-E**). These results suggest that the various conditions likely did not affect the cells' posterior PSM identity. In summary, the experiments with in vitro system allowed us to determine that NODAL accelerates clock gene oscillations and to model signaling interactions in the developing paraxial mesoderm. Together, our in vitro experiments suggest that RA maintains LR symmetry in somitogenesis, at least in part, by buffering the NODAL-mediated acceleration of clock gene oscillations.

Figure 2.5. qPCR analysis of the in vitro human cell model with BMS493 and/or NODAL

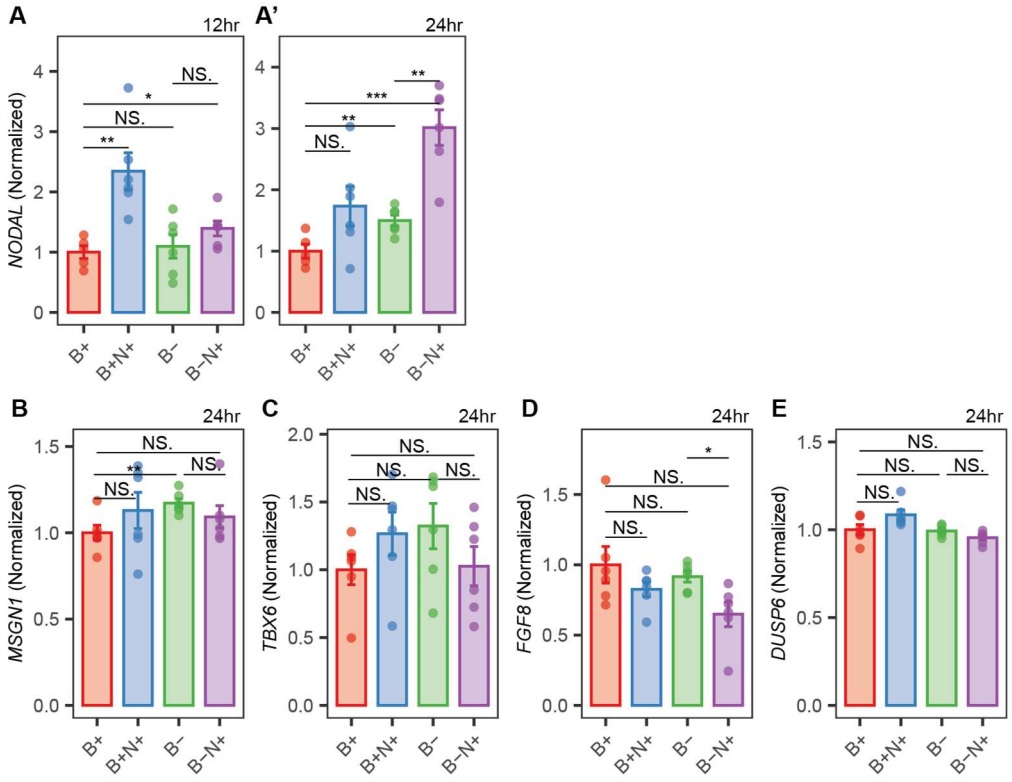

Figure 2.5. (A) *NODAL* mRNA level after 12hr in clock medium shows the most dramatic upregulation of *NODAL* mRNA in the B+N+ condition (BMS493 2.5µM; human recombinant NODAL 0.2µg/ml). *NODAL* mRNA is also significantly upregulated in the B-N+ condition (human recombinant NODAL 0.2µg/ml). n=6 for B+N+, B-, and B-N+; n=5 for B+. (A') *NODAL* mRNA expression at 24hr is most sharply upregulated in the B-N+ condition. n=6 for B+N+, B-, and B-N+; n=5 for B+. (B-E) mRNA level of the posterior PSM markers *MSGN1*, *TBX6*, *FGF8*, and *DUSP6* at 24hr. Statistics are unpaired two-sided t-test. * is $p < 0.05$; ** is $p < 0.01$; *** is $p < 0.001$.

RA treatment makes *LFNG* traveling wave symmetric

We next decided to revisit the role of the RA signaling pathway in somite bilateral symmetry in the chick embryo. The pharmacological inhibition of RA production with disulfiram, an inhibitor of the RA synthesis enzyme RALDH2, has been shown to produce asymmetry in somite boundary position (7). In these experiments, somite boundaries on the left side at the cervical level were located more anteriorly than those on the right side. This phenotype has been traditionally interpreted as acceleration of somitogenesis on the right side,

which is opposite to the somitogenesis acceleration on the left side observed in mouse and zebrafish embryos (6,8).

To revisit the role of the RA pathway in the control of somite bilateral symmetry in chicken embryos, we used the RA inverse agonist BMS493 (100µM) and the RALDH2 inhibitor DEAB (100µM). We first confirmed that these treatments could significantly decrease the expression of *RARB* mRNA in vivo, indicating that they effectively decrease RA signaling (**Fig.2.6.A**). Unexpectedly, when examined in 5- to 9-somite embryos, RA signaling inhibition with these drugs led to a smaller magnitude of left bias in somite AP position asymmetry (**Fig.2.6.B**). Consistently, *LFNG* traveling waves were less left-biased and therefore more symmetric upon RA inhibition (**Fig.2.6.C,D**). This phenotype differs from earlier reports of the effect of RA inhibition in vertebrate embryos, which described that RA inhibition triggers somite asymmetry (6–8). This discrepancy may reflect the fact that different modes of RA inhibition are not functionally equivalent and may have distinct effects on the regulation of NODAL (8,20–24). In various vertebrate embryos, RA signaling has been shown to be necessary for the induction of NODAL in the LPM. Indeed, in 3- to 6-somite-stage embryos, BMS493 and DEAB treatment led to repression or even loss of *NODAL* expression in the LPM in 7/10 (70%) and 8/26 (31%) of embryos, respectively, compared to 1/30 (3%) in control embryos, possibly resulting in overall weaker lateralization of the anterior somites (**Fig.2.6.E,F**). Therefore, these unexpected increases in somite symmetry observed upon treatment with BMS493 and DEAB are likely caused by suppression of NODAL induction.

To assess the effect of RA signaling on the wildtype left bias in somite patterning that we observed, we treated chick embryos at HH4 with all-trans-RA (2µM). RA treatment disrupted the epithelial organization of the occipital somites, so it was not possible to reliably quantify somite

AP position asymmetry (**Fig.2.6.G**). Therefore, we quantified the asymmetry in *LFNG* traveling waves at the 1- to 5-somite stage while monitoring *NODAL* expression (**Fig.2.6.H**). As previously reported, RA treatment occasionally induced bilateral *NODAL* expression (20,21,23). In embryos with unilateral *NODAL* expression on the left side (n=14/15), we consistently observed that RA treatment rendered *LFNG* traveling waves more symmetric (**Fig.2.6.I,J**). This result is consistent with the expected buffering role of RA in maintaining the bilateral symmetry of somitogenesis dynamics, independently of NODAL transcriptional regulation.

Figure 2.6. RA treatment makes early *LFNG* traveling waves more symmetric

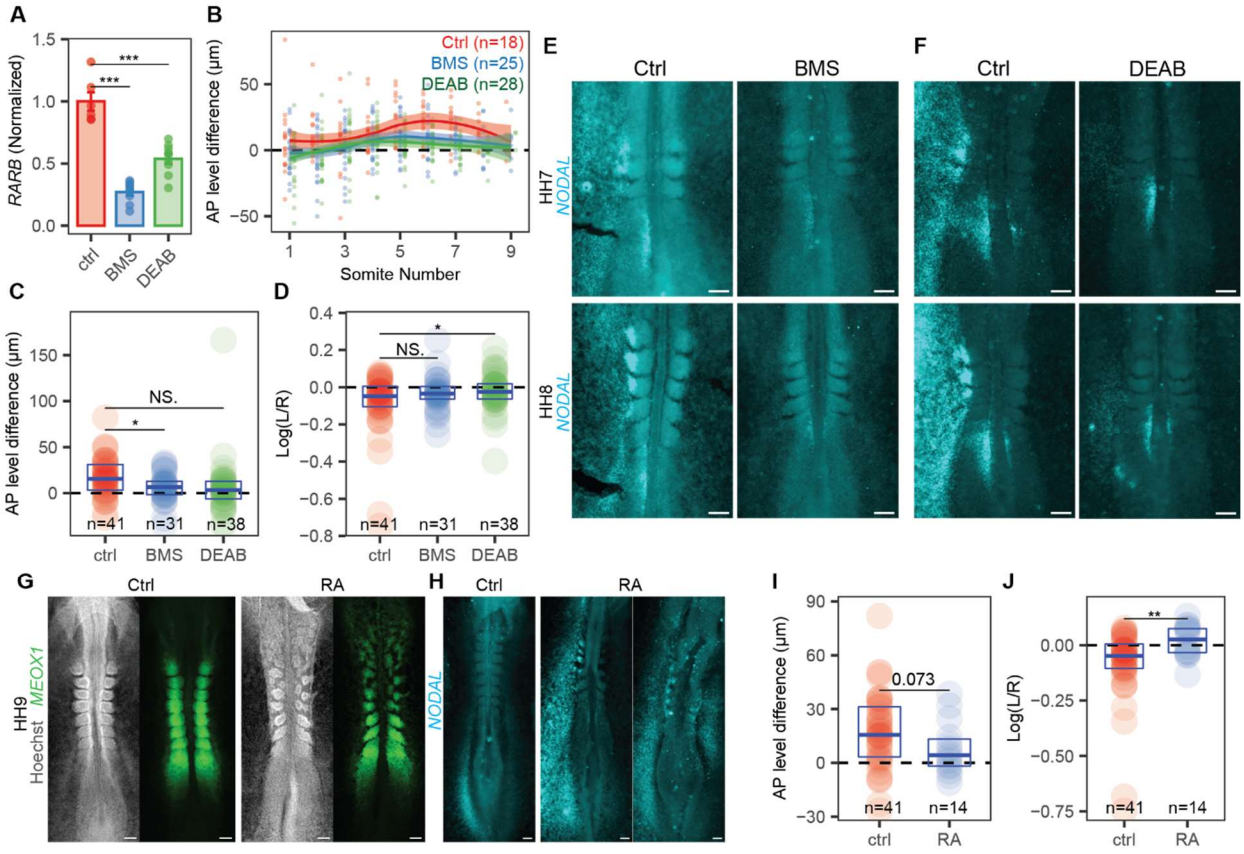

Figure 2.6. (A) *RARB* mRNA level determined by qPCR upon treatment with the RA inverse agonist BMS493 (100μM) and the RALDH2 inhibitor DEAB (100μM). Embryos were treated at HH4-5 and collected after reaching somite stages (HH7 or later). n=6 for the control, and n=9 for BMS493 and DEAB. (B) Somite AP position asymmetry is dampened upon BMS493 and DEAB treatments although the characteristic up-and-down patterns are maintained. (C) AP position and (D) length asymmetry of *LFNG* traveling waves during the augmenting phase are also less asymmetric upon BMS493 and DEAB treatment. (E) BMS493 and (F) DEAB treatment often led to weakening or loss of *NODAL* expression in the LPM at HH7-8. (G) RA (2μM) treatment of chick embryos at HH4 disrupts the epithelial organization of the occipital somites. (H) *NODAL* expression in the anterior LPM is prolonged at HH9 upon treatment with RA (left). Occasionally, RA treatment induces ectopic *NODAL* expression on the right side. (I) AP position asymmetry of *LFNG* traveling waves during the augmenting phase shows a trend toward a reduced left bias upon RA treatment. (J) AP length asymmetry of *LFNG* traveling waves is altered to near symmetry upon RA treatment. Statistics are unpaired two-sided t-test. * is $p < 0.05$; ** is $p < 0.01$; *** is $p < 0.001$. Scale bar = 100μm

The facts that (1) wildtype occipital somites and their underlying patterning processes are asymmetric and (2) RA treatment makes early *LFNG* traveling waves more symmetric suggest that the early paraxial mesoderm producing occipital somite is likely under a low-RA environment, where RA buffering is not fully effective. While an anterior-to-posterior gradient of RA has been demonstrated in the PSM (25), this well-described RA gradient is not established in early stages (26). Thus, the expression patterns of genes encoding enzymes involved in RA metabolism were analyzed with HCR RNA-FISH (**Fig.2.7.A**). Interestingly, at HH7, *CYP26A1* mRNA, which encodes an RA-degrading enzyme, is highly expressed in the tissues surrounding the PSM, including the HN, neuroectoderm, endoderm, and LPM (27). These tissues can act as a RA sink, making RA levels insufficient to protect somitogenesis from the action of NODAL (28,29). Unexpectedly, at HH7, left-biased expression of *CYP26A1* in the LPM was observed (**Fig.2.7.A**). Quantification of *CYP26A1* mRNA signal on the left and right LPM with confocal images of wildtype HH7 chick embryos indeed revealed a robust directional asymmetry of *CYP26A1* (**Fig.2.7.B,C**), raising the possibility that the left paraxial mesoderm might be more dramatically depleted of RA. Additional approaches will be needed to confirm the lack of RA activity in the PSM during the augmenting phase, as well as the asymmetric CYP26A1 protein levels and enzyme activity.

Figure 2.7. mRNA encoding the RA-degrading enzyme CYP26A1 is expressed in the tissues surrounding the early PSM

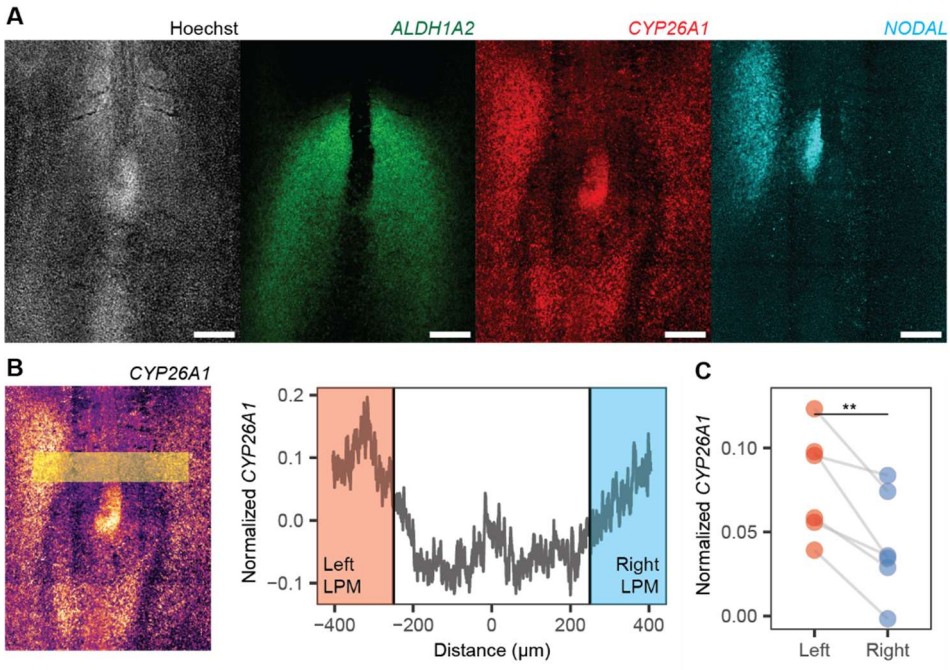

Figure 2.7. (A) Confocal images of a 2-somite stage (HH7) chick embryo with HCR RNA-FISH for *ALDH1A2*, *CYP26A1*, and *NODAL*. (B) Scheme showing quantification of *CYP26A1* signal in the left and right LPM adjacent to the anterior PSM. (C) Comparison of the normalized *CYP26A1* signal at HH7 demonstrates that *CYP26A1* is significantly enriched in the left LPM adjacent to the anterior PSM, revealing a novel molecular asymmetry. n=6. Statistics are a paired two-sample t-test. ** is $p < 0.01$. Scale bar = 200µm

DISCUSSION

Paraxial mesoderm has been largely overlooked in traditional research on LR asymmetry, as bilateral symmetry has been assumed to be the default state of somites. Thus, somite symmetry was mostly studied under specific perturbation conditions, in which it was apparently affected. In other words, under this conventional paradigm, wildtype embryos were easily dismissed as a potential model system for studying bilateral symmetry. Thus, the current work represents one of the first systematic and quantitative analyses of somite bilateral symmetry. In this work, we identified a robust lateralized asymmetry of the anterior-most somites in the early-

stage chick embryo. We expect that this work will provide a solid foundation for future research on somite bilateral symmetry, not only in the chick embryo but also in other vertebrate species. Given the conservation of NODAL as the key left determinant across vertebrate species, it is likely that such somite asymmetries are also present in other model organisms. It is noteworthy, however, that a zebrafish study examining LR asymmetry in somite AP length and boundary position in embryos at the 1- to 6-somite stages did not detect a statistically significant directional bias in these parameters, despite an apparent skew in AP boundary position asymmetry toward one side in the data (5).

The current work mainly focused on how robust lateralized asymmetry is generated in the early PSM. Our analysis of somite AP position asymmetry and gene expression asymmetry underlying somitogenesis also revealed a consistent trend toward progressive achievement of symmetry during development. The initial left bias in somite AP position and associated gene expression is likely generated when NODAL is activated in the anterior presomitic mesoderm and transferred to the LPM. The transient nature of NODAL expression may explain why more posterior asymmetries are not observed. What remains unclear is how asymmetries already present in formed somites, as well as in dynamic somitogenesis processes such as *LFNG* traveling waves, are corrected over time.

One of our most intriguing findings is that asymmetry is mostly observed in the occipital somites. The occipital somites represent the earliest, anterior-most somites (the 1^{st}-5^{th} somites) that later give rise to anatomical structures that are not overtly segmented, such as the basal part of the skull, and the neck, glossal, hypoglossal, and laryngeal muscles (30,31). In addition, although the core machinery for somitogenesis is also involved in the formation of occipital somites (32,33), mouse and zebrafish mutants hint at potential differences in the somitogenesis

of the anterior-most somites. For instance, many mutants that fail to form trunk somites still form varying numbers of anterior-most somites (34–37). Moreover, although it is debated, the occipital somites in the chick embryo were described as forming almost simultaneously, not sequentially (38). While the precise nature of such differences is poorly understood, it is possible that the unique characteristics of occipital somitogenesis contribute to the generation of asymmetry in the occipital somites.

The asymmetries in somite AP position and traveling waves as well as their connection to NODAL signaling have been reported in different contexts. For instance, Amphioxus, an invertebrate chordate representing the sister clade of vertebrates, forms asymmetric somites. Remarkably, this asymmetry, in which the left somites are more anteriorly positioned than the right ones is downstream of NODAL (39,40). The staggered arrangement of left and right somites underlies the LR asymmetry of Amphioxus anatomical structures, including the mouth and pharyngeal organs, which develop on the left side. Although this asymmetry of Amphioxus's somite is reminiscent of our findings in the chick embryo, the functional relevance of morphological asymmetry of somites in the chick embryo remains unclear. Further investigation into the anatomical asymmetry of somite derivatives and adjacent organs might provide a hint about this question.

The Amphioxus somite asymmetry suggests that somitogenesis modulation by the LR machinery may represent an ancestral state. RA-mediated buffering of this asymmetry could represent an evolutionary innovation in vertebrates (40). The findings of the current work, however, suggest that RA-mediated buffering is incomplete and that occipital somites are still sensitive to LR patterning signals.

Furthermore, *NODAL* mRNA expression was detected in the lateral parts of the left occipital somites (**Fig.2.6.E,F**). Moreover, both SAG and NODAL bead treatments in the chick embryo induced ectopic *NODAL* expression not only in the LPM but also in the lateral somite on the right side (**Fig.2.3.B**). These unexpected observations further support the competence of the paraxial mesoderm to be lateralized. The molecular asymmetry of the paraxial mesoderm as well as its developmental consequences will be covered in the next chapter.

In addition, asymmetric expression of Notch-responsive genes and their proposed role in NODAL induction at the HN have previously been described in chick embryos (41,42). A series of studies demonstrated that Notch signaling—including DLL1 and LFNG—are hyperactivated on the left side of HN to induce NODAL at HH6 (pre-somite stage), downstream of a LR asymmetric extracellular $Ca2^{+}$ gradient. The authors showed that treatment with the $Ca2^{+}$ chelator BAPTA and H^{+}/K^{+} ATPase inhibitor omeprazole reduced the asymmetry of DLL1 and LFNG (43). However, treatment with beads soaked in either SHH or an anti-SHH blocking antibody did not alter the reported asymmetry of these gene expression patterns (41). These results appear inconsistent with our results, which show that treatment with beads soaked in SHH-agonist SAG affects the symmetry of *LFNG* traveling waves. However, the two sets of findings are not directly comparable. Our findings are based on the quantitative measurement of *LFNG* traveling wave asymmetry in embryos at early somite stages (HH7-8). Importantly, embryos included in this analysis were labeled by HCR RNA-FISH for *NODAL*, allowing selection of embryos in which LR laterality had been successfully modulated. By contrast, the earlier studies appear to have focused on the pre-somite stage (HH5-6) and did not directly confirm laterality in the treated embryos (41). Moreover, our work did not investigate cyclic gene expression asymmetry at the pre-somite stage (32,33). Thus, while the previous studies

from the Izpisua-Belmonte group provided early evidence for asymmetry in cyclic gene expression (41,42), it is difficult to directly compare their findings with those of the present study because of differences in developmental stage, laterality validation, and analytical approach.

The role of RA signaling in protecting the bilateral symmetry of somitogenesis from the asymmetric signaling environment of LR determination is well established (6–8). Yet the precise role of RA in this process has remained elusive. For instance, the targets through which LR determining signals perturb somitogenesis appeared to vary across species. Mouse mutants for Raldh2 and zebrafish raldh2-morphants showed right-sided expansion of the FGF8 gradient (6,8), but a similarly lateralized alterations to FGF8 gradient was not reported in chick embryos treated with disulfiram (7). Moreover, the opposite directionality of the somitogenesis defect reported in chick embryos, compared with mouse and zebrafish, has remained difficult to explain, although it was attributed to the different directionality of FGF8 in chick and mouse LR determination (7,44). These factors contributed to the lack of consensus on questions such as whether the primary defect reflects left-sided acceleration or right-sided delay, and which aspect of LR asymmetry RA actually buffers against.

Our findings connecting the chick embryo and the human iPSC model provide key insights to these long-standing questions. While other aspects of somitogenesis may also be lateralized by NODAL or by other asymmetric factors, we focused on the modulation of cyclic gene oscillations by NODAL. The experiments in the chick embryo showed that the more anteriorly positioned somite boundary on the left side is likely to result from more advanced traveling waves in the left PSM downstream of NODAL. The human iPSC model provided a compelling mechanistic explanation to this observation, as NODAL was shown to accelerate

HES7 oscillations. Together, these findings offer a possible framework for reconciling the seemingly opposing phenotypes of RA-deficient chick, mouse, and zebrafish embryos. In RA-inhibited chick embryos, somite asymmetry manifested as misalignment of somite boundary positions, where the left somites were more anteriorly positioned than the right ones; by contrast, in mouse and zebrafish mutants for RALDH2, somitogenesis appeared delayed on the right side. It is possible that both phenotypes commonly—and, at least, partially—represent the acceleration of the clock gene oscillation in the left PSM, manifested differently across systems.

At the same time, our RA inhibition experiments in the chick embryo with DEAB and BMS493 differed from the outcomes of earlier work that used disulfiram to inhibit RA signaling in the chick embryo (7). Our results suggest that reduced or absent NODAL induction in the left LPM upon RA inhibition by DEAB and BMS493 led to attenuation of the left bias of somite AP position and *LFNG* traveling waves. Interestingly, different modes of RA inhibition appear to elicit different NODAL outcomes. For instance, pharmacological inhibition of the RA pathway in mouse and zebrafish affects NODAL expression patterns (21,23), whereas mouse genetic mutants for Raldh2 -/- and zebrafish raldh2-morphant exhibit normal left-sided expression of NODAL (8,19). Vitamin A-deficient quail embryos demonstrate left-sided but truncated NODAL expression in the LPM (22). In our data, BMS493 produced stronger suppression of NODAL than DEAB. Thus, it is possible that the differences in the mode of RA inhibition contributed to the discrepancies with previous work. Moreover, our work focused on early-stage embryos (before the 10-somite stage) and on the occipital somites, whereas the somite asymmetries previously described upon RA inhibition by disulfiram in the chick embryo were more posterior in the cervical region and based on the analyses including later-stage embryos (7). It is therefore

also possible that embryos normally engage symmetry-restoring mechanisms at later stages, and that RA inhibition perturbs this corrective process.

Overall, we identify a set of robust lateralized asymmetries in the anterior somites of the chick embryo. Using complementary chick embryo and human iPSC models, we show that the conserved left determinant NODAL underlies this asymmetry by accelerating clock gene oscillations. Our work is expected to provide a novel framework for investigating somite bilateral symmetry, which will motivate future research on both the generation of lateralized asymmetry and the achievement of symmetry in the paraxial mesoderm.

METHODS

Chick embryos

Fertilized chick eggs were acquired from the Charles River Laboratories (for wildtype) and the Susan Chapman Laboratory of Clemson University (for wildtype and transgenic lines ubiquitously expressing GFP (10)). Eggs were incubated at 37°C and 60% humidity.

HCR RNA-FISH

HCR RNA-FISH was performed following the manufacturer's protocol for whole-mount chick embryos (HCR v3.0; Molecular Instruments). Embryos were fixed with 4% paraformaldehyde (PFA) or 4% formaldehyde/2mM EDTA in PBS overnight at 4°C or for 1-2hr at room temperature, washed with PBS, dehydrated in ethanol, and kept in ethanol at -20°C for long-term storage. Before hybridization, embryos were rehydrated through 50% ethanol/50% PBST (PBS with 0.1% Tween 20) and two washes in 100% PBST for 5min each at 4°C. Embryos were then treated with 10µg/mL proteinase K in PBST for 2-3min, post-fixed with 4% PFA for 20min at room temperature, and washed sequentially in PBST and 5x SSCT at 4°C. Embryos were pre-hybridized in probe hybridization buffer (Molecular Instruments) for 30min at 37°C, then incubated overnight at 37°C in 500µL hybridization buffer (Molecular Instruments) containing 2-3pmol of each probe set. HCR probe sets were designed and manufactured by Molecular Instruments. The following day, embryos were washed four times for 15 min each in probe wash buffer at 37°C and twice for 5 min each in 5x SSCT at room temperature. Embryos were then pre-amplified in amplification buffer (Molecular Instruments) for 30 min at room temperature. For amplification, 30pmol each of hairpins h1 and h2 were heated to 95°C for

90sec, cooled to room temperature for 30min, and added to 500µL amplification buffer to prepare a hairpin solution. Embryos were incubated overnight in hairpin solution at room temperature, then washed five times in 5x SSCT. In all experiments except volume asymmetry analysis, Hoechst33342 (Invitrogen; 1:1000) was added to one of the final washes.

Chick embryo manipulation

Chick embryos were collected and cultured using the EC culture protocol in the ventral-up position (45). For bead treatment, Affi-Gel Blue Gel beads (Bio-Rad) were washed in PBS 2-3 times and soaked in SAG (Sigma-Aldrich) or in recombinant human NODAL protein (R&D Systems) diluted in PBS with calcium chloride and magnesium chloride (Sigma-Aldrich; PBS). Depending on the SAG stock used, control beads were soaked either in PBS containing the corresponding dilution of DMSO or in PBS alone. For NODAL experiments, control beads were also soaked in vehicle-matched PBS. A SAG bead was implanted on the right side of the HN at HH4. Multiple NODAL beads were implanted along the right paraxial mesoderm at HH5. For global treatment, embryos were treated with cyclopamine (Selleck Chemicals), DEAB (Sigma-Aldrich), BMS493 (Sigma-Aldrich), or all-trans retinoic acid (Tocris) diluted in PBS. Depending on the cyclopamine stock used, control embryos were treated with PBS containing the corresponding dilution of DMSO or ethanol. For other treatments, control embryos were treated with PBS containing the corresponding dilution of DMSO. For these experiments, 100µL of the treatment or control solution was applied below and above the embryo. The treated embryos were incubated until they reached the desired stages for analysis.

Analysis of somite AP position asymmetry

For the characterization of somite AP position asymmetry in the untreated condition, GFP embryos were windowed in ovo and imaged with a macroscope in the GFP channel from the dorsal side; wildtype embryos were transferred to EC culture with ring-shaped filter paper and imaged with a macroscope in the brightfield channel from the ventral side. Treated/control embryos were imaged with a macroscope from the ventral side before fixation. For experiments perturbing LR determination, only embryos with the expected *NODAL* expression pattern were used. Control embryos for LR-perturbation and RA-modulation experiments were pooled separately for each analysis

Using these images in FIJI, the embryonic midline was defined by manually drawing a segmented line along the midline of the neural tube dorsally or along the notochord ventrally. Next, the posterior boundary of each somite was defined by manually marking two endpoints of a segment of the boundary. The endpoints of each boundary segment were projected onto the midline, and the midpoint between the resulting projection points on the midline was used to represent the AP position of the somite boundary. The distance between the left and right boundary positions was used as a measure of AP position asymmetry for each somite pair. A positive value was assigned when the left somite boundary was positioned more anteriorly than the right boundary, and a negative value was assigned in the opposite case. A custom R script was used for this analysis.

Analysis of somite volume asymmetry

Treated/untreated embryos were collected at the 5- to 9- somite stage and labeled with HCR RNA-FISH for the somite marker *MEOX1* and the left marker *NODAL*. Embryos were

mounted in a block of 1-2% agarose for the iDISCO+ clearing protocol (46). The agarose cube with the embryo was dehydrated in a series of methanol/water solutions (20, 40, 60, 80, 100, 100%) for 1hr each, incubated in a 66% dichloromethane/33% methanol solution for 3hr on a shaker, washed in 100% dichloromethane twice, and incubated in dibenzyl ether. The cleared embryos were imaged with a LaVision Ultramicroscope II (Neurobiology Imaging Facility, Harvard Medical School).

Embryos were imaged such that the AP axis ran roughly in-plane along the Y-axis of the image. To avoid potential effect of laser power imbalances, each sample was imaged twice: once in a position where the left-right body axis ran left-right through the image ("normal"), and once in a reversed position ("reversed") where it ran right-left.

Images were down-sampled in X- and Y-dimensions by a factor of 0.5 (bilinear interpolation) without a change to Z resolution, rotated in 3D such that the AP axis of the embryo was further placed within the image plane and extended from the top to bottom of the in-plane image. AP somite boundaries—and, sometimes, medial boundaries, if necessary—were defined manually as FIJI line segments using a maximum-intensity projection and stored as ROIs. The rest of the boundaries were defined automatically through segmentation of *MEOX1* expression. A gaussian blur of sigma = 3 was applied to the fluorescent *MEOX1* image, and an intensity segmentation threshold was applied at a level uniquely set for each embryo. This threshold was held constant for each "normal" and "reversed" pair of images. Thresholds were set by visually maximizing the potential amount of segmented territory within the somite while minimizing potential background from non-somite tissue. Different thresholds were necessary across embryos due to inter-embryo differences in staining intensities.

Volume measurements of each somite were then produced by a FIJI macro that read the anterior-posterior somite ROIs for each embryo and applied the pre-set threshold. This produced discrete, binarized masks of each embryo's somite. 'Find Connected Regions' was then used within the script to connect all somites in 3D, output a labeled image where each 3D somite has its own unique pixel value, and generate volume measurements corresponding to each 3D somite.

Overlays of the connected regions were constructed on top of the original fluorescent image to evaluate the segmentation. Embryos with visually accurate segmentation of all somites were considered complete. Where tweaking of segmentation was needed, embryos could be re-run with a modified segmentation threshold applied to both the "normal" and "reversed" images in a pair.

For embryos lacking *MEOX1* expression in the core of the somite and thus resulting in holes in the segmentation, a 2nd FIJI macro was used to model the somites as a convex hull. Here, the generated labeled image from macro #1 was provided with a list of somite labels that needed correction. If a somite on one side of the embryo needed convex hull adjustments, the corresponding somite on the contralateral side also received the same treatment, as did the corresponding pair of somites in the other image of the "normal"/"reversed" image-pair. Output .csv files were produced containing somite IDs and somite values that were analyzed in R.

For cyclopamine treatment, the success of treatment could not be assessed by *NODAL* staining because the signal-to-background ratio was not sufficiently consistent for reliable scoring in the staining and imaging conditions used. However, cyclopamine treatment was validated in parallel experiments, in which the success rate was 51/51 (100%).

Analysis of gene expression asymmetry

Treated/untreated embryos were collected at the 1- to 13-somite stage and labeled with HCR RNA-FISH for different combinations of *LFNG*, *MSGN1*, *MESP2*, or *FGF8* probes. For experiments perturbing LR determination, *NODAL* was also visualized to select embryos showing successful treatment outcome. Embryos were mounted on a glass-bottom dish (MatTek) with Fluoromount-G mounting medium (SouthernBiotech) and a glass cover slip. For FGF8 analysis, embryos were imaged with a Zeiss LSM880 confocal microscope (NeuroTechnology Studio, Brigham and Women's Hospital), and maximum-intensity projections were used for analysis. For other analyses, embryos were imaged with a Leica DMi8 widefield microscope (NeuroTechnology Studio, Brigham and Women's Hospital). Control embryos for LR-perturbation and RA-modulation experiments were pooled separately for each analysis

Fluorescence images for a channel of interest were rotated so that the anterior PSM was vertically aligned. Then, a straight ROI was drawn from the anterior boundary of the most recently formed somite to capture the gene expression profile along the PSM of a given side. Next, the ROI was shifted horizontally (without re-aligning it to the anterior boundary of the most recently formed somite on the opposite side) to capture the gene expression profile of the contralateral side. The gene expression profiles of the two sides were normalized by the minimum and maximum values obtained from the combined left and right profiles.

For *LFNG*, the AP range at which the normalized gene expression level exceeds a common threshold (in most cases, 0.5; if this threshold failed to define the left and right traveling waves, a different arbitrary threshold that best matched the apparent traveling waves of both sides was used) was identified as the AP extent of the *LFNG* traveling wave. The AP positions of

the midpoints of the left and right traveling waves were compared to represent the AP position asymmetry of the *LFNG* traveling wave. The distance between the left and right midpoints was used to represent the magnitude of *LFNG* AP position asymmetry. When the left traveling wave was more anteriorly positioned, a positive sign was assigned to the measured distance. The AP extent of the *LFNG* traveling waves were directly compared to analyze *LFNG* length asymmetry. When multiple expression domains were identified, the most anterior pair showing measurable signals on both sides was used for analysis.

For *MESP2*, the peak points of the left and right expression profile were compared to represent the AP position asymmetry of the *MESP2* expression domain. The same logic was applied for sign assignment.

For *MSGN1* and *FGF8*, because the expression profiles showed AP gradients with higher expression posteriorly, the AP levels at which the expression profiles exceeded the common threshold of 0.5 were compared to quantify AP extent asymmetry of *MSGN1* and *FGF8* expression. For *FGF8* analysis, to avoid *FGF8* expression in the primitive streak and the HN and to specifically capture the *FGF8* profile in the PSM, the ROIs were positioned along the PSM such that it does not capture the *FGF8* expression of the midline.

CYP26A1 quantification

Chick embryos labeled with HCR RNA-FISH for *CYP26A1* were imaged with a Zeiss LSM880 confocal microscope (NeuroTechnology Studio, Brigham and Women's Hospital). Maximum-intensity projections were used for analysis. Using FIJI, an ROI (approximately 800μm (ML) * 207μm (AP)) was drawn perpendicular to the midline at the level of the anterior PSM. The measured *CYP26A1* signal intensity across 150μm at each end of the ROI was used to

represent *CYP26A1* expression in the left and right LPM. *CYP26A1* intensities were normalized first to the Hoechst33342 channel to control for differences in tissue density and then to the average normalized intensity of each embryo to account for between-embryo variation.

Human pluripotent stem cell culture

Human stem cell work was approved by the Partners Human Research Committee (2017P000438/PHS) and performed in compliance with all relevant ethical regulations. We used NCRM1 iPS cells (RUCDR, Rutgers University) with the written informed consent of the donor obtained by Rutgers University at the time of sample collection. For maintenance, 500000 cells were initially seeded in each well of Matrigel-coated 6-well plates (Corning) in mTeSR1 medium (StemCell Technologies) supplemented with 10μM ROCK inhibitor Y-27632 (Tocris). Fresh mTeSR1 medium was applied every day. Cells were passed every 3-5 days depending on confluency. For passages, cells were dissociated with Accutase (Corning).

2D Differentiation of human iPSCs and time-lapse imaging

For differentiation to a posterior-PSM-like state, 300000 cells carrying HES7-Achilles were seeded in each well of Matrigel-coated 6-well plates (Corning) in mTeSR1 medium (StemCell Technologies) supplemented with 10μM ROCK inhibitor Y-27632 (Tocris). Cells were cultured for 24hr and, on day 0, the medium was replaced with the DICL medium: DMEM/F-12 GlutaMAX (Gibco) supplemented with 1% Insulin Transferrin Selenium (Gibco), 3μM Chir99021 (Tocris), and 0.5μM LDN193189 (Stemgent). On day 1, the medium was replaced with fresh DICL medium. On day 2, cells were dissociated with Accutase (Corning) and resuspended in the clock medium: DMEM/F-12 GlutaMAX (Gibco) supplemented with 1%

Insulin Transferrin Selenium (Gibco), 3μM Chir99021 (Tocris), 0.5μM LDN193189 (Stemgent), 10μM Y-27632 (Tocris), 50ng/ml mFGF4 (R&D Systems), 1μg/ml Heparin (Sigma Aldrich), and 2.5μM BMS493 (Sigma Aldrich). 500000 cells were seeded in each well of a fibronectin-coated ibidi 24-well plate with polymer coverslip bottom (ibidi). For B- conditions, BMS493 was removed from the base clock medium. For N+ and N++ conditions, 0.2 or 0.5μg/ml recombinant human NODAL protein (R&D Systems) was added. For the controls of experiments with NODAL treatment, a corresponding volume of 4mM HCl was added to the clock medium.

Cells in the clock medium with or without treatment were imaged with a Zeiss LSM780 confocal microscope with an incubation chamber for temperature and CO2 control. Achilles YFP fluorescence was excited with an argon laser (514nm, 20-40μW). A Plan-Apochromat 20x/0.80 objective was used to capture a 2x2 tile (1600x1600 pixel; 850x850μm) region per well every 10 minutes.

Analysis of HES7-Achilles time-lapse image

FIJI was used for background subtraction and Gaussian blurring. An ROI was drawn to acquire the mean fluorescence intensity over time. The peaks of the oscillating mean fluorescence intensity were manually identified to calculate the period. For the period analysis, the first five periods of samples displaying at least five periods were used. The experiment included cells with the base clock medium and base clock medium containing vehicle control for NODAL treatment (a corresponding volume of 4mM HCl). These two conditions showed very similar distributions of periods and thus were pooled as B+ for analysis (Base clock medium median period=4.767hr [4.667,4.842]; Base clock medium containing the vehicle control median period=4.767hr [4.633,4.867]).

For the visualization of detrended HES7-Achilles traces, the mean fluorescence intensity for each well of an experiment was detrended with robust LOESS regression (span=0.3). The average detrended trace for each condition was smoothed with LOESS (span=0.18) for visualization.

RT-qPCR

For chick embryo tissue, embryos were treated at HH4-5 with 100µM BMS493 or DEAB diluted in PBS and collected after reaching somite stages (HH7 or later). Embryonic tissues from the first somite to the posterior PSM, including some LPM tissue, were dissected and used for mRNA extraction using the RNeasy Micro Kit (Qiagen). A Nanodrop spectrophotometer was used to evaluate RNA concentration. A cDNA library was constructed with the iScript cDNA Synthesis Kit (Bio-Rad), using 90ng of RNA. The resulting cDNA library was diluted 1:8 with water, and RT-qPCR was performed. Each well consisted of 5µl iTaq Universal SYBR Green Supermix (Bio-Rad), 0.4µl of primer solution (10µM forward and reverse primers), and 4.6µl of cDNA. Primer sequences are listed in the table below (Table.2.1.). Three technical replicates were performed. For RT-qPCR, the following protocol was used: 95°C for 1min; 40 cycles of 95°C for 5sec, 60°C for 40sec; 65°C for 31sec; 60 cycles of 65°C for 5sec, with +0.5°C/cycle and a ramp 0.5°C/s. For gene expression analysis, Ct values were normalized to *RPL15*, and the resulting normalized Ct values were then normalized against the average of the control samples. When the standard deviation of Ct values among triplicates exceeded 0.5, the obvious outlier was excluded, and the standard deviation was recalculated. If the standard deviation remained above 0.5 after outlier exclusion, that sample was excluded from analysis for the corresponding target.

For human iPSCs, cells were washed with PBS twice, suspended using a cell scraper in PBS, and centrifuged at 4000rpm for 5min to remove the supernatant. mRNA was extracted with the RNeasy Plus Mini Kit (Qiagen). A cDNA library was constructed with the iScript cDNA Synthesis Kit (Bio-Rad), using 1µg of RNA. The resulting cDNA library was diluted 1:30 in water. The same RT-qPCR protocol described above was used. For gene expression analysis, Ct values were normalized to *PPIA*, and normalized Ct values were then normalized against the average of the base clock medium (B+).

Table.2.1. Primer sequences for qPCR

Gene	**Forward**	**Reverse**	**Reference**
hPPIA	TCTGCCCACCTTAACAGACC	AATTCACGCAGAAGGAACCA	Diaz-Cuadros et al. (4)
hRARB	CCCCAGAACAAGACACCATGA	TTTTGTCGGTTCCTCAAGGTC	Butsri et al. (47)
hNODAL	AGACATCATCCGCAGCCTA	CAAAAGCAAACGTCCAGTTCT	Martyn et al. (48)
hMSGN1	AGAGGGAGAAGCTCAGGATGAG	GTGTCTGGATCTTGGTGAGAGG	OriGene
hTBX6	CATCCACGAGAATTGTACCCG	AGCAATCCAGTTTAGGGGTGT	PrimerBank
hFGF8	TCATCCGGACCTACCAACTC	CTCGGACTCGAACTCTGCTT	Diaz-Cuadros et al. (4)
hDUSP6	CCAAATCATGGGCTCACTTT	CCATGCTCACACACACACAC	Diaz-Cuadros et al. (4)
cRPL15	GCTCGCAGGCTGGGATATAA	GCACAGGCTTCCCATAGGTT	Wang et al. (49)
cRARB	GTGTCAGTGCTTGTGAGGGA	TGCAGTACTGGCAGCGATTT	Thiede et al. (50)

REFERENCES

1. Eitler K, Bibok A, Telkes G. Situs Inversus Totalis: A Clinical Review. International Journal of General Medicine. 2022 Mar 3;15:2437–49. doi:10.2147/IJGM.S295444 PubMed PMID: 35264880.

2. Shiraishi I, Ichikawa H. Human Heterotaxy Syndrome. Circulation Journal. 2012;76(9):2066–75. doi:10.1253/circj.CJ-12-0957

3. Palmeirim I, Henrique D, Ish-Horowicz D, Pourquié O. Avian hairy Gene Expression Identifies a Molecular Clock Linked to Vertebrate Segmentation and Somitogenesis. Cell. 1997 Nov 28;91(5):639–48. doi:10.1016/S0092-8674(00)80451-1

4. Diaz-Cuadros M, Wagner DE, Budjan C, Hubaud A, Tarazona OA, Donelly S, et al. In vitro characterization of the human segmentation clock. Nature. 2020 Apr;580(7801):113–8. doi:10.1038/s41586-019-1885-9

5. Naganathan SR, Popović M, Oates AC. Left–right symmetry of zebrafish embryos requires somite surface tension. Nature. 2022 May;605(7910):516–21. doi:10.1038/s41586-022-04646-9

6. Vermot J, Llamas JG, Fraulob V, Niederreither K, Chambon P, Dollé P. Retinoic Acid Controls the Bilateral Symmetry of Somite Formation in the Mouse Embryo. Science. 2005 Apr 22;308(5721):563–6. doi:10.1126/science.1108363

7. Vermot J, Pourquié O. Retinoic acid coordinates somitogenesis and left–right patterning in vertebrate embryos. Nature. 2005 May;435(7039):7039. doi:10.1038/nature03488

8. Kawakami Y, Raya Á, Raya RM, Rodríguez-Esteban C, Belmonte JCI. Retinoic acid signalling links left–right asymmetric patterning and bilaterally symmetric somitogenesis in the zebrafish embryo. Nature. 2005 May;435(7039):7039. doi:10.1038/nature03512

9. Reijntjes S, Stricker S, Mankoo BS. A comparative analysis of <I>Meox1</I> and <I>Meox2</I> in the developing somites and limbs of the chick embryo. The International Journal of Developmental Biology. 2007 Oct 1;51(8):753–9. doi:10.1387/ijdb.072332sr

10. Chapman SC, Lawson A, Macarthur WC, Wiese RJ, Loechel RH, Burgos-Trinidad M, et al. Ubiquitous GFP expression in transgenic chickens using a lentiviral vector. Development. 2005 Mar;132(5):935–40. doi:10.1242/dev.01652 PubMed PMID: 15673573.

11. Cooke J, Zeeman EC. A clock and wavefront model for control of the number of repeated structures during animal morphogenesis. Journal of Theoretical Biology. 1976 Jan 1;58(2):455–76. doi:10.1016/S0022-5193(76)80131-2

12. Dubrulle J, McGrew MJ, Pourquié O. FGF Signaling Controls Somite Boundary Position and Regulates Segmentation Clock Control of Spatiotemporal Hox Gene Activation. Cell. 2001 Jul 27;106(2):219–32. doi:10.1016/S0092-8674(01)00437-8

13. Wittler L, Shin E ha, Grote P, Kispert A, Beckers A, Gossler A, et al. Expression of Msgn1 in the presomitic mesoderm is controlled by synergism of WNT signalling and Tbx6. EMBO Rep. 2007 Aug;8(8):784–9. doi:10.1038/sj.embor.7401030 PubMed PMID: 17668009; PubMed Central PMCID: PMC1978083.

14. McGrew MJ, Dale JK, Fraboulet S, Pourquié O. The *lunatic Fringe* gene is a target of the molecular clock linked to somite segmentation in avian embryos. Current Biology. 1998 Aug 27;8(17):979–82. doi:10.1016/S0960-9822(98)70401-4

15. Aulehla A, Johnson RL. Dynamic Expression oflunatic fringeSuggests a Link betweennotchSignaling and an Autonomous Cellular Oscillator Driving Somite Segmentation. Developmental Biology. 1999 Mar 1;207(1):49–61. doi:10.1006/dbio.1998.9164

16. Saga Y, Hata N, Koseki H, Taketo MM. Mesp2: a novel mouse gene expressed in the presegmented mesoderm and essential for segmentation initiation. Genes Dev. 1997 Jul 1;11(14):1827–39. doi:10.1101/gad.11.14.1827 PubMed PMID: 9242490.

17. Levin M, Johnson RL, Stern CD, Kuehn M, Tabin C. A molecular pathway determining left-right asymmetry in chick embryogenesis. Cell. 1995 Sep 8;82(5):803–14. doi:10.1016/0092-8674(95)90477-8

18. Uehara M, Yashiro K, Takaoka K, Yamamoto M, Hamada H. Removal of maternal retinoic acid by embryonic CYP26 is required for correct Nodal expression during early embryonic patterning. Genes Dev. 2009 Jul 15;23(14):1689–98. doi:10.1101/gad.1776209 PubMed PMID: 19605690.

19. Niederreither K, Vermot J, Messaddeq N, Schuhbaur B, Chambon P, Dollé P. Embryonic retinoic acid synthesis is essential for heart morphogenesis in the mouse. Development. 2001 Apr 1;128(7):1019–31. doi:10.1242/dev.128.7.1019

20. Tsukui T, Capdevila J, Tamura K, Ruiz-Lozano P, Rodriguez-Esteban C, Yonei-Tamura S, et al. Multiple left-right asymmetry defects in Shh−/− mutant mice unveil a convergence of the Shh and retinoic acid pathways in the control of Lefty-1. Proceedings of the National Academy of Sciences. 1999 Sep 28;96(20):11376–81. doi:10.1073/pnas.96.20.11376

21. Chazaud C, Chambon P, Dollé P. Retinoic acid is required in the mouse embryo for left-right asymmetry determination and heart morphogenesis. Development. 1999 Jun 15;126(12):2589–96. doi:10.1242/dev.126.12.2589

22. Zile MH, Kostetskii I, Yuan S, Kostetskaia E, St. Amand TR, Chen Y, et al. Retinoid Signaling Is Required to Complete the Vertebrate Cardiac Left/Right Asymmetry Pathway. Developmental Biology. 2000 Jul 15;223(2):323–38. doi:10.1006/dbio.2000.9754

23. Huang S, Ma J, Liu X, Zhang Y, Luo L. Retinoic Acid Signaling Sequentially Controls Visceral and Heart Laterality in Zebrafish. J Biol Chem. 2011 Aug 12;286(32):28533–43. doi:10.1074/jbc.M111.244327 PubMed PMID: 21669875; PubMed Central PMCID: PMC3151095.

24. Niederreither K, Vermot J, Messaddeq N, Schuhbaur B, Chambon P, Dolle P. Embryonic retinoic acid synthesis is essential for heart morphogenesis in the mouse. Development. 2001 Apr 1;128(7):1019–31. doi:10.1242/dev.128.7.1019

25. del Corral RD, Olivera-Martinez I, Goriely A, Gale E, Maden M, Storey K. Opposing FGF and Retinoid Pathways Control Ventral Neural Pattern, Neuronal Differentiation, and Segmentation during Body Axis Extension. Neuron. 2003 Sep 25;40(1):65–79. doi:10.1016/S0896-6273(03)00565-8

26. Swindell EC, Thaller C, Sockanathan S, Petkovich M, Jessell TM, Eichele G. Complementary Domains of Retinoic Acid Production and Degradation in the Early Chick Embryo. Developmental Biology. 1999 Dec 1;216(1):282–96. doi:10.1006/dbio.1999.9487

27. Blentic A, Gale E, Maden M. Retinoic acid signalling centres in the avian embryo identified by sites of expression of synthesising and catabolising enzymes. Developmental Dynamics. 2003;227(1):114–27. doi:10.1002/dvdy.10292

28. Rydeen A, Voisin N, D'Aniello E, Ravisankar P, Devignes CS, Waxman JS. Excessive feedback of Cyp26a1 promotes cell non-autonomous loss of retinoic acid signaling. Dev Biol. 2015 Sep 1;405(1):47–55. doi:10.1016/j.ydbio.2015.06.008 PubMed PMID: 26116175; PubMed Central PMCID: PMC4529768.

29. Rydeen AB, Waxman JS. Cyp26 enzymes are required to balance the cardiac and vascular lineages within the anterior lateral plate mesoderm. Development. 2014 Apr 15;141(8):1638–48. doi:10.1242/dev.105874

30. Couly GF, Coltey PM, Le Douarin NM. The triple origin of skull in higher vertebrates: a study in quail-chick chimeras. Development. 1993 Feb 1;117(2):409–29. doi:10.1242/dev.117.2.409

31. Huang R, Zhi Q, Patel K, Wilting J, Christ B. Contribution of single somites to the skeleton and muscles of the occipital and cervical regions in avian embryos. Anat Embryol. 2000 Oct 1;202(5):375–83. doi:10.1007/s004290000131

32. Jouve C, Iimura T, Pourquie O. Onset of the segmentation clock in the chick embryo: evidence for oscillations in the somite precursors in the primitive streak. Development. 2002 Mar 1;129(5):1107–17. doi:10.1242/dev.129.5.1107

33. Maia-Fernandes AC, Martins-Jesus A, Borralho-Martins N, Pais-de-Azevedo T, Magno R, Duarte I, et al. Spatio-temporal dynamics of early somite segmentation in the chicken embryo. PLoS One. 2024 Apr 18;19(4):e0297853. doi:10.1371/journal.pone.0297853 PubMed PMID: 38635504; PubMed Central PMCID: PMC11025740.

34. Oates AC, Rohde LA, Ho RK. Generation of segment polarity in the paraxial mesoderm of the zebrafish through a T-box-dependent inductive event. Developmental Biology. 2005 Jul 1;283(1):204–14. doi:10.1016/j.ydbio.2005.04.012

35. Oates AC, Ho RK. Hairy/E(spl)-related (Her) genes are central components of the segmentation oscillator and display redundancy with the Delta/Notch signaling pathway in the formation of anterior segmental boundaries in the zebrafish. Development. 2002 Jun 15;129(12):2929–46. doi:10.1242/dev.129.12.2929

36. Therapontos C, Vargesson N. Zebrafish notch signalling pathway mutants exhibit trunk vessel patterning anomalies that are secondary to somite misregulation. Developmental dynamics : an official publication of the American Association of Anatomists. 2010 Oct 1;239:2761–8. doi:10.1002/dvdy.22410

37. Chalamalasetty RB, Garriock RJ, Dunty WC Jr, Kennedy MW, Jailwala P, Si H, et al. Mesogenin 1 is a master regulator of paraxial presomitic mesoderm differentiation. Development. 2014 Nov 15;141(22):4285–97. doi:10.1242/dev.110908

38. Dias AS, de Almeida I, Belmonte JM, Glazier JA, Stern CD. Somites Without a Clock. Science. 2014 Feb 14;343(6172):791–5. doi:10.1126/science.1247575

39. Schubert M, Holland LZ, Stokes MD, Holland ND. Three Amphioxus *Wnt* Genes (*AmphiWnt3*, *AmphiWnt5*, and *AmphiWnt6*) Associated with the Tail Bud: the Evolution of Somitogenesis in Chordates. Developmental Biology. 2001 Dec 1;240(1):262–73. doi:10.1006/dbio.2001.0460

40. Soukup V, Yong LW, Lu TM, Huang SW, Kozmik Z, Yu JK. The Nodal signaling pathway controls left-right asymmetric development in amphioxus. EvoDevo. 2015 Feb 17;6:5. doi:10.1186/2041-9139-6-5 PubMed PMID: 25954501; PubMed Central PMCID: PMC4423147.

41. Raya Á, Kawakami Y, Rodríguez-Esteban C, Büscher D, Koth CM, Itoh T, et al. Notch activity induces Nodal expression and mediates the establishment of left–right asymmetry in vertebrate embryos. Genes Dev. 2003 May 15;17(10):1213–8. doi:10.1101/gad.1084403 PubMed PMID: 12730123; PubMed Central PMCID: PMC196060.

42. Raya Á, Kawakami Y, Rodríguez-Esteban C, Ibañes M, Rasskin-Gutman D, Rodríguez-León J, et al. Notch activity acts as a sensor for extracellular calcium during vertebrate left–right determination. Nature. 2004 Jan;427(6970):121–8. doi:10.1038/nature02190

43. Raya Á, Kawakami Y, Rodríguez-Esteban C, Ibañes M, Rasskin-Gutman D, Rodríguez-León J, et al. Notch activity acts as a sensor for extracellular calcium during vertebrate left–right determination. Nature. 2004 Jan;427(6970):6970. doi:10.1038/nature02190

44. Meyers EN, Martin GR. Differences in left-right axis pathways in mouse and chick: Functions of FGF8 and SHH. Science. 1999 Jul 16;285(5426):403–6.

45. Chapman SC, Collignon J, Schoenwolf GC, Lumsden A. Improved method for chick whole-embryo culture using a filter paper carrier. Developmental Dynamics. 2001;220(3):284–9. doi:10.1002/1097-0177(20010301)220:3<284::AID-DVDY1102>3.0.CO;2-5

46. Renier N, Adams EL, Kirst C, Wu Z, Azevedo R, Kohl J, et al. Mapping of Brain Activity by Automated Volume Analysis of Immediate Early Genes. Cell. 2016 Jun 16;165(7):1789–802. doi:10.1016/j.cell.2016.05.007 PubMed PMID: 27238021.

47. Butsri S, Kukongviriyapan V, Senggunprai L, Kongpetch S, Prawan A. All-trans-retinoic acid induces RARB-dependent apoptosis via ROS induction and enhances cisplatin sensitivity by NRF2 downregulation in cholangiocarcinoma cells. Oncol Lett. 2022 Jun;23(6):179. doi:10.3892/ol.2022.13299 PubMed PMID: 35464301; PubMed Central PMCID: PMC9025595.

48. Martyn I, Kanno TY, Ruzo A, Siggia ED, Brivanlou AH. Self-organization of a human organizer by combined WNT and NODAL signalling. Nature. 2018 Jun;558(7708):132–5. doi:10.1038/s41586-018-0150-y PubMed PMID: 29795348; PubMed Central PMCID: PMC6077985.

49. Wang Y, Zhang YQ, Wu ZW, Fang T, Wang F, Zhao H, et al. Selection of reference genes for RT-qPCR analysis in developing chicken embryonic ovary. Mol Biol Rep. 2023 Apr 1;50(4):3379–87. doi:10.1007/s11033-023-08280-0

50. Thiede BR, Mann ZF, Chang W, Ku YC, Son YK, Lovett M, et al. Retinoic acid signalling regulates the development of tonotopically patterned hair cells in the chicken cochlea. Nat Commun. 2014 May 20;5(1):3840. doi:10.1038/ncomms4840

Chapter 3

Molecular Asymmetry and Developmental Fate of Anterior Somites

Author contributions: Jong Gwan Lee and Olivier Pourquié conceptualized the study. Jong Gwan Lee performed the experiments and analyzed the data. Ségolène Bernheim analyzed the fate map experiments and contributed to the figures and the writings related to the heart. Gauthier Toulouse assisted in the staining of chick embryo sections. Kongju Zhu and Gauthier Toulouse assisted in the preparation of the electroporation plasmids. Alejandra Rodríguez-delaRosa and Yannis Djeffal assisted in the single-cell RNA sequencing. Jong Gwan Lee and Olivier Pourquié wrote the manuscript. Olivier Pourquié supervised the project.

INTRODUCTION

Left-right (LR) asymmetry is a conserved feature of the vertebrate body plan that is established early in development and essential for the proper positioning and morphogenesis of visceral organs. Central to this process is the NODAL signaling pathway, a member of the transforming growth factor beta (TGF-β) superfamily (1). The earliest known symmetry-breaking mechanisms vary across different vertebrate species (2–5), but they converge on the left-sided activation of NODAL signaling in the embryonic organizer, such as Hensen's node (HN) in the chick embryo. Asymmetric NODAL signaling in the embryonic organizer is transferred to and transiently amplified in the lateral plate mesoderm (LPM) to activate a downstream signaling cascade, including the induction of the left-specific transcription factor *PITX2* (6–8). The regulation and downstream effectors of NODAL signaling in the embryonic organizer, the LPM, and asymmetrically developing organs have been extensively studied. However, whether other embryonic tissues are molecularly and developmentally lateralized during these early stages is poorly understood.

The paraxial mesoderm and somites have generally been overlooked in research of LR asymmetry, while being assumed to be bilaterally symmetric. However, previous observations of molecular asymmetry in the paraxial mesoderm of the chick embryo during the LR patterning process argue against such a view. For instance, *CER1*, an antagonist of the bone morphogenetic proteins (BMP) signaling pathway, is broadly expressed in the left LPM and anterior paraxial mesoderm and is necessary for the induction of NODAL in the LPM (9,10). Moreover, the *NODAL* transcript itself is also asymmetrically expressed in the left anterior PSM (1,11). These observations align with a classic co-culture experiment using chick tissue explants: a co-culture of right LPM tissue and a SHH bead alone failed to induce *NODAL*, whereas a co-culture of right LPM tissue with a SHH bead and paraxial tissue induced NODAL, showing the necessity of

paraxial tissue for the proper induction of *NODAL* in LPM explants (12). Yet the view of a bilaterally symmetric paraxial mesoderm persisted despite these observations. Whether the somites themselves are molecularly lateralized has not been investigated.

The anterior occipital somites (1^{st}-5^{th} somites) are a promising model for investigating molecular asymmetry in the paraxial mesoderm. These somites form concurrently with the LR patterning process and exhibit distinguishing developmental properties, compared to the trunk somites, including maturation dynamics and gene expression profiles (13–16). They also lie between the major centers of NODAL induction at the HN and the LPM and are adjacent to tissues associated with LR-asymmetric morphogenesis, including the cardiac mesoderm and cardiac neural crest cells (CNCCs). If anterior somites are molecularly asymmetric, they could be a previously unrecognized contributor to LR asymmetric organogenesis.

Here, we analyzed LR asymmetry in the paraxial mesoderm of the early chick embryo. Using HCR RNA-FISH, we found that the lateral parts of the anterior somites are molecularly asymmetric. We performed side-specific single-cell RNA sequencing and identified novel asymmetric genes in a tissue-specific manner. Leveraging these findings, we also revisited the fate map of these asymmetric occipital somites in a side-specific manner to demonstrate that left and right anterior somites asymmetrically contribute to the heart. Lastly, we show that modulation of the molecular laterality of anterior somite grafts affects their fate contribution and normal cardiac development, highlighting a functional role for somite molecular laterality in vertebrate LR-asymmetric development.

RESULTS

NODAL is expressed in the lateral parts of the anterior somites

To revisit molecular asymmetry in the paraxial mesoderm during the early LR patterning process, *NODAL* mRNA expression in Hamburger-Hamilton (HH) stage 7-8 chick embryos was analyzed using HCR RNA-FISH (17). Traditionally, at HH7-8 (1-6 somite stage), *NODAL* has been described to be expressed in the anterior part of the PSM adjacent to the HN and in the LPM, but not in the somites (1). Unexpectedly, however, our analysis revealed that *NODAL* is very strongly expressed in the lateral parts of anterior somites, most commonly in the 1st-4th somites (**Fig. 3.1A,B**). Indeed, *NODAL* expression was observed in cells showing clear signatures of epithelial somite cells and expression of the somite marker *MEOX1* (18). When we implanted beads soaked with human recombinant NODAL protein (50μg/ml) next to the paraxial mesoderm of HH5-8 chick embryos and incubated them for 6hr, strong expression of both *NODAL* and *PITX2* was observed by HCR RNA-FISH on the lateral side of the anterior somites (**Fig. 3.1C**). Moreover, this pattern of *NODAL* expression in the lateral parts of the anterior somites during the transfer of NODAL signaling to the LPM is likely conserved in mammals as well, as HCR RNA-FISH for *NODAL* and *MEOX1* in E8.0 mouse embryos (4-somite stage) exhibited *NODAL* expression in the corresponding parts of the anterior somites (**Fig. 3.1D**). These findings demonstrate that lateral somite cells at the occipital level are competent to become lateralized and molecularly asymmetric, expressing core left-determining factors such as *NODAL* and *PITX2*.

Figure 3.1. Molecular asymmetry of anterior somites

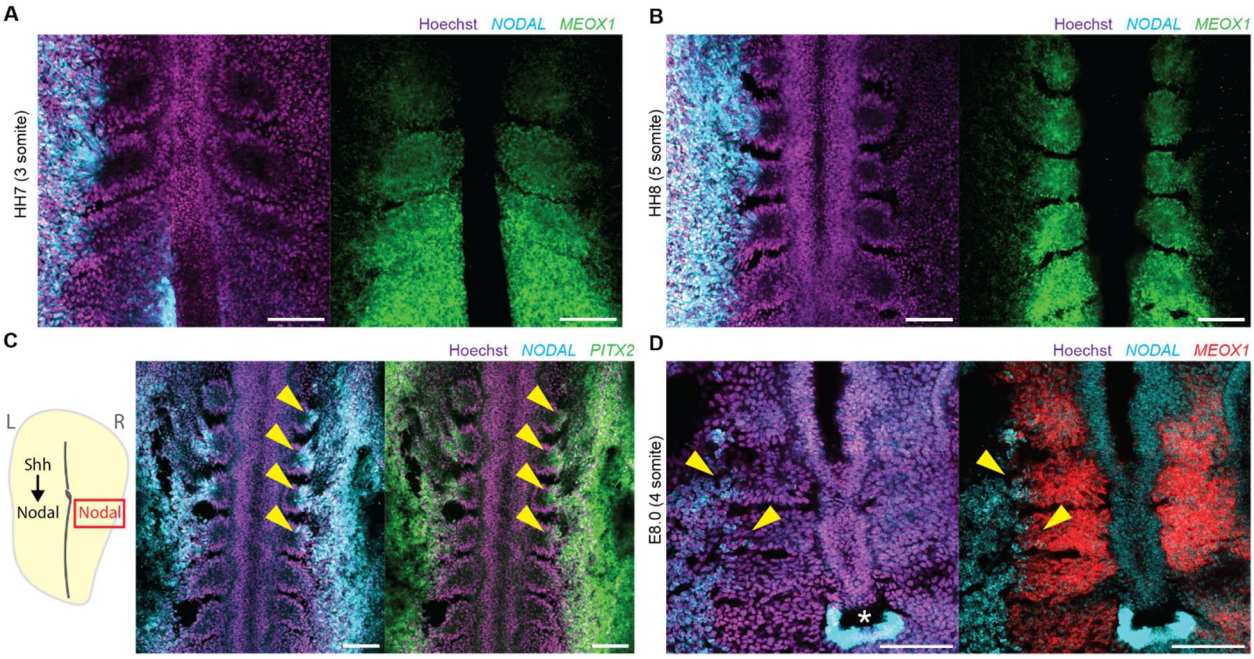

Figure 3.1. (A) A HH7 (3-somite stage) and (B) a HH8 (5-somite stage) chick embryo labeled with HCR RNA-FISH for *MEOX1* and *NODAL*. The lateral parts of the anterior somites express NODAL. (C) Implanting beads soaked in human recombinant NODAL (50µg/ml) along the paraxial mesoderm of HH5-8 chick embryos induced ectopic expression of *NODAL* and *PITX2* in the lateral parts of the right anterior somites. Yellow arrowheads point to ectopic *NODAL* (cyan) and *PITX2* (green) expression in the lateral parts of the right 1st-4th somites. (D) An E8.0 (4-somite stage) mouse embryo labeled with HCR RNA-FISH for *MEOX1* and *NODAL*. Yellow arrowheads point to *NODAL* expression in the lateral parts of the left 2nd and 3rd somites. The asterisk indicates the node. Scale bar = 100µm

Single cell RNA sequencing of left versus right sides of chick embryo

To further investigate the molecular asymmetry of the early chick embryo in an unbiased manner, we performed side-specific single-cell RNA sequencing. Using this approach, we aimed to characterize the transcriptomic landscape of these lateral somite cells that are molecularly asymmetric and to discover novel LR asymmetric genes. The 4-somite stage embryos were bisected along the midline, and the left and right tissues—from the first somite to the 30-50% level of the PSM in the AP direction, and from the midline to the border between LPM and the extraembryonic tissue in the ML direction—were separately collected by pooling 4 embryos (**Fig.3.2A**). The left and right samples were separately sequenced and merged for downstream analysis. We sequenced a total of 17490 cells (left: 9057 and right: 8433; n=4).

The left and right cells on the UMAP mostly overlapped, except for a domain outlined by a dotted line where left and right cells were separated by side (**Fig.3.2B**). The expression patterns of the somite marker *MEOX1*, the LPM marker *HAND1*, and the left determinant *NODAL* indicated that these cells represent LPM cells undergoing NODAL induction (**Fig.3.2C**). Interestingly, the expression pattern of the W chromosome gene *HINTW*, which is ubiquitously expressed by ZW (female) cells (19), revealed that LPM cells not only separate by side but also by sex chromosome, generating four apparent cell clusters that represent the left and right LPM of ZZ and ZW embryos (**Fig.3.2C**). The cells showed a bimodal distribution of *HINTW* expression, revealing the inclusion of both ZZ (male) and ZW (female) embryos in our sample. For ease of analysis, ZZ and ZW cells were separated based on *HINTW* expression (ZZ: normalized expression < 0.1), and ZZ cells were primarily used for analysis.

Figure 3.2. A side-specific single-cell RNA sequencing of HH8 chick embryo

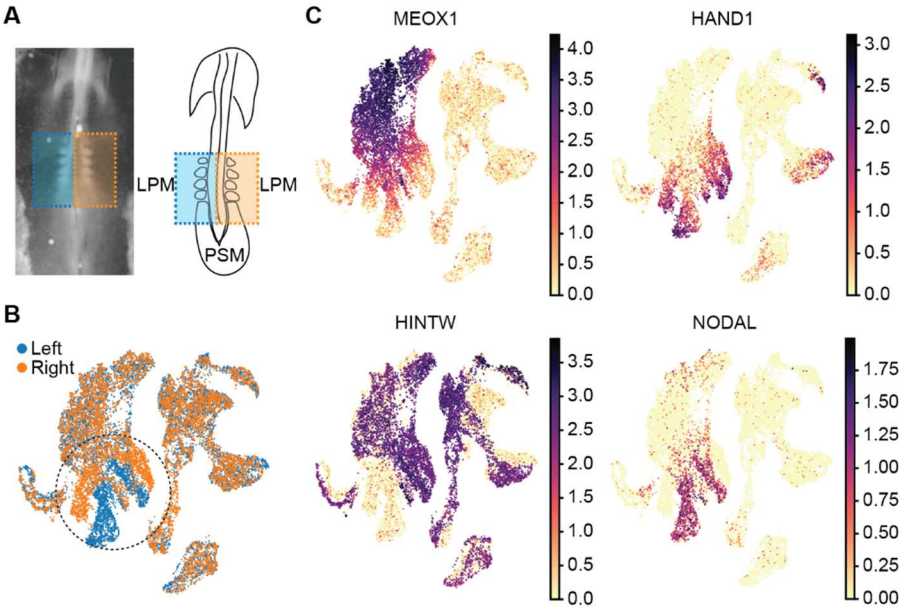

Figure 3.2. (A) Dissection of an HH8 (4-somite stage) chick embryo for left and right single-cell RNA sequencing. Four embryos were pooled. (B) Single-cell RNA sequencing of left and right tissue samples shows a region of the UMAP where cells are separated by side (dotted circle). (C) The expression patterns of the somite marker *MEOX1*, the LPM marker *HAND1*, the W chromosome marker *HINTW*, and the left marker *NODAL* show that a subset of mesoderm cells separates by both side and sex chromosome. Cells were divided into ZZ (male) and ZW (female) subsets, based on normalized *HINTW* expression.

The UMAP of ZZ cells demonstrated clear separation of LPM cells by side, whereas the cells of other regions largely overlapped (**Fig.3.3A**). Clusters of different germ layers were identified (**Fig.3.3B**), based on common markers for tissues at these early stages (**Fig.3.3C**). The distribution of markers for mesoderm (*PITX2*, *MSGN1*, *TCF15*, *HAND1*) and ectoderm (*SOX2*, *PAX7*, *TFAP2A*) suggested that cells belonging to these germ layers represent most of our sample. Furthermore, the left-specific distribution of *PITX2* together with the clear separation of mesoderm cells by side not only validated the clean execution of the experiment but also identified the mesoderm as the primary site of molecular lateralization during the early phase of LR determination.

Figure 3.3. Clusters representing various tissue types of ZZ cells

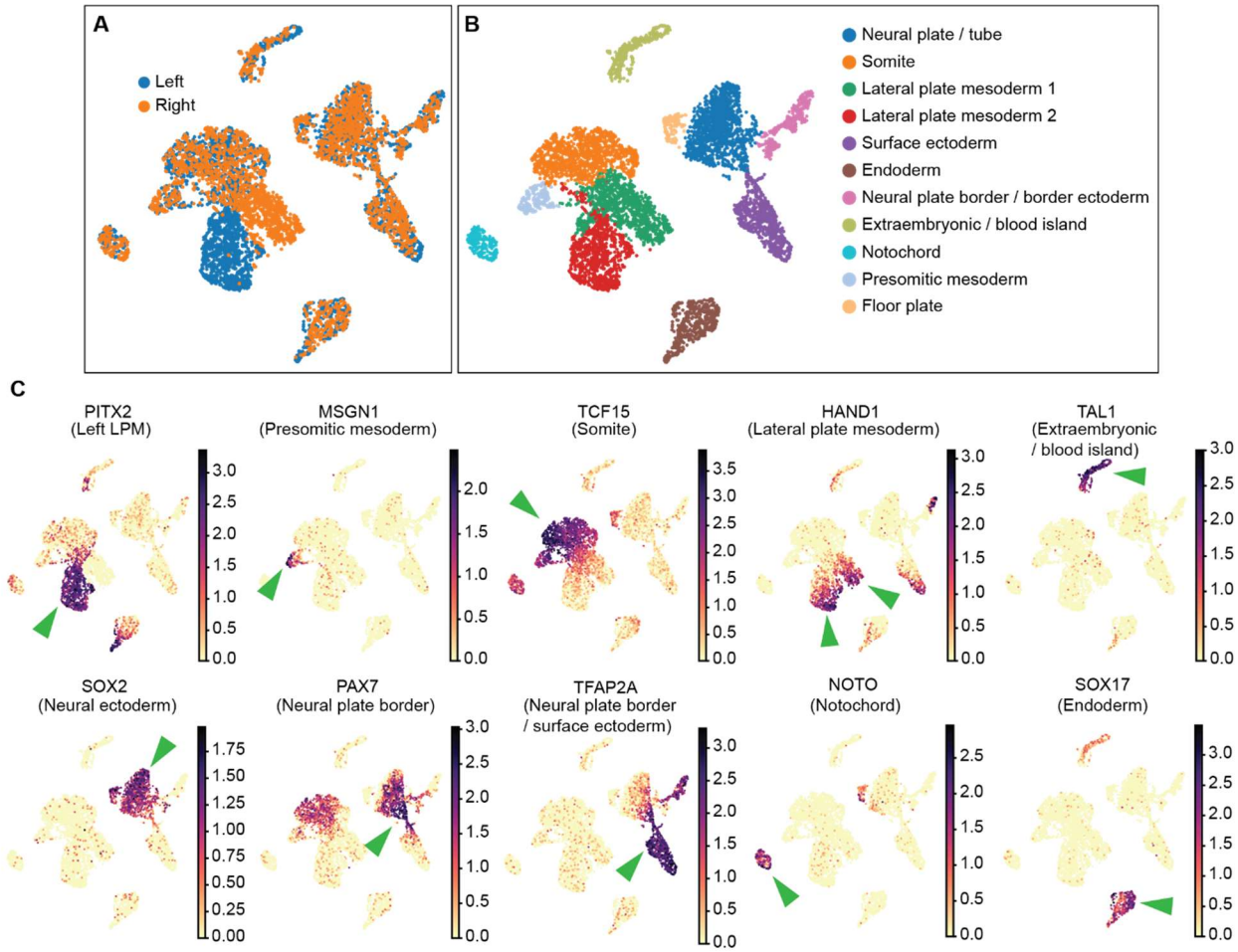

Figure 3.3. (A) UMAP of ZZ cells displays a region with clear separation by side. (B) Cluster assignment of ZZ cells. (C) Expression patterns of markers for different tissues. Green arrowheads indicate cells with elevated marker expression that informed assignment of cluster identity.

Identification and validation of novel asymmetric genes

As only the mesoderm cells demonstrated clear separation by side, we decided to focus on the LR asymmetry of mesoderm cells by subsetting and further clustering these cells (**Fig.3.4A**). We assigned mesoderm clusters, based on the expression of *PCDH8* (PSM), *TCF15* and *PAX3* (somite), and *HAND1/2* and *ISL1* (LPM) (**Fig.3.4B**). In addition, the left lateral somite cells expressing both *MEOX1* and *NODAL* lie at the interface of somite and LPM cells (**Fig.3.1A,3.4.A,C**). Therefore, we reasoned that the cells expressing both *MEOX1* and *NODAL*

between somite and LPM cells on the UMAP would represent the “left lateral somite” (**Fig.3.4C**), with the corresponding right counterparts representing the “right lateral somite”. We validated that side-specific clusters (left and right LPM; left and right lateral somite) consisted predominantly of the cells of one side, whereas the non-side-specific clusters (PSM, somite) exhibited a nearly 50:50 distribution (**Fig.3.4D**). The left and right lateral somite cells demonstrated “mixed” identity, with slightly lower levels of somite markers compared to the non-side-specific somite cluster and elevated levels of LPM markers (**Fig.3.4B**).

Figure 3.4. ZZ mesoderm subset and its cluster annotation

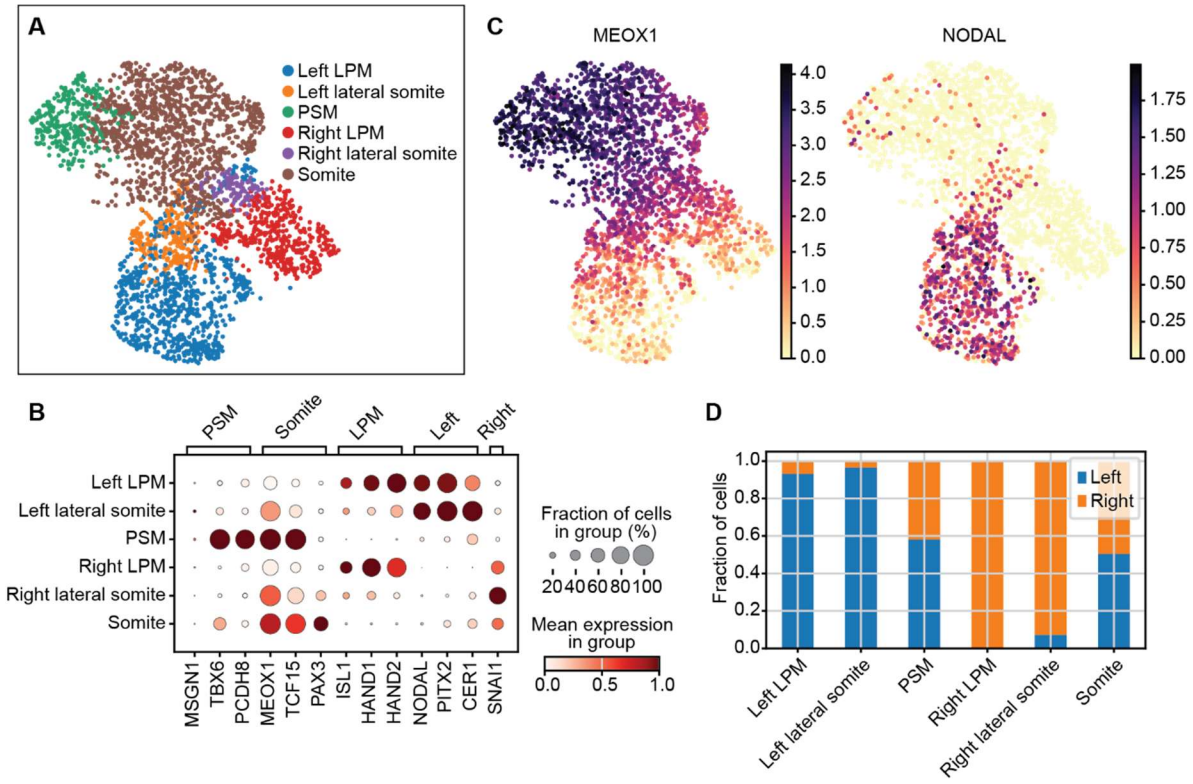

Figure 3.4. (A) Clusters of the ZZ mesoderm subset. (B) Validation of ZZ mesoderm clusters by the expression profiles of tissue-specific marker genes. *PCDH8* (PSM), *TCF15* and *PAX3* (somite), and *HAND1/2* and *ISL1* (LPM) were utilized to assign clusters. (C) The cells co-expressing *MEOX1* and *NODAL* were assigned to the left lateral somite cluster. Cells with the corresponding marker expression profile on the right side were assigned to the right lateral somite cluster. (D) Clusters were further validated by the fraction of cells belonging to the left and right sides, such that the side-specific clusters were predominantly composed of cells from a given side.

To validate these clusters, we performed differential gene expression analysis between the left and right lateral somite clusters and selected a few novel asymmetric genes for HCR RNA-FISH: *SLIT1* and *CHST11* for the left, and *DLX2* and *TCF21* for the right (**Fig.3.5A-D**). Indeed, HCR RNA-FISH for these genes in HH8 chick embryos displayed clear LR asymmetric expression at the lateral parts of occipital somites at HH8 (4-6 somite stage). Interestingly, at HH8, these genes were asymmetrically expressed in distinct tissue combinations. For example, *SLIT1* and *TCF21* were shown to be asymmetrically expressed in the lateral somite and LPM (**Fig.3.5A',D'**). On the other hand, *CHST11* asymmetry was pronounced in the lateral somite and the posterior halves of newly forming somites (**Fig.3.5B'**). One of the novel right-enriched genes *DLX2* exhibited highly specific expression in the right lateral somite, providing strong evidence for the cluster assignment (**Fig.3.5C'**). When we performed HCR RNA-FISH for *SLIT1* and *CHST11* in HH10 chick embryos to evaluate how long this newly discovered molecular asymmetry persists, both *SLIT1* and *CHST11* demonstrated lasting asymmetric expression on the left paraxial mesoderm (**Fig.3.5A",B"**).

To identify tissue-specific asymmetric genes, differential gene expression analyses were performed between left and right cells of the subsets representing the PSM, LPM, somite, and lateral somite. Using adjusted p-value = 0.05 and log-2-fold-change = 0.58 (1.5-fold) as thresholds, the analyses identified the largest number of asymmetric genes in the LPM subset (231 left-enriched genes vs. 244 right-enriched genes). Lateral somite cells displayed a comparable number of asymmetric genes (120 left vs. 200 right). Heatmaps of the top 20 asymmetric genes (20 left-enriched and 20 right-enriched) for each of the LPM and lateral somite subsets are shown for comparison (**Fig.3.5E**). On the other hand, only a few genes were identified as asymmetrically expressed in the somite cells (21 left vs. 8 right) and PSM cells (9

left vs. 1 right), consistent with the traditional expectation for the LR determination process. For instance, *BOLA3* (involved in mitochondrial of iron-sulfur cluster biogenesis (20,21)), *CER1* (a BMP antagonist involved in NODAL induction in the LPM (9,22)), *CHST11 (*involved in the regulation of sulfate chondroitin proteoglycans (23)*)*, *CXCL12* (a signaling factor broadly involved in development and physiology (24)), *NODAL*, *IDH2* (a mitochondrial NADP-dependent isocitrate dehydrogenase involved in metabolism and redox homeostasis (25)), *LDLRAD4* (a negative regulator of TGF-β signaling (26)), *MFAP2* (involved in the formation of microfibrils in the extracellular matrix (27)), *PITX2*, *SLIT1* (a signaling factor of the Slit-Robo pathway involved in axon guidance and cell migration (28)), and *WFIKKN1* (a secreted factor involved in the regulation of TGF-β signaling (29,30)) are consistently left-enriched in the LPM, lateral somite, and somite clusters (**Fig.3.5F**); on the other hand, *ESYT1* (a endoplasmic reticulum (ER) membrane protein involved in ER-plasma membrane tethering and lipid transfer (31)), *ID3* (a negative regulator of basic Helix-loop-Helix transcription factors (32)), and *SNAI1* (a transcription factor involved in epithelial-mesenchymal transition and cell motility (33,34)) are consistently right-enriched across the same clusters (**Fig.3.5G)**. These lists include well-known canonical asymmetric genes such as *NODAL*, *PITX2*, and *SNAI1* as well as multiple novel asymmetric genes. As such, our analysis of single-cell RNA sequencing provides a resource for identifying promising candidates for novel effectors of LR asymmetric development.

Next, we decided to apply the same logic for identifying left-right asymmetric genes to the non-mesoderm clusters: endoderm, neural plate/tube, surface ectoderm, neural plate border, and floor plate. The differential gene expression analysis with the same threshold (log-2-fold-change > 0.58; adjusted p-value > 0.05) identified fewer asymmetric genes in each cluster,

compared to the LPM and lateral somite clusters. For instance, the analyses identified 11 left and 13 right asymmetric genes for the endoderm; 14 left and 4 right for the neural plate/tube; 12 left and 5 right for the surface ectoderm; 5 left and 4 right for the neural plate border; and 8 left and 2 right for the floor plate. Among the left-enriched genes, *BOLA3* was the only gene significantly asymmetric in all five clusters, followed by *IDH2* in four clusters except for the floor plate; and by *CCT3*, *PITX2*, *ENSGALG00010028735*, and *MFAP2* in different sets of three clusters. Among the right-enriched genes, *ESYT1* was the only gene significantly asymmetric in all five clusters. The other 23 genes that were shown to be right-enriched in any of these clusters were significantly right-enriched in only one of the five clusters.

Figure 3.5. Differential gene expression analysis of the ZZ mesoderm clusters identifies novel asymmetric genes

Figure 3.5. (A) A novel left-enriched gene *SLIT1*, identified by the differential gene expression analysis of the left and right lateral somite clusters, (A') displays asymmetric *SLIT1* expression by HCR RNA-FISH in the LPM and the lateral parts of the anterior somites of the HH8 chick embryo. (A") The asymmetric expression of *SLIT1* persists in the LPM and lateral somites as late as HH10. (B) A novel left-enriched gene *CHST11* is asymmetrically expressed in the lateral parts of the anterior somites and the caudal parts of newly forming somites (B'), and asymmetric expression in the latter persists as late as HH10 (B"). (C) A novel right-enriched gene *DLX2* demonstrates relatively specific expression at the right lateral somite cluster. (C') A HH8 embryo labeled with HCR RNA-FISH for *DLX2* shows clear asymmetric expression in the lateral parts of the right anterior somites. (D,D') A novel right-enriched gene *TCF21* is asymmetrically expressed in the lateral parts of the anterior somites and the LPM. Blue and orange arrowheads indicate approximate positions of the left and right lateral somite clusters, respectively. (E) Heatmap of the top 20 left- and right-enriched genes for the LPM (left panel) and lateral somite (right panel) clusters. (F) Venn diagram of left-enriched genes in the LPM, lateral somite, and somite clusters. Eleven genes are consistently left-enriched in all three tissue types. (G) Venn diagram of right-enriched genes in the LPM, lateral somite, and somite clusters. Three genes are consistently right-enriched in all three tissue types. The novel asymmetric genes used for the validation of differential gene expression analysis via HCR RNA-FISH of (A-D) are written in red. Scale bar = 100μm

Figure 3.5. (continued)

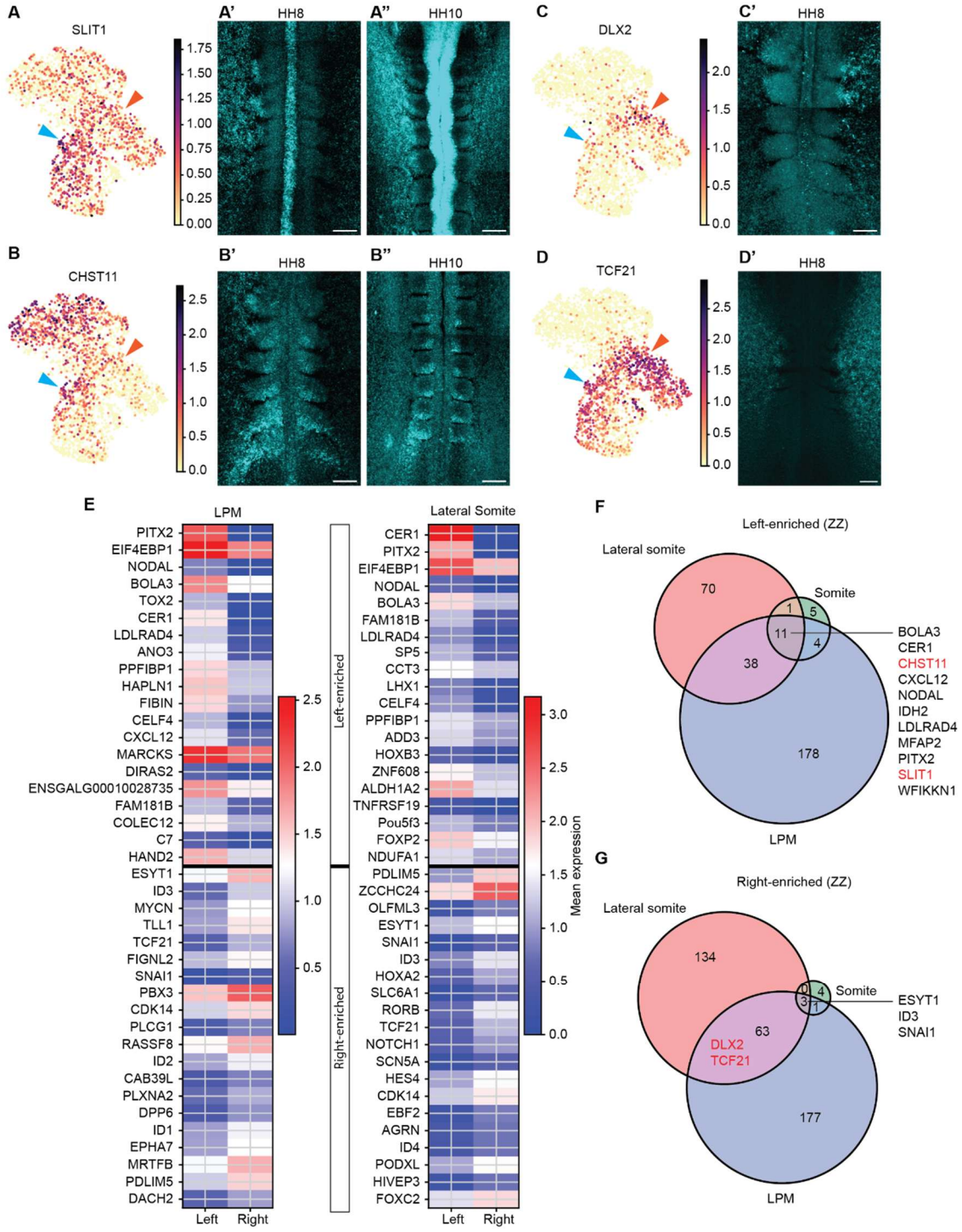

Lastly, our findings from the ZZ sample were validated in the ZW mesoderm subset (**Fig.3.6A)**. Just as with ZZ cells, the cells expressing both *MEOX1* and *NODAL* were assigned to the "left lateral somite" cluster, with the right counterpart assigned to the "right lateral somite" cluster (**Fig.3.6B)**. These lateral somite clusters and left and right LPM clusters (determined by *HAND1/2* and *ISL1*) were predominantly composed of cells of a given side; conversely, the somite cluster (determined by *TCF15* and *PAX3*) and the PSM cluster (determined by *PCDH8*), as well as an unknown mesoderm cluster, included a nearly 50/50 mix of left and right cells (**Fig.3.6C,D)**. The asymmetric genes identified in the ZZ sample and validated by HCR RNA-FISH—*SLIT1* and *CHST11* for the left and *DLX2* and *TCF21* for the right—consistently demonstrated asymmetric expression on the UMAP of the ZW mesoderm subset (**Fig.3.6E)**. The tissue-specific differential gene expression analyses of left versus right cells identified comparable numbers of asymmetric genes for each tissue as in the ZZ sample (**Fig.3.6F)**. Importantly, most of the genes that were consistently asymmetric in the LPM, lateral somite, and somite clusters of the ZZ sample were also robustly asymmetric in the ZW sample (**Fig.3.6F-blue text)**. The agreement between ZZ and ZW samples further reinforces the robustness and validity of our analysis underlying the discovery of novel molecular asymmetry.

Figure 3.6. Validation of novel asymmetric genes with ZW mesoderm subset

Figure 3.6. (A) UMAP of the ZW mesoderm. (B) Clusters of the ZW mesoderm. The same logic demonstrated for the ZZ mesoderm analysis above was applied. (C) Validation of clusters by left-right cell fraction. (D) Validation of clusters by tissue-specific marker expression profiles. (E) The novel asymmetric genes discovered in the ZZ mesoderm are consistently asymmetric in the ZW mesoderm. Blue and orange arrowheads indicate approximate positions of the left and right lateral somite clusters, respectively. (F) Venn diagrams of left-enriched (top panel) and right-enriched (bottom panel) genes in the LPM, lateral somite, and somite clusters. The novel asymmetric genes whose asymmetry is demonstrated with HCR RNA-FISH are written in red. Genes that were consistently asymmetric in the LPM, lateral somite, and somite clusters of the ZZ mesoderm are written in blue.

Figure 3.6. (continued)

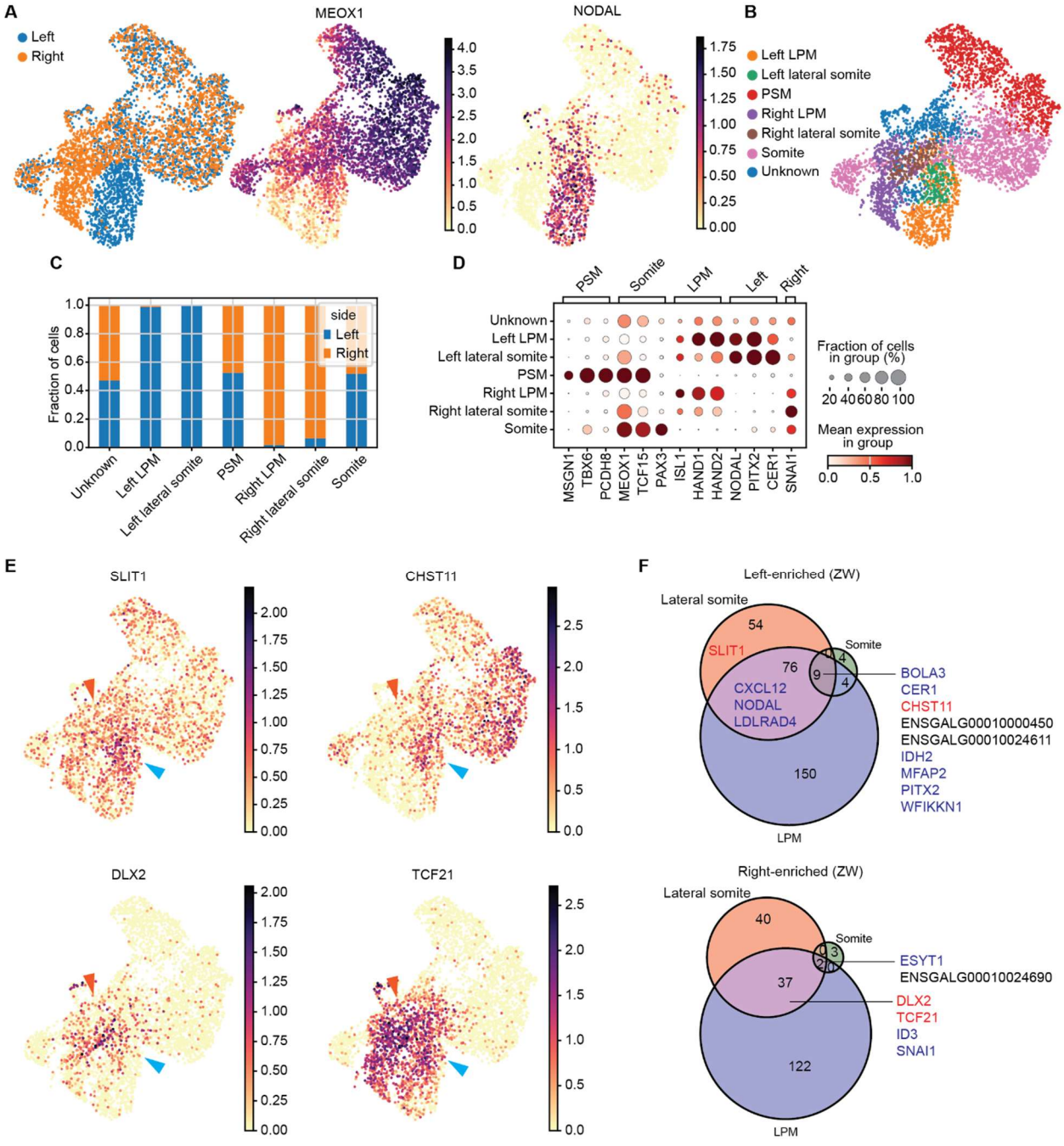

Potential non-autonomous role for somite molecular asymmetry in NC development

SLIT1 is one of the newly discovered asymmetric genes whose function is best characterized in the context of neural crest (NC) cell migration and axon guidance (**Fig.3.5A)** (28). When the early LR determination was perturbed at HH4 by either global treatment with cyclopamine (100μM; to inhibit Sonic Hedgehog signaling and prevent left-sided NODAL expression) or by implantation of a SAG bead on the right side of the HN (200μM; a Hedgehog pathway agonist, to induce ectopic right-sided NODAL expression), the asymmetric expression of *SLIT1* at HH9-10 was abolished, showing that *SLIT1* asymmetry is downstream of the early LR determination pathway (**Fig.3.7A)**. When *SLIT1* remained asymmetrically expressed at HH10 (10-12-somite stage), CNCCs begin to migrate out of the midline, through the asymmetric anterior somites (**Fig.3.7B)** (35,36). In addition to *SLIT1*, various genes involved in NC migrations were also found to be asymmetrically expressed by the lateral somite cells, including genes belonging to the Semaphorin (*SEMA5B*, *SEMA3A*), Plexin (*PLXNB2*), CXCL (*CXCL12*), Netrin (*UNC5C*), Slit-Robo (*SLIT1*, *ROBO2*), and Ephrin-Eph (*EFNB2*, *EFNB1*) signaling pathways (**Fig.3.7C)** (36–38).

To explore the potential function of this novel molecular asymmetry of somites, we hypothesized that the molecular asymmetry of the lateral somite impacts CNCC migration. To test this hypothesis, we evaluated asymmetry in CNCC migration in wild-type HH10 chick embryos by segmenting and comparing SOX9 immunostaining signals from migratory NC cells on the left and right sides beyond the neural tube (NT) domain (**Fig.3.7D)**. CNCC migration is highly temporally coordinated, such that at the 11-somite stage, CNCCs were only sparsely observed beyond the NT, whereas at the 12-somite stage, they had extended into the somite domain. CNCC migration determined by SOX9 segmentation beyond the NT was symmetric at

the 11-somite stage (**Fig.3.7E)**. Strikingly, by the 12-somite stage, however, a greater amount of SOX9+ signal was detected on the left side, demonstrating a left-bias in NC development (**Fig.3.7E)**. When we treated embryos with either a SAG bead or cyclopamine at HH4 to perturb early LR determination and incubated the treated embryos until the 12-somite stage, CNCC migration at the 12-somite stage became more symmetric (**Fig.3.7F)**. The modulation of CNCC asymmetry here cannot be specifically attributed to the novel molecular asymmetry of the anterior somites as the treatment perturbs LR determination across all tissues. Yet, considering that various genes associated with NC migration are asymmetrically expressed by somites and that the analyses were performed when CNCCs were migrating through these asymmetric somites, these results argue for the potential non-autonomous role of the molecular asymmetry of the occipital somites in regulating LR asymmetric development of adjacent tissue types.

Figure 3.7. Molecular asymmetry of the anterior somites may contribute to asymmetric cardiac neural crest cell migration

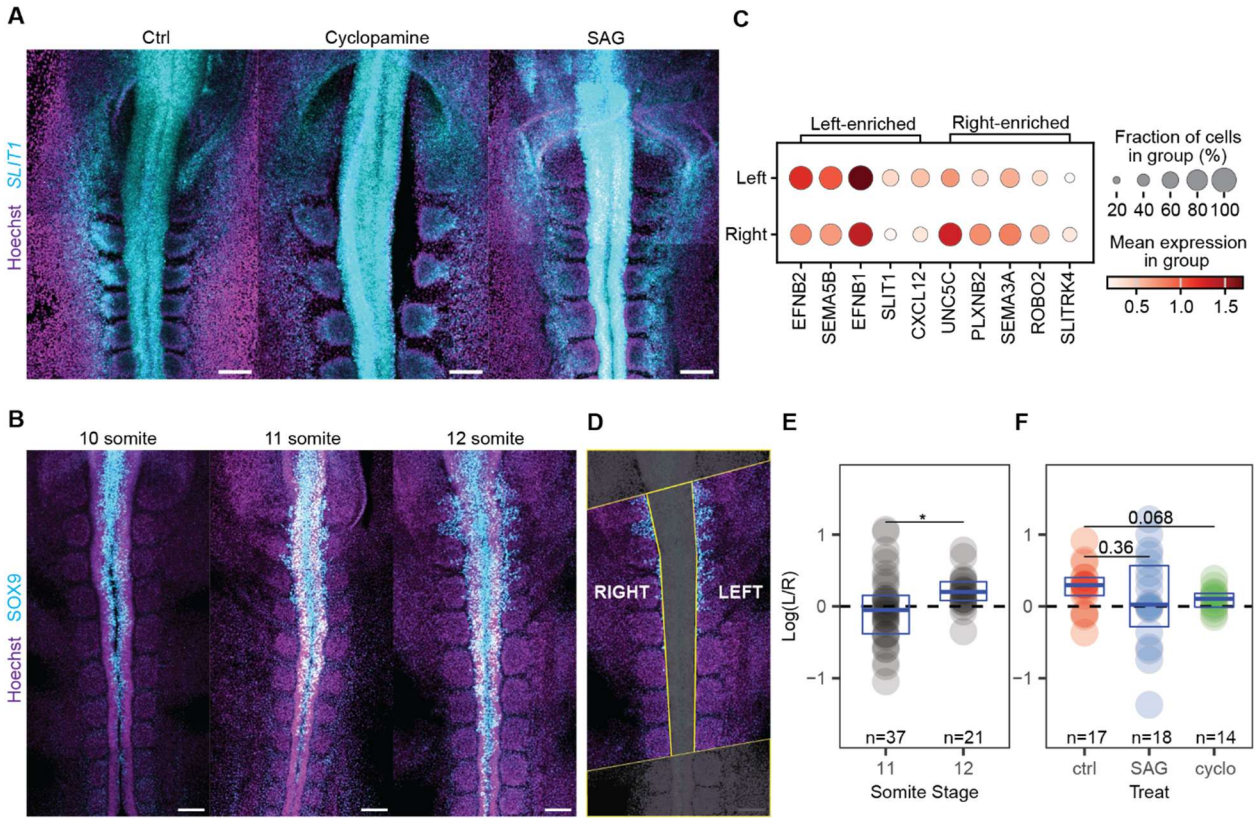

Figure 3.7. (A) Asymmetric expression of *SLIT1* at HH9-10 was abolished when chick embryos at HH4 were treated with either cyclopamine (100µM) or a SAG bead on the right side of the HN (200µM). Treated embryos were labeled with HCR RNA-FISH for *SLIT*1. (B) Migration of cardiac neural crest cells (CNCCs) in a HH10 chick embryo labeled with immunostaining for SOX9. CNCCs are confined within the closed neural tube by the 10-somite stage. Soon afterward, they emigrate from the neural tube and pass through the anterior somites at the 11- to 12-somite stages. (C) Multiple genes associated with NC migration were identified as asymmetrically expressed by differential gene expression analysis of the ZZ lateral somite clusters. (D) Schematic of CNCC migration asymmetry quantification. (E) CNCC migration is symmetric at the 11-somite stage but becomes left-biased at the 12-somite stage. (F) CNCC migration at the 12-somite stage is more symmetric upon either global treatment with cyclopamine (100µM) or implantation of a SAG bead on the right side of the HN (200µM) at HH4. Statistics are unpaired two-sided t-test. * is $p < 0.05$. Scale bar = 100µm

Anterior somites contribute to the heart

To further investigate the developmental consequences of their molecular asymmetry, we decided to revisit the fate map of anterior somites in a side-specific manner (39,40). To this end, we performed GFP somite graft experiments in chick embryo (41). The 2^{nd} to 5^{th} somites from transgenic donor embryos at the 5-7-somite stage ubiquitously expressing GFP were grafted orthotopically into non-fluorescent wildtype host embryos at the same stage (**Fig.3.8A,B)**. Embryos were incubated in ovo for 7 days until HH25-34, and the fate map was analyzed by 3D imaging with light sheet microscopy after tissue clearing and anti-GFP immunostaining.

At HH16, 2 days post-grafting, GFP-positive cells were predominantly localized in the dermomyotome, as confirmed by PAX7 immunostaining, and were absent from the neural tube (**Fig.3.8C,S1A)**. Only a few SOX9-GFP-double-positive cells were observed, suggesting that the donor graft contributed only minimally to the sclerotome. This was potentially because the ventral parts of the endogenous host somites could not be completely removed without risking puncture of the embryo, thereby limiting proper sclerotome differentiation of the ventral part of the donor somites. Importantly, at the time of grafting (5-7-somite stage), NC cells had not yet emigrated from the neural tube at the anterior somite levels, as attested by the restriction of SOX9 expression to the closed neural tube (**Fig.3.7B)**. NC emigration was first detected at the 11-somite stage as described earlier (35,36). At Day7, GFP-positive cells labeled known somite-derived structures, including the cervical dermis, the larynx, and the tongue (**Fig.3.8D-F)**, consistent with the previously described fate map of occipital somites (39,40). However, GFP-positive cells were not detected at the caudal parts of the skull or in the atlas and axis, which respectively derive from 1^{st}-5^{th} somites and 5-6^{th} somites.

The heart is widely known to undergo LR asymmetric organogenesis, and the heart forming region in the chick embryo is directly adjacent to the NODAL-expressing anterior somites (42,43). Strikingly, we detected a robust contribution of GFP-positive cells to the heart for both left and right grafts. When left somites were grafted (n=10), GFP-positive cells were robustly detected in the left sinus venosus (10/10, 100%) and frequently in the pulmonary artery (8/10, 80%) (**Fig. 3.8K–N**). In contrast, when right somites were grafted (n=8), GFP-positive cells were consistently found in the right sinus venosus (8/8, 100%), but only rarely in the pulmonary artery (1/8, 13%) (**Fig. 3.8G–J**). Together, these results show that contribution to the pulmonary artery was asymmetric, with a strong bias toward left somites.

To confirm these findings, we performed in ovo electroporation on 5-9-somite stage embryos (**Fig.3.8O)**. We injected a cocktail of membrane-bound-dTomato-expressing plasmid (mem-dTomato) flanked by Tol2 sequences and a plasmid containing a transposase into the somitocoel of a single anterior somite (44). Upon electroporation, the mem-dTomato sequence is randomly incorporated into the genome, so that the electroporated cells and their descendants display a permanent red fluorescent signal. The embryos were electroporated to specifically target the lateral side of the injected somite. Electroporation of the second left somite resulted in mem-dTomato labeling of the pulmonary artery in 6/10 (60%) embryos and of the sinus venosus in 6/10 embryos (60%) (**Fig.3.S2A-D)**. Electroporation of the third left somite yielded mem-dTomato signal in the pulmonary artery in 3/4 (75%) embryos and in the sinus venosus in 2/4 (50%) embryos (**Fig.3.8P-R)**. Electroporation of the fourth left somite resulted in no signal in the pulmonary artery (0/7) and only rare labeling in the sinus venosus (1/7, 14%) (**Fig.3.S2E-H).** These results independently validate the somite-to-heart contribution identified by grafting and indicate that this contribution arises predominantly from the 2nd and 3rd somites.

To characterize the identity of somite-derived cardiac cells, we performed co-immunostaining on grafted hearts upon paraffin sectioning. In the pulmonary artery, GFP-positive cells co-expressed the epicardial marker cytokeratin (CK555), consistent with an epicardial identity (**Fig.3.8S)**. In the sinus venosus, GFP-positive cells did not co-express smooth muscle actin (SMA) but were localized to the innermost single-cell layer, consistent with an endothelial identity (**Fig.3.8T)**.

Taken together, these results demonstrate that anterior somites contribute cells to the heart in a lateralized manner: they make a bilateral contribution to the endothelium of the ipsilateral sinus venosus, and an asymmetric, left-specific contribution to the epicardium of the pulmonary artery.

Figure 3.8. Anterior somites contribute to the heart in a lateralized manner

Figure 3.8. (A) Scheme of the side-specific GFP-somite graft experiment. The 2^{nd}-5^{th} somites of a transgenic GFP-expressing chick embryo at the 5- to 7-somite stage were grafted orthotopically into a wildtype host at the same stage. Grafted embryos were incubated for 7 days. Depending on survival, grafted embryos at HH25-34 were collected for analysis (*earliest stage for analysis). (B) A HH8 embryo right after grafting of a strip of GFP somites. (C) At HH16, 2 days after grafting, GFP+ cells were predominantly found in the dermomyotome (scale bar = 100μm). (D) 3D light sheet image of a grafted embryo after 7 days of incubation. Collected embryos were labeled with immunostaining for GFP and cleared with iDISCO+ (scale bar = 1000μm). GFP+ cells were found in the muscles of the (E) esophagus and larynx, and (F) tongue. (G) Upon right somite graft, (H,I) GFP+ cells were robustly detected in the right sinus venosus, (J) while they were only rarely observed in the pulmonary artery. (K) Upon left somite graft, (L-N) GFP+ cells were consistently detected in the left sinus venosus and the pulmonary artery. (O) Parallel validation by electroporation of a membrane-bound-dTomato-expressing plasmid (mem-dTomato) and transposase-expressing plasmid. (P-R) When the plasmid cocktail was injected into the somitocoel of the left 3^{rd} somite at the 5- to 9-somite stage and electroporated specifically on the lateral side, mem-dTomato-expressing cells were observed at the left sinus venosus and pulmonary artery (scale bar = 500μm). (S,T) An embryo with a left somite graft was paraffin-sectioned, and co-immunostaining was performed. (S) Left somite grafts likely contribute to endothelial cells of the left sinus venosus and (T) to epicardial cells of the pulmonary artery (CK+). Left somite grafts likely contribute to endothelial cells of the left sinus venosus and (S) to epicardial cells of the pulmonary artery (scale bar = 30 μm). **Abbreviations:** RA, right atrium; LA, left atrium; RV, right ventricle; LV, left ventricle; SV, sinus venosus (rSV, lSV); Ao, aorta; PA, pulmonary artery; DM, dermomyotome; NT, neural tube; Oe, oesophagus; La, larynx; To, tongue; αSMA, alpha-smooth muscle actin; CK, cytokeratin.

Figure 3.8. (continued)

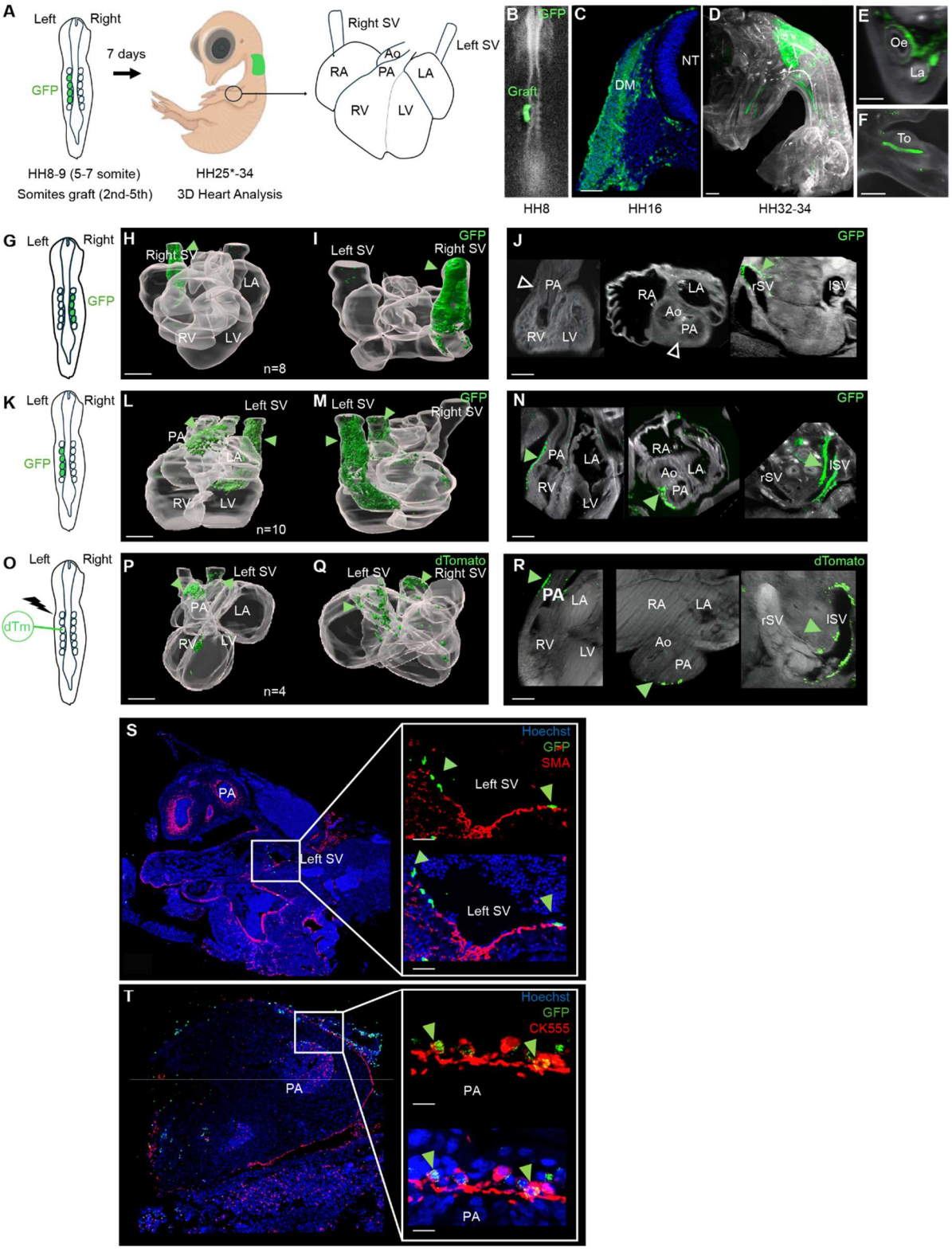

Left-right identity of somites impacts cardiac development

Given the lateralized contribution of somites to the heart, we asked whether the left–right identity of somites influences heart development. To address this question, we modulated the laterality of somite donor embryos before grafting. Donor GFP embryos were treated at HH4 with cyclopamine (to inhibit Sonic Hedgehog signaling and prevent left-sided Nodal expression) or with implantation of a SAG bead on the right side of the HN (a Hedgehog pathway agonist, to induce ectopic right-sided Nodal expression). Treated somites (2^{nd}–5^{th}) were then grafted into wildtype host embryos at HH8, and hearts were analyzed at HH25–34 (**Fig.3.9A**).

Impairment of left identity. When left somites from cyclopamine-treated donors were grafted (n=5), GFP signal was detected in the sinus venosus in 5/5 (100%) embryos but in the pulmonary artery in only 2/5 (40%), compared with 8/10 (80%) in controls (**Fig.3.9B-E**). Cardiac anatomy was severely affected: 4/5 embryos (80%) displayed congenital heart defects, compared with 1/10 controls (10%). These included ventricular malformations (3/5), such as ventricular hypoplasia and abnormal ventricular cavities, and outflow tract defects (3/5), including an outlet ventricular septal defect, persistent truncus arteriosus, severe subaortic stenosis, and an aorta overriding the right ventricle (**Fig.3.9F-I**; **Table.3.1.**). Thus, the loss of left identity in somites resulted in a high rate of cardiac malformations, affecting both the ventricles and the outflow tract, indicating that left somite identity plays a critical role in cardiac morphogenesis.

Ectopic right-sided Nodal expression. When right somites from SAG-treated donors were grafted (n=5), GFP signal was detected in the sinus venosus in 5/5 embryos, as expected. Ectopic GFP signal was observed in the aorta in 5/5 embryos (100%), whereas GFP was detected in the pulmonary artery in only 1/8 control right-side grafts (13%) (**Fig.3.9J-M**). This suggests that conferring left identity to right somites redirects their vascular contribution toward the aorta,

mirroring the left-sided contribution to the pulmonary artery. Cardiac malformations were observed in 2/5 embryos (40%), consisting exclusively of ventricular defects, predominantly right ventricular hypoplasia (**Fig.3.9N-O**; **Table.3.1.**). No outflow tract defects were detected.

Control experiments. To confirm the specificity of these effects, we performed reciprocal control experiments. Cyclopamine-treated right somites grafted to the right side (n=3) showed a GFP distribution and cardiac anatomy that were indistinguishable from those of untreated right-side grafts: signal in the right sinus venosus (3/3), minimal pulmonary artery signal (1/3), and no cardiac defects (0/3) (**Fig.3.S3A-F**). Similarly, SAG-treated left somites grafted to the left side (n=3) recapitulated untreated left-side grafts: signal in the left sinus venosus (3/3) and the pulmonary artery (2/3), with no cardiac malformations (0/3) (**Fig.3.S3G-L**; **Table.3.1.**). These controls demonstrate that cardiac defects arise specifically from modulation of the molecular laterality of the grafted somites, rather than from unintended effects of pharmacological treatment.

Figure 3.9. Molecular laterality of the anterior somites is critical for fate contribution and proper heart development

Figure 3.9. (A) Scheme of modulating the molecular laterality of somite grafts. GFP-expressing donor embryos were treated with either cyclopamine (100μM) or a SAG bead (200μM) at HH4 and incubated to the 5- to 7-somite stage for the graft experiment. (B,C) Untreated left grafts contributed to the left sinus venosus and the pulmonary artery. (D,E) Left grafts whose left identity was disrupted by cyclopamine treatment demonstrated compromised contribution to the pulmonary artery. In addition, cyclopamine-treated left grafts led to a high frequency of congenital heart defects (H,I), compared to untreated left grafts (F,G). (L,M,O) Right grafts with induced left identity by SAG bead treatment contributed to the right sinus venosus and the aorta, (J,K,N) whereas the untreated right graft contributed robustly to the right sinus venosus, with minimal contribution to the pulmonary artery. (P) Summary of the somite graft experiment with molecular laterality modulation. Scale bar = 500μm. Abbreviations: RA, right atrium; RV, right ventricle; LA, left atrium; LV, left ventricle; SV, sinus venosus; Ao, aorta; PA, pulmonary artery; CHD, congenital heart defect.

Figure 3.9. (continued)

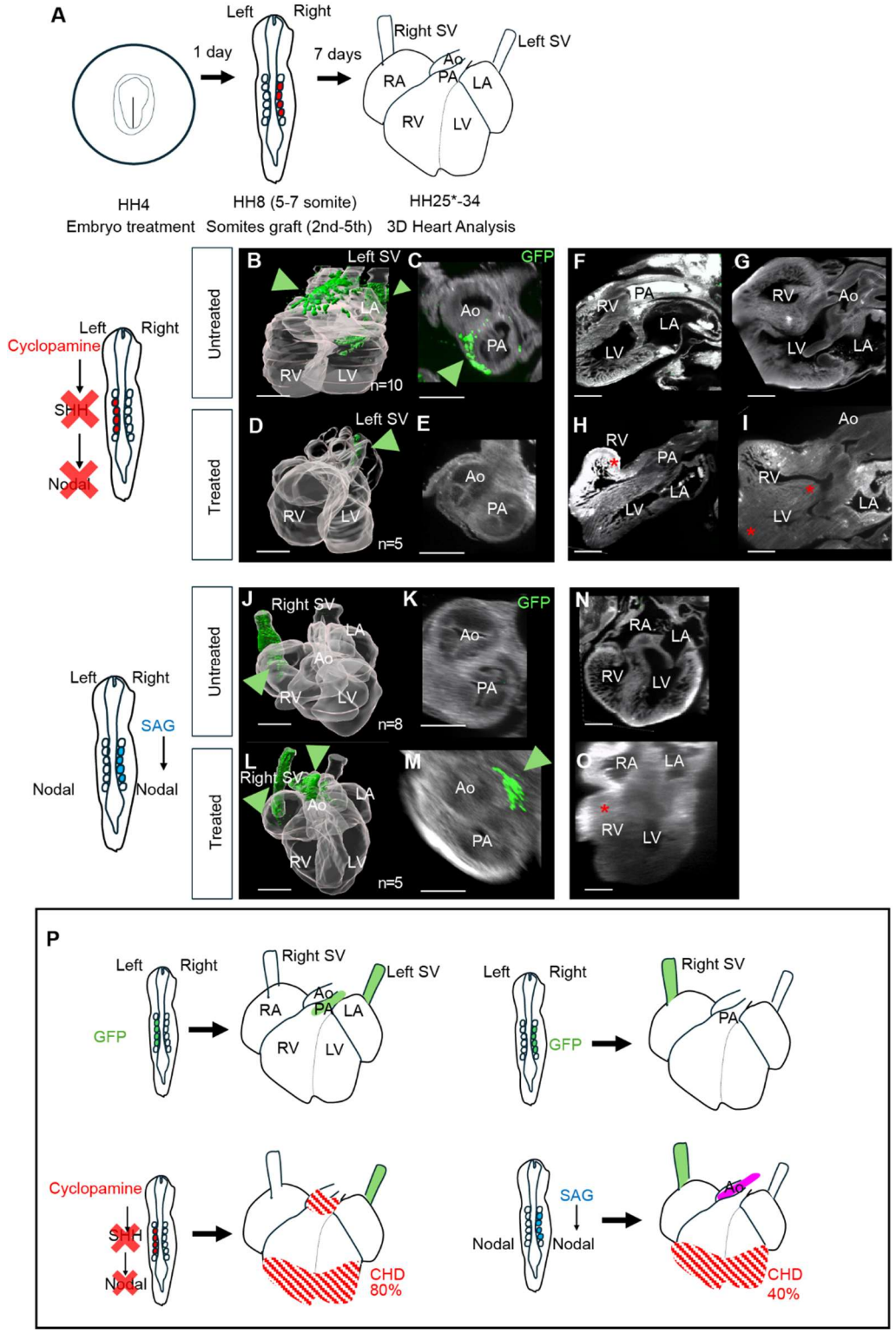

Table 3.1. Summary of GFP somite graft experiment

Experiment		GFP Signal Analysis							Summary
Sample ID	Final Stage	Sinus Venosus	Great Vessels	Ventricular Loop	Ventricular Malformation	VSD	AV Valve Defect	Outflow Tract / Great Arteries	Conclusion
WT Graft – Left Somites									
10010401	HH34-35	Left SV	PA	D-loop	No	No	No	Normal	**Normal**
10010301	HH30-31	Left SV	PA	D-loop	No	Ongoing septation (stage HH31)	No	Normal	**Normal for stage**
10010102	HH34	Left SV	PA	D-loop	No	No	No	Normal	**Normal**
10010202	HH35	Left SV	PA	D-loop	No	No	No	Normal	**Normal**
10010101	HH33	Left SV	PA	D-loop	No	No	No	Normal	**Normal**
11010105	HH34	Left SV	PA	D-loop	No	No	No	Normal	**Normal**
11010201	HH28	Left SV	PA	D-loop	No	Ongoing septation (stage HH31)	No	Ongoing aortic wedging (stage HH31)	**Normal for stage**
11010203	HH30	Left SV	PA	D-loop	No	Ongoing septation (stage HH31)	No	Ongoing aortic wedging (stage HH31)	**Normal for stage**
11010104	HH31-32	Left SV	No signal	D-loop	No	No	No	Normal	**Normal**
11010102	HH32-33	Left SV	No signal	D-loop	Abnormal ventricular cavities and trabeculation	Outlet VSD (subaortic)	AV canal defect	Aorta overriding RV	**Abnormal ventricles and great arteries**
WT Graft – Right Somites									
10020302	HH34	Right SV	No signal	D-loop	No	No	No	Normal	**Normal**
10020202	HH34	Right SV	No signal	D-loop	No	No	No	Normal	**Normal**
10020103	HH31	Right SV	No signal	D-loop	No	No	No	Normal	**Normal**
10020101	HH34	Right SV	No signal	D-loop	No	No	No	Normal	**Normal**
11020101	HH30-31	Right SV	No signal	D-loop	No	Ongoing septation (stage HH31)	No	Normal	**Normal for stage**

Table 3.1. (continued)

11020201	HH25	Right SV	No signal	D-loop	No	Ongoing septation (stage HH25)	Ongoing AV valve morphogenesis (stage HH25)	Ongoing aortic wedging (stage HH25)	**Normal for stage**
11020301	HH25	Left SV	No signal	D-loop	No	Ongoing septation (stage HH25)	No	Ongoing aortic wedging (stage HH25)	**Normal for stage**
11020302	HH33-34	Right SV	PA	D-loop	No	No	No	Normal	**Normal**
Cyclopamine – Left Somites									
11030101	HH34	Left SV	No signal	D-loop	Abnormal ventricular cavities (Small left ventricle)	Outlet VSD (subaortic)	No	Aorta overriding RV	**Outlet VSD + aorta overriding RV + small LV**
11030102	HH31	Left SV	No signal	D-loop	No	Ongoing septation (stage HH31)	Ongoing AV valve morphogenesis (stage HH31)	Ongoing aortic wedging (stage HH31)	**Normal for stage**
11030103	HH34	Left SV	PA	D-loop	Abnormal ventricular cavities (hypoplasia)	No	No	Normal	**Abnormal ventricles**
11030105	HH34	Left SV	No signal	D-loop	Abnormal ventricular cavities (major RV hypoplasia)	No	No	Severe subaortic stenosis	**Abnormal ventricles and great arteries**
11030201	HH30-31	Left SV	PA	D-loop	No	Ongoing septation (stage HH31)	Ongoing AV valve morphogenesis (stage HH31)	Persistent truncus arteriosus	**Abnormal great arteries (persistent truncus arteriosus)**
Cyclopamine – Right Somites									
11040103	HH30-31	Right SV	No signal	D-loop	No	No	No	Normal	**Normal for stage**
11040206	HH33-34	Right SV	No signal	D-loop	No	No	No (cushions still present)	Normal	**Normal**
11040208	HH33	Right SV	PA	D-loop	No	No	No	Normal	**Normal**

Table 3.1. (continued)

SAG – Right Somites									
11050301	HH34	Right SV	Aorta	D-loop	RV hypoplasia with abnormal ventricular morphology	No	No	Normal	**Abnormal ventricles**
11050201	HH33	Right SV	PA + Aorta	D-loop	No	No	No	Normal	**Normal**
11050202	HH31	Right SV	PA + Aorta	D-loop	No	No	No	Normal	**Normal**
11050101	HH34	Right SV	PA + Aorta	D-loop	RV hypoplasia	No	Tricuspid atresia	Normal	**Abnormal ventricles and tricuspid atresia**
11050303	HH33	Right SV	Aorta	D-loop	No	No	No	Normal	**Normal**
SAG – Left Somites									
11060101	HH29	Left SV	PA	D-loop	No	No	Ongoing AV valve morphogenesis (stage HH29)	Ongoing aortic wedging (stage HH31)	**Normal for stage**
11060201	HH34	Left SV	PA	D-loop	No	No	No (cushions still present)	Normal	**Normal**
11060202	HH28	Left SV	Outflow tract	D-loop	No	No	Ongoing AV valve morphogenesis (stage HH28)	Ongoing aortic wedging (stage HH28)	**Normal for stage**

DISCUSSION

LR asymmetry of the paraxial mesoderm and somites has long been overlooked, and, consequently, the potential developmental asymmetry of somites has not been carefully investigated. Our findings provide strong and direct evidence that anterior somites are molecularly asymmetric, especially at their lateral sides. Our side-specific single-cell RNA sequencing of the HH8 chick embryo is expected to be an invaluable resource for understanding the early molecular landscape during the early LR patterning process. As the efficacy of our approach has been validated above, a series of side-specific single-cell RNA sequencing experiments at later stages will be extremely useful in establishing a comprehensive picture of the signaling cascades and the downstream effectors underlying LR asymmetric development of the vertebrate embryo.

The occipital somites are known to exhibit a variety of distinguishing developmental properties, compared to trunk somites. First, the occipital somites do not express many of the widely recognized rostro-caudal polarity markers of somites. For instance, when the expression of several RC markers of somites—*delta1*, *notch1*, *hairy1*, *hey2*, *hairy2*, and *lunatic fringe*—was analyzed, the 1st to 3rd somites did not express any of these genes, while the 4th to 9th somites expressed only a subset of them, compared to somites at more caudal levels (13). Second, the occipital somites exhibit different maturation dynamics. The activation of markers for somite compartmentalization—*PAX1* for the sclerotome, and *MYOD1* for the dermomyotome—is not only much delayed but also simultaneous across occipital somites, whereas marker gene expression is much faster and sequential in trunk somites (14). The developmental dynamics of the myotome also demonstrate a similar pattern (15,16). These findings indicate that the differentiation trajectories of occipital somites are different from those of trunk somites, in that

the molecular maturation and compartmentalization of occipital somites are relatively delayed and/or lacking. This prolonged or reduced differentiation state may underlie the ability of occipital somites to respond to LR-determining signals.

The asymmetry in CNCC migration was evaluated as a potential, non-autonomous contribution of somite molecular asymmetry to the asymmetric development of the embryo. Two newly discovered left-enriched genes, *SLIT1* and *CHST11*, have been implicated in the regulation of NC migration. For instance, *CHST11* encodes an enzyme involved in regulating chondroitin sulfate proteoglycans, ECM components that act as a barrier to the migration of NC cells (23,45). Chondroitin sulfate proteoglycans have been shown to be necessary for confining migratory NC cells to the anterior half of the somite, as treatments that perturb their biosynthesis alter the NC migration pattern (45). It remains to be explored whether the elevated *CHST11* expression on the left side, especially in the caudal parts of newly forming somites, is translated into higher levels of chondroitin sulfate proteoglycans and into an asymmetric environment for NC migration dynamics. Our finding that CNCC migration is more pronounced on the left side at the 12-somite stage, however, contradicts the expected upregulation of chondroitin sulfate proteoglycans in the left somites. However, as our single-cell RNA sequencing identifies multiple asymmetric genes involved in NC migration, the combination of all these factors, each of which may not be unilaterally biased, can generate the overall left-bias in CNCC migration. In addition, our treatments perturbing LR determination affect the laterality of the entire embryo, not specifically that of the anterior somites. Thus, experiments specifically modulating the molecular laterality of somites will be needed to unequivocally determine whether somite molecular asymmetry plays a non-autonomous role in regulating CNCC migration asymmetry.

Interestingly, our results align with recent findings on the asymmetric contribution of CNCCs to heart development (46). It was shown that surgical ablation of left and right CNCCs led to different heart defect outcomes and survival rates. While our results posit a non-autonomous role for asymmetric somites in providing asymmetric fields for NC migration, it is possible that NCs are intrinsically asymmetric, just as somites are. Regardless, our findings, together with this recent finding of NC asymmetry, call for further investigation into the asymmetry of tissues beyond the LPM and endoderm.

Our results demonstrate that anterior somites are a previously unrecognized source of cardiac cells in the chick embryo, contributing endothelial cells to the sinus venosus bilaterally and epicardial cells to the pulmonary artery specifically from the left side. Modulation of somite laterality through pharmacological manipulation of the Hedgehog/Nodal pathway reveals that the left–right identity of somites is functionally relevant for both their cardiac contribution and for normal cardiac morphogenesis.

The cardiac and somitic lineages develop in close spatial and temporal proximity during early embryogenesis. In the chick at HH8 (4–6 somites), the anterior somites are directly adjacent to the cardiac mesoderm (42,43); in the mouse, equivalent proximity exists at E8.5 (47). The heart is one of the first organs to undergo left–right asymmetric morphogenesis, with the heart tube initiating rightward looping at this stage (48). Simultaneously, left–right patterning is established in the heart field through transient left-sided Nodal signaling, which biases cell behavior to control asymmetric heart tube remodeling (49). During heart looping, the venous pole undergoes a leftward shift (50), a process dependent on left–right patterning that takes place at the level of the anterior somites. Thus, two left–right patterned developmental processes,

cardiac looping and somitogenesis, are occurring at the same time and place, raising the possibility of functional interactions between them.

The mammalian heart is built from multiple cell lineages with distinct developmental origins, progressively characterized over the past decades (47,51,52). The myocardium and endocardium derive from two successive waves of progenitors: the first heart field, which forms the initial heart tube and gives rise primarily to the left ventricle, and the second heart field, a population of progenitors in the dorsal pericardial wall and pharyngeal mesoderm that is progressively added to both poles of the heart tube, contributing to the right ventricle, outflow tract, and atria (47,51). The epicardium originates from the proepicardial organ, a transient mesothelial structure that emerges near the sinus venosus (53), and gives rise to smooth muscle cells, fibroblasts, and mesenchymal cells of the valves. Single-cell transcriptomic profiling has further refined this lineage map, revealing a common progenitor pool for the epicardium and myocardium at early stages (52). CNCCs, of ectodermal origin, contribute to the outflow tract septum, interventricular septum and coronary smooth muscle cells (54,55). Thus, the heart integrates cells from the lateral plate mesoderm (first and second heart fields, proepicardial organ) and the NC.

Our findings add anterior somites to this lineage map. Several lines of prior evidence support the plausibility of a somite-to-heart contribution. First, somites are known contributors to the trunk vasculature: the dermomyotome gives rise to endothelial cells, while the sclerotome produces vascular smooth muscle cells and pericytes of the body wall, and smooth muscle cells of the dorsal aorta share a common clonal origin with skeletal muscle of the myotome (56,57). Second, mixed NC and somite contributions to the same structure have been documented in other contexts, such as the tongue musculature (58) and the branchiomeric muscles (59),

establishing a precedent for dual-origin tissues. Third, Meox1-Cre-based lineage tracing in the mouse (60), although designed to target somite derivatives, has reported labeling in the pulmonary artery and the epicardium. This observation, initially described as ectopic, is in fact consistent with our findings and supports a genuine somite contribution to the heart in mammals. Our identification of somite-derived endothelial cells in the sinus venosus and epicardial cells in the pulmonary artery extends this contribution from the trunk vasculature to the heart itself.

A striking feature of our findings is the left-specific contribution of somites to the pulmonary artery. Lateralized clonal relationships between cervical structures and cardiac regions have been demonstrated in mice: left facial muscles share a common progenitor with the pulmonary trunk, whereas right facial muscles derived from head mesoderm are clonally related to the aorta (61). Similarly, left-sided progenitors of the trapezius muscle group are clonally related to pulmonary trunk myocardium, while right-sided progenitors contribute to the right venous pole (62). Our results extend this principle to the somitic mesoderm: left somites contribute to the pulmonary artery, whereas right somites do not. Critically, our laterality reversal experiments demonstrate that this asymmetry is determined by left–right identity rather than anatomical position. When right somites are exposed to ectopic Nodal signaling (SAG bead treatment), they contribute to the aorta rather than the pulmonary artery, effectively acquiring a mirror pattern of the normal left-sided contribution. These observations indicate that the Nodal signaling cascade determines the specific vascular destination of somite-derived cells within the outflow tract.

A potential concern is that the grafted tissue could include NC cells. Several lines of evidence argue against this possibility. First, at the time of grafting (5- to 7-somite stage), NC cells had not yet emigrated from the neural tube at anterior axial levels, as demonstrated by the

restriction of SOX9 expression to the neural tube. NC emigration was not detected until the 11-somite stage. Second, NC contributions to the heart are primarily to the outflow tract septum and the interventricular septum not to the epicardium (39), which is where we detect somite-derived cells in the pulmonary artery. Third, isolated NC ablation produces conotruncal septation defects but not the ventricular malformations we observe upon cyclopamine treatment (46), suggesting that the ventricular phenotype reflects impairment of a distinct, somite-specific mechanism.

We cannot fully exclude minor contamination from the lateral plate mesoderm adjacent to the somites (42,43). However, any such contribution would be expected to predominantly affect the venous pole rather than the outflow tract. Moreover, parallel validation via an electroporation-based fate map further corroborates the contribution of the anterior somites to the heart, arguing against the possibility of LPM contaminants being a primary source of GFP-positive signals in the heart.

Our findings that somites contribute to the heart and that their laterality influences cardiac morphogenesis have potential clinical relevance. Congenital heart defects are frequently associated with vertebral anomalies in the context of VACTERL syndrome (63) and VCRL syndrome (64). The risk of developing scoliosis in children with congenital heart disease is more than ten-fold that of idiopathic scoliosis (65), suggesting a shared developmental etiology. Moreover, laterality defects further connect spine and heart: most idiopathic scoliosis cases display right convexity, whereas in patients with reversed organ laterality (situs inversus), scoliosis cases are predominantly left-convex (66). Our results suggest a developmental mechanism that could underlie these clinical associations: disruption of left–right signaling in somites may simultaneously impair both vertebral symmetry and cardiac morphogenesis, explaining the co-occurrence of spine and heart defects in these syndromes.

In summary, our work reveals extensive molecular asymmetry of the anterior somites and identifies anterior somites as a novel source of cardiac cells, with a lateralized contribution pattern that depends on Nodal signaling. Perturbation of somite laterality produces congenital heart defects, establishing a functional link between somite left–right identity and cardiac morphogenesis. These findings open new perspectives on the developmental origins of congenital heart defects and their association with vertebral anomalies.

METHODS

Chick embryos

Fertilized chick eggs were acquired from the Charles River Laboratories (for wildtype) and the Susan Chapman Laboratory of Clemson University (for wildtype and transgenic lines ubiquitously expressing GFP (41)). Eggs were incubated at 37°C and 60% humidity.

HCR RNA-FISH

HCR RNA-FISH for chick embryo was performed as described above. HCR probe sets were designed and manufactured by Molecular Instruments.

Chick embryo manipulation

Chick embryos were collected, cultured, and treated as described above.

Single-cell RNA sequencing

4-somite stage chick embryos were collected with ring-shaped filter papers. The embryos were first bisected along the midline. Next, for each side, dissection was performed to obtain the rectangular tissue of interest, which spanned from the first somite to the 30-50% level of the PSM in the AP direction, and from the midline to the border between the LPM and the extraembryonic tissue in the ML direction. Left and right samples were processed and sequenced separately. Tissue samples from the same 4 embryos were pooled for each side and incubated in 400µl of 0.25% Trypsin-EDTA (Gibco) at 37°C for 25min with mechanical dissociation by pipetting every 5min. Next, 600µl of ice-cold PBS supplemented with 1% bovine serum albumin

(Sigma-Aldrich; PBS-BSA) was added and centrifuged at 400rcf for 5min at room temperature. Supernatant was removed, and the cells were resuspended in 400µl of PBS-BSA to pass through 20µm cell strainer (Stellar Scientific). After initial passage, additional 400µl of PBS-BSA was applied to capture remaining cells. The cells were then centrifuged at 400rcf for 5min, and the supernatant was removed to resuspend cells with 80µl of PBS-BSA. Cell density was determined by manual counting. Cells were encapsulated with the Chromium Next GEM Single Cell 3' kit (v.3.1 Dual Index) with the Chromium NextGEM Chip and the 10x Chromium Controller (Biopolymers Facility, Harvard Medical School). Libraries were prepared following the manufacturer's protocol and sequenced on a NovaSeq 6000 S1 system. After sequencing, the libraries were aligned to the chicken genome (GRCg7b) with Cell Ranger (v7.1.0).

Analysis of single-cell RNA sequencing

The single-cell RNA sequencing data was analyzed with Scanpy (1.9.5), AnnData (0.10.2), Numpy (1.24.4), Pandas (2.1.1), SciPy (1.11.2), and Matplotlib (3.7.2) on Python (3.11.5). Left and right samples were merged, and cells with at least 1000 detected genes, and genes expressed by at least 3 cells were retained for analysis. Next, cells with greater than 15% mitochondrial transcripts or less than 10% ribosomal transcripts were excluded, based on the quality control distribution. Mitochondrial and ribosomal genes were then removed from downstream analysis. Predicted doublets were removed with Scrublet (0.2.3). Raw counts were normalized and log-transformed. Highly variable genes were identified from the log-normalized data, after which total counts and mitochondrial transcript percentage were regressed out, followed by data scaling and principal component analysis. Putative ZZ and ZW cells were separated using a threshold of 0.1 on the log-normalized expression of the W chromosome gene

HINTW. After separation, neighbors and UMAP (n_pcs=40, n_neighbors=8) were recomputed for each dataset. For the ZZ dataset, Leiden clustering was performed at resolutions of 0.2 for the full dataset and 1.5 for the mesoderm subset. Cluster identities were assigned based on the expression of known marker genes. In particular, clusters expressing both MEOX1 and NODAL and showing a left-cell bias were annotated as the left lateral somite cluster, whereas the corresponding contralateral clusters with a similar marker expression profile and a right-cell bias were annotated as the right lateral somite cluster. For the ZW dataset, Leiden clustering was performed at resolutions of 0.2 for the full dataset and 1.1 for the mesoderm subset. The same annotation logic was applied to the ZW dataset.

Analysis of cardiac neural crest cell migration asymmetry

Treated or untreated embryos at HH10 (10-12 somite stage) were fixed in 4% paraformaldehyde (PFA) for 1-2hr at room temperature or overnight at 4°C, washed three times in PBS with 0.5% Triton X-100 for 10min, and blocked with 5% donkey serum in PBS with 0.5% Triton X-100 for 2hr at room temperature. Embryos were incubated with a primary antibody solution (blocking solution with 1:500 rabbit anti-SOX9 (Chemicon, AB5535)) overnight at 4°C. Next, embryos were washed six times with PBS with 0.5% Triton X-100 for 10min at room temperature and incubated in a secondary antibody solution (blocking solution with 1:1000 donkey anti-rabbit Alexa Fluor 647 (Invitrogen, A-31573)) overnight at 4°C. The following day, embryos were washed six times with PBS with 0.5% Triton X-100 for 10min at room temperature. Hoechst33342 (Invitrogen) was added at 1:1000 in one of the final washes. The labeled embryos were imaged in Z stacks with an interval of 5μm using a Zeiss LSM880

confocal microscope (NeuroTechnology Studio, Brigham and Women's Hospital) and a Plan-Apochromat 20x/0.80 objective.

For a given batch of staining and imaging, a common threshold for segmentation of the SOX9 signal was determined. Next, left and right ROIs spanning from the first somite to the seventh somite in the AP direction and lateral to the outer wall of the neural tube facing the somites were manually drawn for slices showing SOX9-positive neural crest cells to capture NC migration beyond the midline. The threshold for a given imaging batch was applied to both left and right ROIs, and the sum of the areas of the remaining particles larger than 20μm2 was used to represent the amount of migratory neural crest cells on each side. Log(L/R) was calculated as a measure of asymmetry of neural crest cell migration.

For the experiments perturbing LR determination, treatments were performed as described above. Embryos were collected using the EC culture method and treated with either a global treatment with cyclopamine (100μM) or implantation of a SAG bead (200μM) at the right side of the HN at HH4 (67). Control embryos were treated with either vehicle-matched PBS or beads soaked in PBS. In parallel experiments, cyclopamine (100μM) altered the NODAL expression pattern in 51/51 embryos (100%), whereas SAG beads (200-500μM) did so in 50/65 embryos (77%). Therefore, SAG-bead-treated embryos were labeled with HCR RNA-FISH for PITX2 so that only embryos showing the predicted treatment outcome were included in the analysis.

Somite graft experiment

Wildtype and GFP-expressing chick embryos at 5-7 somite stage were used for grafting.

For a host, 2-3ml of clear albumen was removed, and the eggs were windowed in an orientation, in which the long axis was parallel to the ground. A few drops of PBS with calcium chloride and magnesium chloride (Sigma-Aldrich; PBS) supplemented with 1% penicillin-streptomycin (Gibco; 100units/ml Penicillin, 100µg/ml streptomycin) were applied to the embryo. A solution of 1% Fast Green (Sigma-Aldrich) diluted in PBS was injected into the yolk to visualize the embryo. After gently rupturing the vitelline membrane above the somites, endogenous somites (2nd-5th somites on the left or on the right) were removed in ovo. Briefly, longitudinal cuts were made along the apparent boundary between the somite and the neural tube and along the boundary between the somite and the lateral plate mesoderm. Transverse cuts were made at the anterior end of the 2nd somite and the posterior end of the 5th somite. Next, the endogenous somites were carefully removed using a custom-made scalpel and a mouth pipette with a pulled glass capillary, without puncturing the embryo.

For donor somites, GFP embryos were collected using the EC culture method, and, if needed, incubated additionally in vitro to reach the desired stages (67). Next, GFP embryos were washed in PBS, and placed ventral-up. Collagenase Type IV (Gibco) diluted in PBS to a final concentration of 2800units/ml was applied for 1min, followed by the application of a small volume of bovine serum albumin (Sigma-Aldrich) to stop collagenase activity. This treatment was used to remove the endoderm and the lateral plate mesoderm from the somites using a custom-made scalpel (In some early wildtype untreated graft experiments, the collagenase step was omitted, but no effect on somite fate contribution was detected.). Next, the embryo was excised from the filter paper and fixed with insect pins dorsal-up to dissect the strip of somites (2nd–5th) to be grafted. Similar longitudinal and transverse cuts to those used in the host preparation were made to dissect the somite strips. Dissection was performed ensuring that

midline tissue (e.g., neural tube and neural crest) was not included in the graft, and therefore the most medial parts of the somites were also excluded from the graft. The dissected graft was transferred to the host and positioned appropriately by removing liquid using a mouth pipette and a pulled glass capillary. The eggs were sealed with tape and incubated for 7 days at 37°C and 60% humidity.

For the graft experiments perturbing LR determination, treatments were performed as described above. Donor GFP embryos were collected using the EC culture method and treated with either a global treatment with cyclopamine (100μM) or implantation of SAG bead (200μM) in the right side of the HN at HH4. Treated embryos were incubated until they reached the 5-7-somite stage.

After incubation, grafted embryos were dissected out of the egg, washed in PBS several times, staged, and fixed with 4% paraformaldehyde overnight at 4°C.

Immunostaining, clearing, and imaging of GFP somite graft embryos

Embryos were processed with a standard iDISCO+ protocol (68). Fixed embryos were washed three times in PBS for 30min, dehydrated in a methanol/water gradient (20, 40, 60, 80, 100, 100%) for 1hr each, chilled at 4°C, and bleached in 5% H2O2 in methanol overnight at 4°C. Embryos were then rehydrated in a methanol/water gradient (80, 60, 40, 20%), washed in PBS and twice in PBS with 0.2% Triton X-100 (PTx.2) for 1hr at room temperature. Next, samples were incubated in a permeabilization solution (400ml PTx.2 supplemented with 11.5g glycine and 100ml DMSO) for 2 days in 37°C, transferred to a blocking solution (42ml PTx.2 supplemented with 3ml goat serum and 5ml DMSO) for 2 days at 37°C, then incubated in a primary antibody solution (PTx.2 supplemented with 10μg/ml Heparin (Sigma-Aldrich; PTwH),

5% DMSO, 3% goat serum, and 1:400 rabbit anti-GFP (Invitrogen, A-11122)) for 4 days at 37°C. Embryos were washed 5 times in PTwH overnight, incubated in secondary antibody solution (PTwH supplemented with 3% goat serum, 1:1000 goat anti-rabbit Alexa Fluor 647 (Invitrogen, A-21245)) for 4 days in 37°C, again washed 5 times in PTwH overnight, and incubated in PTwH supplemented with 1:1000 Hoechst33342 (Invitrogen) for 2 days at room temperature. The upper part of the head and the lower half of the body were removed by dissection, and the embryos were embedded in 1-2% agarose. The agarose cube with the embryo was dehydrated in a series of methanol/water gradients (20, 40, 60, 80, 100, 100%) for 1hr each, incubated in 66% dichloromethane/33% methanol solution for 3hr on a shaker, washed in 100% dichloromethane twice, and incubated in dibenzyl ether. The cleared embryos were imaged with a LaVision Ultramicroscope II (Neurobiology Imaging Facility, Harvard Medical School).

3D imaging and cardiac analysis

3D reconstructions and analysis were performed using Imaris software (Bitplane). For GFP signal analysis, systematic virtual sections were generated through each cardiac structure (right and left ventricles, right and left atria, right and left sinus venosus, aorta, pulmonary artery) and compared with the symmetric counterpart when applicable. For 3D rendering, each cardiac chamber was manually segmented. GFP signal within segmented regions was extracted using the Mask Channel function and surfaces were reconstructed from the extracted channel.

Cardiac phenotyping

Cardiac anatomy was assessed on 3D reconstructions following the sequential segmental approach recommended by the International Paediatric and Congenital Cardiac Code (IPCCC)

and ICD-11 nomenclature (69). Each segment was systematically evaluated: cardiac position in the thorax, systemic veins, atria, atrial septation, atrioventricular valves, ventricles (morphology, loop, and hypoplasia), ventricular septation, arterial valve position, and great artery anatomy (pulmonary artery and aorta). For each sample, the Hamburger–Hamilton stage was recorded, and findings were compared with a stage-matched control to account for developmental processes still ongoing before HH34, such as ventricular septation and aortic wedging, which are incomplete at HH31.

Immunostaining of chick embryo sections

Chick embryos with GFP somites were fixed in 4% paraformaldehyde, washed in PBS, and processed by the Pathology Cores (Brigham and Women's Hospital) to obtain paraffin sections (5μm). Sections were incubated at 60°C for 30-60min to melt paraffin, washed 2-3 times in xylene for 5min each, and rehydrated with ethanol/water series (100% x 3 times, 95% x 2 times, 80% x 2 times, 70% x 2 times, water x 2times) for 2-3min each. Next, antigen retrieval was performed in a citric-acid-based antigen unmasking solution (Vector Laboratories) diluted 1:100 in water using a pressure cooker, followed by rinsing 3 times in PBS. Sections were incubated in PBS with 0.5% Triton X-100 for 6min, rinsed 2 times in PBS, and bleached in 3% H2O2 in PBS for 10min. A hydrophobic barrier pen was used to draw a barrier around the sections, and the sections were horizontally positioned to apply a blocking solution (PBS with 0.1% Triton X-100, 3% goat serum) for 1hr at room temperature and then a primary antibody solution (blocking solution with primary antibody) overnight at 4°C. Next the sections were washed 3 times in PBS with 0.1% Tween 20 for 5min in a staining chamber, placed horizontally again to apply a secondary antibody solution (blocking solution with secondary antibody and

Hoechst33342), and again washed 3 times in PBS with 0.1% Tween 20 for 5min in staining chamber, followed by incubation in PBS.

For imaging, Fluoromount-G mounting medium (SouthernBiotech) was applied and covered with a cover slip, followed by sealing with nail polish. Sections were imaged with a Zeiss LSM880 confocal microscope (NeuroTechnology Studio, Brigham and Women's Hospital).

For GFP somite graft on day 2, embryos were washed in PBS, incubated in PBS with 7.5% sucrose for 2hr and then in PBS with 15% sucrose overnight at 4°C. The embryos were incubated in PBS with 7.5% gelatin and 15% sucrose for 2hr at 42°C, placed in molds, and frozen in a dry ice/ethanol bath to obtain cryosections (18µm). Sections were dried for 30min at room temperature, incubated in PBS at 42°C to melt the gelatin, and then in a blocking solution (PBS with 0.1% Triton X-100, 0.2% bovine serum albumin (Sigma-Aldrich)) for 4hr. Sections were kept in a primary antibody solution (blocking solution with primary antibody) overnight at 4°C, washed 3 times for 1hr, incubated in a secondary antibody solution (blocking solution with secondary antibody) for 2hr at room temperature, and again washed 3 times for 15min.

The antibodies used are listed in **Table.3.2**.

Table.3.2. Primary antibodies for immunostaining

Antibody	Species	Type	Source	Catalog #	Dilution
SOX9	Rabbit	Polyclonal	Chemicon	AB5535	1:500
FluoTag-X4 anti-GFP	Alpaca	Single-domain	NanoTag	N0304-At488-L	1:250
PAX7	Mouse	Monoclonal	DSHB	PAX7-c	1:100
GFP	Rabbit	Polyclonal	Invitrogen	A-11122	1:400
ACTA2	Mouse	Monoclonal	Sigma-Aldrich	A2547	1:400

Cytokeratin	Mouse	Multiclonal	Abcam	Ab86734	1:100
RFP	Rabbit	Polyclonal	Rockland	600-401-379	1:400

Electroporation

Wildtype chick embryos at the 5-9-somite stage were used for electroporation. 2-3ml of clear albumen was removed, and the eggs were windowed in an orientation, in which the long axis was parallel to the ground. A few drops of PBS with calcium chloride and magnesium chloride (Sigma-Aldrich; PBS) supplemented with 1% penicillin-streptomycin (Gibco; 100units/ml penicillin, 100µg/ml streptomycin) were applied to the embryo. A solution of 1% Fast Green (Sigma-Aldrich) diluted in PBS was injected into the yolk to visualize the embryo. After gently rupturing the vitelline membrane above the somites, a cocktail containing plasmids for fate mapping was injected into the somitocoel of a single somite using a mouth pipette and a pulled glass capillary. The injection cocktail consisted of 1% Fast Green (Sigma-Aldrich), 6% sucrose, ~2.8µg/µl CAGGS:mbTomato (which ubiquitously expresses membrane-bound red fluorescent protein and is flanked by Tol2 sequences), and ~1µg/µl CAGGS:Transposase (which ubiquitously expresses transposase) (44). Electroporated cells were expected to integrate CAGGS:mbTomato into the genome and to stably express the membrane-bound fluorophore. The (+) and (-) electrodes were positioned to specifically target the lateral side of the injected somite, such that the (+) electrode was positioned lateral to the injected somite with the (-) electrode on the opposite side of the embryo. Three poring pulses of 20-30V, 10msec pulse length, 50msec pulse interval, and 40% decay rate were used. Electroporated eggs were sealed with tape and incubated for 7 days at 37°C and 60% humidity. After incubation, embryos were

dissected out of the egg, washed in PBS several times, staged, and fixed with 4% paraformaldehyde overnight at 4°C.

The same staining, clearing, and imaging procedures were used, as for the GFP somite graft experiments. For immunostaining, 1:400 rabbit anti-RFP primary antibody (Rockland) and 1:1000 goat anti-rabbit Alexa Fluor 647 secondary antibody (Invitrogen, A-21245) were used.

REFERENCES

1. Levin M, Johnson RL, Stern CD, Kuehn M, Tabin C. A molecular pathway determining left-right asymmetry in chick embryogenesis. Cell. 1995 Sep 8;82(5):803–14. doi:10.1016/0092-8674(95)90477-8

2. Gros J, Feistel K, Viebahn C, Blum M, Tabin CJ. Cell Movements at Hensen's Node Establish Left/Right Asymmetric Gene Expression in the Chick. Science. 2009 May 15;324(5929):941–4. doi:10.1126/science.1172478

3. Cui C, Little CD, Rongish BJ. Rotation of organizer tissue contributes to left-right asymmetry. Anat Rec (Hoboken). 2009 Apr;292(4):557–61. doi:10.1002/ar.20872 PubMed PMID: 19301278; PubMed Central PMCID: PMC2714534.

4. Nonaka S, Tanaka Y, Okada Y, Takeda S, Harada A, Kanai Y, et al. Randomization of Left–Right Asymmetry due to Loss of Nodal Cilia Generating Leftward Flow of Extraembryonic Fluid in Mice Lacking KIF3B Motor Protein. Cell. 1998 Dec 11;95(6):829–37. doi:10.1016/S0092-8674(00)81705-5

5. Kawakami Y, Raya Á, Raya RM, Rodríguez-Esteban C, Belmonte JCI. Retinoic acid signalling links left–right asymmetric patterning and bilaterally symmetric somitogenesis in the zebrafish embryo. Nature. 2005 May;435(7039):7039. doi:10.1038/nature03512

6. Logan M, Pagán-Westphal SM, Smith DM, Paganessi L, Tabin CJ. The Transcription Factor Pitx2 Mediates Situs-Specific Morphogenesis in Response to Left-Right Asymmetric Signals. Cell. 1998 Aug 7;94(3):307–17. doi:10.1016/S0092-8674(00)81474-9

7. Ryan AK, Blumberg B, Rodriguez-Esteban C, Yonei-Tamura S, Tamura K, Tsukui T, et al. Pitx2 determines left–right asymmetry of internal organs in vertebrates. Nature. 1998 Aug;394(6693):6693. doi:10.1038/29004

8. Yoshioka H, Meno C, Koshiba K, Sugihara M, Itoh H, Ishimaru Y, et al. Pitx2, a Bicoid-Type Homeobox Gene, Is Involved in a Lefty-Signaling Pathway in Determination of Left-Right Asymmetry. Cell. 1998 Aug 7;94(3):299–305. doi:10.1016/S0092-8674(00)81473-7

9. Esteban CR, Capdevila J, Economides AN, Pascual J, Ortiz Á, Belmonte JCI. The novel Cer-like protein Caronte mediates the establishment of embryonic left–right asymmetry. Nature. 1999 Sep;401(6750):6750. doi:10.1038/45738

10. Yokouchi Y, Vogan KJ, Pearse RV, Tabin CJ. Antagonistic Signaling by Caronte, a Novel Cerberus-Related Gene, Establishes Left–Right Asymmetric Gene Expression. Cell. 1999 Sep 3;98(5):573–83. doi:10.1016/S0092-8674(00)80045-8

11. Negretti MI, Böse N, Petri N, Kremnyov S, Tsikolia N. Nodal asymmetry and hedgehog signaling during vertebrate left–right symmetry breaking. Front Cell Dev Biol. 2022 Sep

12;10:957211. doi:10.3389/fcell.2022.957211 PubMed PMID: 36172285; PubMed Central PMCID: PMC9511907.

12. Pagán-Westphal SM, Tabin CJ. The Transfer of Left-Right Positional Information during Chick Embryogenesis. Cell. 1998 Apr 3;93(1):25–35. doi:10.1016/S0092-8674(00)81143-5

13. Rodrigues S, Santos J, Palmeirim I. Molecular characterization of the rostral-most somites in early somitic stages of the chick embryo. Gene Expression Patterns. 2006 Oct 1;6(7):673–7. doi:10.1016/j.modgep.2006.01.004

14. Maschner A, Krück S, Draga M, Pröls F, Scaal M. Developmental dynamics of occipital and cervical somites. J Anat. 2016 Nov;229(5):601–9. doi:10.1111/joa.12516 PubMed PMID: 27380812; PubMed Central PMCID: PMC5055085.

15. Borman WH, Yorde DE. Analysis of chick somite myogenesis by in situ confocal microscopy of desmin expression. J Histochem Cytochem. 1994 Feb 1;42(2):265–72. doi:10.1177/42.2.8288867

16. Borman WH, Urlakis JR. KJ, Yorde DE. Analysis of the in vivo myogenic status of chick somites by desmin expression in vitro. Developmental Dynamics. 1994;199(4):268–79. doi:10.1002/aja.1001990403

17. Hamburger V, Hamilton HL. A series of normal stages in the development of the chick embryo. J Morphol. 1951 Jan;88(1):49–92. doi:10.1002/jmor.1050880104

18. Reijntjes S, Stricker S, Mankoo BS. A comparative analysis of <I>Meox1</I> and <I>Meox2</I> in the developing somites and limbs of the chick embryo. The International Journal of Developmental Biology. 2007 Oct 1;51(8):753–9. doi:10.1387/ijdb.072332sr

19. Nagai H, Sezaki M, Bertocchini F, Fukuda K, Sheng G. HINTW, a W-chromosome HINT gene in chick, is expressed ubiquitously and is a robust female cell marker applicable in intraspecific chimera studies. genesis. 2014;52(5):424–30. doi:10.1002/dvg.22769

20. Haack TB, Rolinski B, Haberberger B, Zimmermann F, Schum J, Strecker V, et al. Homozygous missense mutation in BOLA3 causes multiple mitochondrial dysfunctions syndrome in two siblings. Journal of Inherited Metabolic Disease. 2013;36(1):55–62. doi:10.1007/s10545-012-9489-7

21. Iijima H, Imai-Okazaki A, Kishita Y, Sugiura A, Shimura M, Murayama K, et al. Role of BOLA3 in the mitochondrial Fe-S cluster clarified by metabolomic analysis. Molecular Genetics and Metabolism. 2025 Jun 1;145(2):109113. doi:10.1016/j.ymgme.2025.109113

22. Yokouchi Y, Vogan KJ, Pearse RV, Tabin CJ. Antagonistic Signaling by Caronte, a Novel Cerberus-Related Gene, Establishes Left–Right Asymmetric Gene Expression. Cell. 1999 Sep 3;98(5):573–83. doi:10.1016/S0092-8674(00)80045-8

23. Cooney CA, Jousheghany F, Yao-Borengasser A, Phanavanh B, Gomes T, Kieber-Emmons AM, et al. Chondroitin sulfates play a major role in breast cancer metastasis: a role for CSPG4 and CHST11gene expression in forming surface P-selectin ligands in aggressive breast cancer cells. Breast Cancer Res. 2011 Jun 9;13(3):R58. doi:10.1186/bcr2895

24. Cambier S, Gouwy M, Proost P. The chemokines CXCL8 and CXCL12: molecular and functional properties, role in disease and efforts towards pharmacological intervention. Cell Mol Immunol. 2023 Mar;20(3):217–51. doi:10.1038/s41423-023-00974-6

25. Yan H, Parsons DW, Jin G, McLendon R, Rasheed BA, Yuan W, et al. IDH1 and IDH2 Mutations in Gliomas. New England Journal of Medicine. 2009 Feb 19;360(8):765–73. doi:10.1056/NEJMoa0808710

26. Xie W, Xiao H, Luo J, Zhao L, Jin F, Ma J, et al. Identification of low-density lipoprotein receptor class A domain containing 4 (LDLRAD4) as a prognostic indicator in primary gastrointestinal stromal tumors. Current Problems in Cancer. 2020 Dec 1;44(6):100593. doi:10.1016/j.currproblcancer.2020.100593

27. Xu W, Wang M, Bai Y, Chen Y, Ma X, Yang Z, et al. The role of microfibrillar-associated protein 2 in cancer. Front Oncol. 2022 Nov 30;12:1002036. doi:10.3389/fonc.2022.1002036 PubMed PMID: 36530974; PubMed Central PMCID: PMC9748481.

28. Blockus H, Chédotal A. Slit-Robo signaling. Development. 2016 Sep 1;143(17):3037–44. doi:10.1242/dev.132829

29. Kondás K, Szláma G, Trexler M, Patthy L. Both WFIKKN1 and WFIKKN2 Have High Affinity for Growth and Differentiation Factors 8 and 11*. Journal of Biological Chemistry. 2008 Aug 29;283(35):23677–84. doi:10.1074/jbc.M803025200

30. Monestier O, Blanquet V. WFIKKN1 and WFIKKN2: “Companion” proteins regulating TGFB activity. Cytokine & Growth Factor Reviews. 2016 Dec 1;32:75–84. doi:10.1016/j.cytogfr.2016.06.003

31. Janer A, Morris JL, Krols M, Antonicka H, Aaltonen MJ, Lin ZY, et al. ESYT1 tethers the ER to mitochondria and is required for mitochondrial lipid and calcium homeostasis. Life Science Alliance. 2024 Jan 1;7(1). doi:10.26508/lsa.202302335 PubMed PMID: 37931956.

32. Pan L, Sato S, Frederick JP, Sun XH, Zhuang Y. Impaired Immune Responses and B-Cell Proliferation in Mice Lacking the Id3 Gene. Mol Cell Biol. 1999 Sep;19(9):5969–80. doi:10.1128/mcb.19.9.5969 PubMed PMID: 10454544; PubMed Central PMCID: PMC84466.

33. Patel K, Isaac A, Cooke J. Nodal signalling and the roles of the transcription factors SnR and Pitx2 in vertebrate left–right asymmetry. Current Biology. 1999 Jun 3;9(11):609-S1. doi:10.1016/S0960-9822(99)80267-X

34. Barrallo-Gimeno A, Nieto MA. The Snail genes as inducers of cell movement and survival: implications in development and cancer. Development. 2005 Jul 15;132(14):3151–61. doi:10.1242/dev.01907

35. Kuratani SC, Kirby ML. Initial migration and distribution of the cardiac neural crest in the avian embryo: An introduction to the concept of the circumpharyngeal crest. American Journal of Anatomy. 1991;191(3):215–27. doi:10.1002/aja.1001910302

36. Kirby ML, Hutson MR. Factors controlling cardiac neural crest cell migration. Cell Adhesion & Migration. 2010 Oct 1;4(4):609–21. doi:10.4161/cam.4.4.13489 PubMed PMID: 20890117.

37. Rezzoug F, Seelan RS, Bhattacherjee V, Greene RM, Michele Pisano M. Chemokine-mediated migration of mesencephalic neural crest cells. Cytokine. 2011 Dec 1;56(3):760–8. doi:10.1016/j.cyto.2011.09.014

38. Jiang Y, Liu M tsai, Gershon MD. Netrins and DCC in the guidance of migrating neural crest-derived cells in the developing bowel and pancreas. Developmental Biology. 2003 Jun 15;258(2):364–84. doi:10.1016/S0012-1606(03)00136-2

39. Couly GF, Coltey PM, Le Douarin NM. The triple origin of skull in higher vertebrates: a study in quail-chick chimeras. Development. 1993 Feb 1;117(2):409–29. doi:10.1242/dev.117.2.409

40. Huang R, Zhi Q, Patel K, Wilting J, Christ B. Contribution of single somites to the skeleton and muscles of the occipital and cervical regions in avian embryos. Anat Embryol. 2000 Oct 1;202(5):375–83. doi:10.1007/s004290000131

41. Chapman SC, Lawson A, Macarthur WC, Wiese RJ, Loechel RH, Burgos-Trinidad M, et al. Ubiquitous GFP expression in transgenic chickens using a lentiviral vector. Development. 2005 Mar;132(5):935–40. doi:10.1242/dev.01652 PubMed PMID: 15673573.

42. Redkar A, Montgomery M, Litvin J. Fate map of early avian cardiac progenitor cells. Development. 2001 Jun 15;128(12):2269–79. doi:10.1242/dev.128.12.2269

43. Wolton M, Davey MG, Dietrich S. At early stages of heart development, the first and second heart fields are a continuum of lateral head mesoderm-derived, cardiogenic cells. Developmental Biology. 2025 Apr 1;520:200–23. doi:10.1016/j.ydbio.2025.01.009

44. Toulouse G, Jarassier W, Jagot S, Morin V, Le Grand F, Marcelle C. Early lineage segregation of primary myotubes from secondary myotubes and adult muscle stem cells. Nat Commun. 2025 Aug 22;16(1):7858. doi:10.1038/s41467-025-61767-1

45. Kubota Y, Morita T, Kusakabe M, Sakakura T, Ito K. Spatial and temporal changes in chondroitin sulfate distribution in the sclerotome play an essential role in the formation of migration patterns of mouse neural crest cells. Dev Dyn. 1999 Jan;214(1):55–65.

doi:10.1002/(SICI)1097-0177(199901)214:1<55::AID-DVDY6>3.0.CO;2-E PubMed PMID: 9915576.

46. Solovieva T, Bronner ME. Congenital heart defects differ following left versus right avian cardiac neural crest ablation. Dev Biol. 2025 Mar;519:30–7. doi:10.1016/j.ydbio.2024.12.003 PubMed PMID: 39667652; PubMed Central PMCID: PMC11768310.

47. Meilhac SM, Buckingham ME. The deployment of cell lineages that form the mammalian heart. Nat Rev Cardiol. 2018 Nov;15(11):705–24. doi:10.1038/s41569-018-0086-9

48. Desgrange A, Le Garrec JF, Meilhac SM. Left-right asymmetry in heart development and disease: forming the right loop. Development. 2018 Nov 22;145(22):dev162776. doi:10.1242/dev.162776

49. Desgrange A, Le Garrec JF, Bernheim S, Bønnelykke TH, Meilhac SM. Transient Nodal Signaling in Left Precursors Coordinates Opposed Asymmetries Shaping the Heart Loop. Developmental Cell. 2020 Nov 23;55(4):413-431.e6. doi:10.1016/j.devcel.2020.10.008

50. Le Garrec JF, Domínguez JN, Desgrange A, Ivanovitch KD, Raphaël E, Bangham JA, et al. A predictive model of asymmetric morphogenesis from 3D reconstructions of mouse heart looping dynamics. Harvey RP, editor. eLife. 2017 Nov 28;6:e28951. doi:10.7554/eLife.28951

51. Kelly RG, Brown NA, Buckingham ME. The Arterial Pole of the Mouse Heart Forms from Fgf10-Expressing Cells in Pharyngeal Mesoderm. Developmental Cell. 2001 Sep 1;1(3):435–40. doi:10.1016/S1534-5807(01)00040-5

52. Tyser RCV, Ibarra-Soria X, McDole K, Jayaram SA, Godwin J, van den Brand TAH, et al. Characterization of a common progenitor pool of the epicardium and myocardium. Science. 2021 Mar 5;371(6533):eabb2986. doi:10.1126/science.abb2986 PubMed PMID: 33414188; PubMed Central PMCID: PMC7615359.

53. Schulte I, Schlueter J, Abu-Issa R, Brand T, Männer J. Morphological and molecular left–right asymmetries in the development of the proepicardium: A comparative analysis on mouse and chick embryos. Developmental Dynamics. 2007;236(3):684–95. doi:10.1002/dvdy.21065

54. Kirby ML, Gale TF, Stewart DE. Neural Crest Cells Contribute to Normal Aorticopulmonary Septation. Science. 1983 Jun 3;220(4601):1059–61. doi:10.1126/science.6844926

55. Etchevers HC, Vincent C, Douarin NML, F. Couly G. The cephalic neural crest provides pericytes and smooth muscle cells to all blood vessels of the face and forebrain. Development. 2001 Apr 1;128(7):1059–68. doi:10.1242/dev.128.7.1059

56. Esner M, Meilhac SM, Relaix F, Nicolas JF, Cossu G, Buckingham ME. Smooth muscle of the dorsal aorta shares a common clonal origin with skeletal muscle of the myotome. Development. 2006 Feb 15;133(4):737–49. doi:10.1242/dev.02226

57. Pouget C, Pottin K, Jaffredo T. Sclerotomal origin of vascular smooth muscle cells and pericytes in the embryo. Developmental Biology. 2008 Mar 15;315(2):437–47. doi:10.1016/j.ydbio.2007.12.045

58. Le Lièvre CS, Le Douarin NM. Mesenchymal derivatives of the neural crest: analysis of chimaeric quail and chick embryos. J Embryol Exp Morphol. 1975 Aug;34(1):125–54. PubMed PMID: 1185098.

59. Matsuoka T, Ahlberg PE, Kessaris N, Iannarelli P, Dennehy U, Richardson WD, et al. Neural Crest Origins of the Neck and Shoulder. Nature. 2005 Jul 21;436(7049):347–55. doi:10.1038/nature03837 PubMed PMID: 16034409; PubMed Central PMCID: PMC1352163.

60. Wasteson P, Johansson BR, Jukkola T, Breuer S, Akyürek LM, Partanen J, et al. Developmental origin of smooth muscle cells in the descending aorta in mice. Development. 2008 May 15;135(10):1823–32. doi:10.1242/dev.020958

61. Lescroart F, Kelly RG, Le Garrec JF, Nicolas JF, Meilhac SM, Buckingham M. Clonal analysis reveals common lineage relationships between head muscles and second heart field derivatives in the mouse embryo. Development. 2010 Oct 1;137(19):3269–79. doi:10.1242/dev.050674

62. Lescroart F, Hamou W, Francou A, Théveniau-Ruissy M, Kelly RG, Buckingham M. Clonal analysis reveals a common origin between nonsomite-derived neck muscles and heart myocardium. Proceedings of the National Academy of Sciences. 2015 Feb 3;112(5):1446–51. doi:10.1073/pnas.1424538112

63. van de Putte R, van Rooij IALM, Marcelis CLM, Guo M, Brunner HG, Addor MC, et al. Spectrum of congenital anomalies among VACTERL cases: a EUROCAT population-based study. Pediatr Res. 2020 Feb;87(3):541–9. doi:10.1038/s41390-019-0561-y

64. Aubert-Mucca M, Janel C, Porquet-Bordes V, Patat O, Touraine R, Edouard T, et al. Clinical heterogeneity of NADSYN1-associated VCRL syndrome. Clinical Genetics. 2023;104(1):114–20. doi:10.1111/cge.14328

65. Herrera-Soto JA, Vander Have KL, Barry-Lane P, Myers JL. Retrospective Study on the Development of Spinal Deformities Following Sternotomy for Congenital Heart Disease. Spine. 2007 Aug 15;32(18):1998. doi:10.1097/BRS.0b013e318131b225

66. Schlösser TPC, Semple T, Carr SB, Padley S, Loebinger MR, Hogg C, et al. Scoliosis convexity and organ anatomy are related. Eur Spine J. 2017 Jun 1;26(6):1595–9. doi:10.1007/s00586-017-4970-5

67. Chapman SC, Collignon J, Schoenwolf GC, Lumsden A. Improved method for chick whole-embryo culture using a filter paper carrier. Developmental Dynamics. 2001;220(3):284–9. doi:10.1002/1097-0177(20010301)220:3<284::AID-DVDY1102>3.0.CO;2-5

68. Renier N, Adams EL, Kirst C, Wu Z, Azevedo R, Kohl J, et al. Mapping of Brain Activity by Automated Volume Analysis of Immediate Early Genes. Cell. 2016 Jun 16;165(7):1789–802. doi:10.1016/j.cell.2016.05.007 PubMed PMID: 27238021.

69. Franklin RCG, Béland MJ, Colan SD, Walters HL, Aiello VD, Anderson RH, et al. Nomenclature for congenital and paediatric cardiac disease: the International Paediatric and Congenital Cardiac Code (IPCCC) and the Eleventh Iteration of the International Classification of Diseases (ICD-11). Cardiol Young. 2017 Dec;27(10):1872–938. doi:10.1017/S1047951117002244 PubMed PMID: 29286277.

Chapter 4

Conclusion

During my Ph.D., I aimed to understand how bilateral symmetry in the paraxial mesoderm is regulated. Biologists have long investigated the mechanisms by which initial symmetry breaking occurs at the embryonic organizer as well as the molecular circuits conferring lateralized tissue identity in the lateral plate mesoderm (1–3). Yet the paraxial mesoderm has been largely overlooked in traditional research on LR asymmetry.

This project was launched by initially asking how the bilateral symmetry is maintained in the paraxial mesoderm, with the goal of identifying mechanisms that correct fluctuating asymmetry of somites. Soon it became clear that without thorough characterization of somite bilateral symmetry, it would be extremely difficult to understand how symmetry is achieved. Therefore, I decided to quantitatively and systematically measure somite bilateral symmetry in chick embryos, with the goal of capturing the developmental window or molecular steps over which symmetry is enhanced. The growing awareness of the field that somite bilateral symmetry is not the default state and that somitogenesis occurs amid various sources of asymmetry was a critical motivation to this goal (4–7).

I analyzed asymmetry in somite AP boundary position and in somite volume and demonstrated that the anterior-most somites are morphologically asymmetric in a lateralized manner and that gene expression underlying somitogenesis shows corresponding directional asymmetry. Experiments perturbing the LR determination pathway showed that this directional asymmetry in the paraxial mesoderm is indeed downstream of LR determining signals and that the NODAL signaling pathway modulates somitogenesis in an asymmetric manner. The human iPSC differentiation protocol developed by our lab was instrumental in clearly demonstrating the effect of the NODAL signaling pathway on somitogenesis, as the addition of NODAL protein to posterior-PSM-like cells accelerated clock gene oscillations (8). Moreover, this NODAL-

mediated acceleration of somitogenesis dynamics was specific to conditions of RA inhibition, a finding that aligns well with the classic works on the role of RA in somite bilateral symmetry (4–6). As such, by modeling the interaction between the RA and NODAL signaling pathways, this system allowed us to revisit classic findings on somite bilateral symmetry and suggest at least one concrete function of RA in regulating somite bilateral asymmetry.

The findings in the chick embryo and human iPSCs indicated that the early paraxial mesoderm is exposed to an asymmetric signaling environment that not only asymmetrically modulates somitogenesis dynamics but also can drive molecular asymmetry between the left and right paraxial mesoderm. Moreover, the experiments perturbing LR determination allowed us to revisit *NODAL* expression dynamics, which showed clear expression in the lateral parts of the anterior somites. While *NODAL* expression in the lateral parts of anterior somites was not previously known, this finding extends reports of transient molecular asymmetry in the paraxial mesoderm of the chick embryo, such as *NODAL* in the anterior PSM and *CER1* in the paraxial mesoderm during NODAL induction in the lateral plate mesoderm (LPM) (2,9–11). Thus, we decided to investigate the molecular asymmetry of the paraxial mesoderm in the chick embryo with a side-specific single-cell RNA sequencing experiment. This approach uncovered extensive molecular asymmetry of early chick embryo undergoing LR determination, identifying novel asymmetric genes in a tissue-specific manner. These genes demonstrated lasting asymmetric expression, making them promising candidates as downstream effectors of LR asymmetric development.

The validation of molecular asymmetry in the paraxial mesoderm motivated us to investigate its developmental consequences. First, as various genes involved in neural crest (NC) migration regulation are asymmetrically expressed, we showed that cardiac neural crest cell

(CNCC) migration was potentially lateralized, suggesting a possible non-autonomous contribution of asymmetric somites to LR asymmetric development. Moreover, through an extensive side-specific GFP somite graft experiment, we revisited the fate of occipital somites and identified a robust contribution of anterior somites to the heart in addition to other known derivatives of somites (12,13). The contribution of occipital somite cells to the heart was independently validated in a second fate map experiment, in which the lateral parts of the occipital somites were electroporated to stably express membrane-bound dTomato (14). Importantly, we further demonstrated that the modulation of molecular laterality specifically in grafted anterior somites can alter the fate contribution of somites and affect proper cardiac development. This finding provides strong evidence that anterior somites are direct, functionally relevant contributors to LR asymmetric organogenesis.

As such, my thesis challenges the traditional view of somites as bilaterally symmetric structures and reveals previously overlooked dimensions of lateralized asymmetry in the early-stage embryo. Importantly, LR asymmetry in the early embryo is not confined to Hensen's node (HN), the LPM, and the heart—the embryonic structures long regarded as the earliest signatures of vertebrate handedness (15)—but extends to the paraxial mesoderm, as demonstrated by its morphological and molecular asymmetries. Thus, our findings point to previously unrecognized domains of vertebrate LR asymmetry. This perspective is consistent with recent findings showing asymmetric developmental outcomes of left and right CNCC ablation (16).

One of the most striking findings of my thesis is that occipital somites contribute to the heart in a lateralized manner and that their molecular laterality is important for proper cardiac development. Somites have been described to contribute to various cell types of vasculature including endothelium and smooth muscle (17–19). Also, *Meox1-Cre*-based lineage tracing in

the mouse showed reporter gene expression in the arterial pole of the heart (20). Therefore, our finding that anterior somites contribute to the heart expands the traditional fate map of somites and is consistent with these observations in the mouse. Moreover, our finding may be relevant to single-cell RNA sequencing studies of E6.5-8.5 mouse embryos, which identified distinct transcriptional trajectories for the anterior-most versus more posterior somites (21). In that study, the trajectory of the anterior-most somites was marked by elevated expression of lateral plate mesoderm markers, and these somites were proposed to share developmental origins with other anterior mesodermal tissues, including cardiac and cranial mesoderm (21,22). This model is consistent with our own characterization of the lateral parts of the anterior somites, which contribute to the heart and display a mixed transcriptional identity with intermediate expression of both paraxial and LPM markers. Thus, the anterior somite trajectory described in early mouse embryos may correspond, at least in part, to the unique developmental properties of the lateral anterior somites identified here.

An important remaining question is how asymmetries in morphology, transcriptional profile, and developmental fate are mechanistically connected. Our GFP somite graft experiments, in which molecular laterality was experimentally modulated, clearly establish a link between somite molecular asymmetry and the lateralized fate map. However, the molecular mechanisms by which side-specific transcriptional programs govern fate contribution remain unclear. It is also not yet known whether the morphological asymmetries of occipital somites are functionally linked to their asymmetric developmental fates. In particular, the fact that left occipital somites are larger and more anteriorly positioned than the right raises the possibility that these morphological asymmetries may contribute to the asymmetric fate contribution of occipital somites, especially given that the more anteriorly positioned left somites contribute to

the arterial pole of the heart. Addressing this question will require fate map experiments that carefully track somite cells across multiple developmental stages. Another possible explanation lies in asymmetric BMP signaling. BMP signaling is critical for specification of lateral fates, including LPM and lateral somite identity (23–25), yet it is asymmetrically antagonized on the left side, where CER1-mediated BMP inhibition is necessary for NODAL induction in the left LPM (2,9). It is therefore possible that the left and right anterior mesoderm experience different degrees of lateralization and that this difference contributes to asymmetry in developmental fate as well as in somite volume.

An interesting question that this project did not examine is the achievement of bilateral symmetry. The quantification of asymmetry in somite AP boundary position and gene expression underlying somitogenesis suggests that this asymmetry is most pronounced in early stages and likely resolves toward symmetry over development. This means that asymmetry in both the already asymmetrically formed somites and the formation process of nascent somites is attenuated. An approach that allows detailed and extended tracking of asymmetry in somite morphology and in underlying gene expression—such as, time-lapse imaging coupled with a live-reporter of clock gene oscillation in the chick embryo—would be instrumental for addressing this exciting question.

Another remaining question of this project is the molecular mechanisms by which the NODAL signaling pathway accelerates segmentation clock gene oscillation and by which RA buffers this NODAL-mediated acceleration. Mouse mutants and zebrafish morphants that lack the RA-synthesizing enzyme RALDH2 show asymmetric expansion of the FGF gradient on the right side, suggesting that posterior-PSM identity is likely a target of modulation by LR-determining signals (5,26). Yet qPCR experiments with human posterior-PSM-like cells did not

exhibit consistent alteration of posterior PSM identity upon NODAL treatment. Curiously, in the early chick embryo during the formation of occipital somites, posterior PSM markers *MSGN1* and *FGF8* demonstrated more anteriorly expanded expression pattern on the left side, but modulation of LR determination with a SAG bead did not alter *MSGN1* asymmetry. Moreover, lateralized expansion of posterior PSM identity was not reported in chick embryos with pharmacological inhibition of the RA pathway with disulfiram (4). Thus, it would be interesting to further investigate the molecular mechanisms by which NODAL impacts somitogenesis dynamics in a species-specific manner.

Lastly, the conservation of somite asymmetry delineated by this thesis in different vertebrate organisms is an important question. My thesis showed that at least some features of somite asymmetry are likely conserved, as E8.0 mouse embryos also express *Nodal* in the lateral parts of the anterior somites. Also, our unpublished preliminary data suggest that left anterior somites are larger than the right ones in early mouse embryos (data not shown). Indeed, our quantification strategy for somite AP position asymmetry is not immediately transferrable to mouse and human embryos due to differences in embryonic geometry and/or the scarcity of early samples. Yet, the facts that Amphioxus embryos exhibit clear somite asymmetry and that *Meox1-Cre*-based lineage tracing in the mouse embryo shows labeling in the arterial pole of the heart support a broad conservation of previously unidentified somite asymmetry in different vertebrate species (20,27,28). It remains to be determined to what extent morphological, molecular, and developmental asymmetry in the paraxial mesoderm is conserved.

Overall, my thesis identifies extensive lateralized asymmetry in the anterior somites of the chick embryo, spanning morphology, transcriptional landscape, and developmental fate. This work provides a novel framework to investigate the question of asymmetry in other embryonic

tissues that have traditionally been assumed to be symmetric and a valuable resource to explore previously unrecognized aspects of LR asymmetry. I believe that my thesis research demonstrates that revisiting familiar genes and tissues with different tools and perspectives has the potential to reveal overlooked dimensions of classic biological questions.

REFERENCES

1. Levin M, Johnson RL, Stern CD, Kuehn M, Tabin C. A molecular pathway determining left-right asymmetry in chick embryogenesis. Cell. 1995 Sep 8;82(5):803–14. doi:10.1016/0092-8674(95)90477-8

2. Yokouchi Y, Vogan KJ, Pearse RV, Tabin CJ. Antagonistic Signaling by Caronte, a Novel Cerberus-Related Gene, Establishes Left–Right Asymmetric Gene Expression. Cell. 1999 Sep 3;98(5):573–83. doi:10.1016/S0092-8674(00)80045-8

3. Logan M, Pagán-Westphal SM, Smith DM, Paganessi L, Tabin CJ. The Transcription Factor Pitx2 Mediates Situs-Specific Morphogenesis in Response to Left-Right Asymmetric Signals. Cell. 1998 Aug 7;94(3):307–17. doi:10.1016/S0092-8674(00)81474-9

4. Vermot J, Pourquié O. Retinoic acid coordinates somitogenesis and left–right patterning in vertebrate embryos. Nature. 2005 May;435(7039):7039. doi:10.1038/nature03488

5. Vermot J, Llamas JG, Fraulob V, Niederreither K, Chambon P, Dollé P. Retinoic Acid Controls the Bilateral Symmetry of Somite Formation in the Mouse Embryo. Science. 2005 Apr 22;308(5721):563–6. doi:10.1126/science.1108363

6. Kawakami Y, Raya Á, Raya RM, Rodríguez-Esteban C, Belmonte JCI. Retinoic acid signalling links left–right asymmetric patterning and bilaterally symmetric somitogenesis in the zebrafish embryo. Nature. 2005 May;435(7039):7039. doi:10.1038/nature03512

7. Naganathan SR, Popović M, Oates AC. Left–right symmetry of zebrafish embryos requires somite surface tension. Nature. 2022 May;605(7910):516–21. doi:10.1038/s41586-022-04646-9

8. Diaz-Cuadros M, Wagner DE, Budjan C, Hubaud A, Tarazona OA, Donelly S, et al. In vitro characterization of the human segmentation clock. Nature. 2020 Apr;580(7801):113–8. doi:10.1038/s41586-019-1885-9

9. Esteban CR, Capdevila J, Economides AN, Pascual J, Ortiz Á, Belmonte JCI. The novel Cer-like protein Caronte mediates the establishment of embryonic left–right asymmetry. Nature. 1999 Sep;401(6750):6750. doi:10.1038/45738

10. Negretti MI, Böse N, Petri N, Kremnyov S, Tsikolia N. Nodal asymmetry and hedgehog signaling during vertebrate left–right symmetry breaking. Front Cell Dev Biol. 2022 Sep 12;10:957211. doi:10.3389/fcell.2022.957211 PubMed PMID: 36172285; PubMed Central PMCID: PMC9511907.

11. Pagán-Westphal SM, Tabin CJ. The Transfer of Left-Right Positional Information during Chick Embryogenesis. Cell. 1998 Apr 3;93(1):25–35. doi:10.1016/S0092-8674(00)81143-5 PubMed PMID: 9546389.

12. Couly GF, Coltey PM, Le Douarin NM. The triple origin of skull in higher vertebrates: a study in quail-chick chimeras. Development. 1993 Feb 1;117(2):409–29. doi:10.1242/dev.117.2.409

13. Huang R, Zhi Q, Patel K, Wilting J, Christ B. Contribution of single somites to the skeleton and muscles of the occipital and cervical regions in avian embryos. Anat Embryol. 2000 Oct 1;202(5):375–83. doi:10.1007/s004290000131

14. Toulouse G, Jarassier W, Jagot S, Morin V, Le Grand F, Marcelle C. Early lineage segregation of primary myotubes from secondary myotubes and adult muscle stem cells. Nat Commun. 2025 Aug 22;16(1):7858. doi:10.1038/s41467-025-61767-1

15. Cooke J. Vertebrate embryo handedness. Nature. 1995 Apr;374(6524):681–681. doi:10.1038/374681a0

16. Solovieva T, Bronner ME. Congenital heart defects differ following left versus right avian cardiac neural crest ablation. Dev Biol. 2025 Mar;519:30–7. doi:10.1016/j.ydbio.2024.12.003 PubMed PMID: 39667652; PubMed Central PMCID: PMC11768310.

17. Christ B, Ordahl CP. Early stages of chick somite development. Anat Embryol. 1995 May 1;191(5):381–96. doi:10.1007/BF00304424

18. Esner M, Meilhac SM, Relaix F, Nicolas JF, Cossu G, Buckingham ME. Smooth muscle of the dorsal aorta shares a common clonal origin with skeletal muscle of the myotome. Development. 2006 Feb 15;133(4):737–49. doi:10.1242/dev.02226

19. Pouget C, Pottin K, Jaffredo T. Sclerotomal origin of vascular smooth muscle cells and pericytes in the embryo. Developmental Biology. 2008 Mar 15;315(2):437–47. doi:10.1016/j.ydbio.2007.12.045

20. Wasteson P, Johansson BR, Jukkola T, Breuer S, Akyürek LM, Partanen J, et al. Developmental origin of smooth muscle cells in the descending aorta in mice. Development. 2008 May 15;135(10):1823–32. doi:10.1242/dev.020958

21. Guibentif C, Griffiths JA, Imaz-Rosshandler I, Ghazanfar S, Nichols J, Wilson V, et al. Diverse Routes toward Early Somites in the Mouse Embryo. Dev Cell. 2021 Jan 11;56(1):141-153.e6. doi:10.1016/j.devcel.2020.11.013 PubMed PMID: 33308481; PubMed Central PMCID: PMC7808755.

22. Kinder SJ, Tsang TE, Quinlan GA, Hadjantonakis AK, Nagy A, Tam PPL. The orderly allocation of mesodermal cells to the extraembryonic structures and the anteroposterior axis during gastrulation of the mouse embryo. Development. 1999 Nov 1;126(21):4691–701. doi:10.1242/dev.126.21.4691

23. Pourquié O, Fan CM, Coltey M, Hirsinger E, Watanabe Y, Bréant C, et al. Lateral and Axial Signals Involved in Avian Somite Patterning: A Role for BMP4. Cell. 1996 Feb 9;84(3):461–71. doi:10.1016/S0092-8674(00)81291-X

24. Tonegawa A, Funayama N, Ueno N, Takahashi Y. Mesodermal subdivision along the mediolateral axis in chicken controlled by different concentrations of BMP-4. Development. 1997 May 15;124(10):1975–84. doi:10.1242/dev.124.10.1975

25. Pourquié O, Coltey M, Bréant C, Le Douarin NM. Control of somite patterning by signals from the lateral plate. Proceedings of the National Academy of Sciences. 1995 Apr 11;92(8):3219–23. doi:10.1073/pnas.92.8.3219

26. Kawakami Y, Raya Á, Raya RM, Rodríguez-Esteban C, Belmonte JCI. Retinoic acid signalling links left–right asymmetric patterning and bilaterally symmetric somitogenesis in the zebrafish embryo. Nature. 2005 May;435(7039):7039. doi:10.1038/nature03512

27. Schubert M, Holland LZ, Stokes MD, Holland ND. Three Amphioxus Wnt Genes (AmphiWnt3, AmphiWnt5, and AmphiWnt6) Associated with the Tail Bud: the Evolution of Somitogenesis in Chordates. Developmental Biology. 2001 Dec 1;240(1):262–73. doi:10.1006/dbio.2001.0460

28. Soukup V, Yong LW, Lu TM, Huang SW, Kozmik Z, Yu JK. The Nodal signaling pathway controls left-right asymmetric development in amphioxus. EvoDevo. 2015 Feb 17;6:5. doi:10.1186/2041-9139-6-5 PubMed PMID: 25954501; PubMed Central PMCID: PMC4423147.

Appendix 1

Supplemental data for:

Molecular Asymmetry and Developmental Fate of Anterior Somites

Figure 3.S1. Characterization of somite graft after 48hr

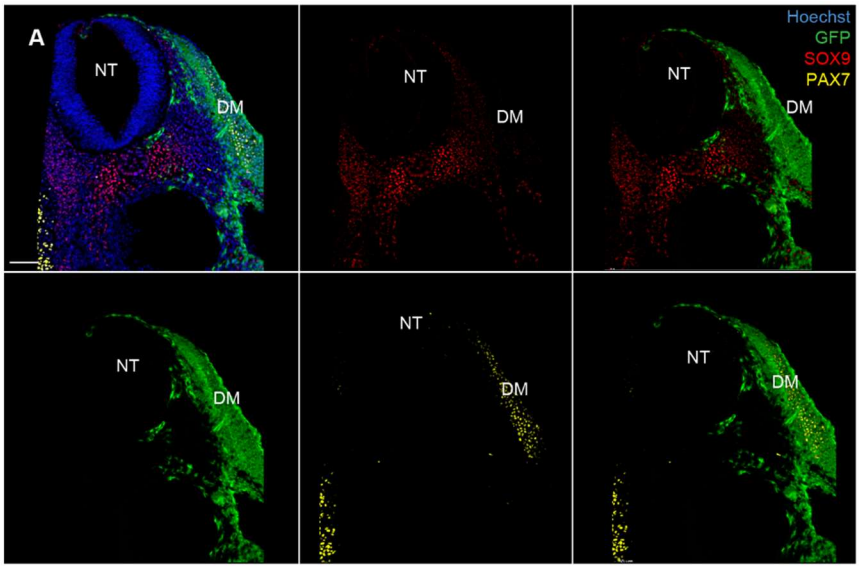

(A) Transverse cryostat section through a GFP-somite-grafted chick embryo collected at HH16 (~48hr post-graft), co-immunostained for GFP (green), SOX9 (red), and PAX7 (yellow). GFP+ cells derived from the graft are distributed across the somite derivatives and overlap with Pax7+ dermomyotomal cells (lower row). Abbreviations: NT, neural tube; DM, dermomyotome. Scale bar = 100µm

Figure 3.S2. Fate map of anterior somites by electroporation

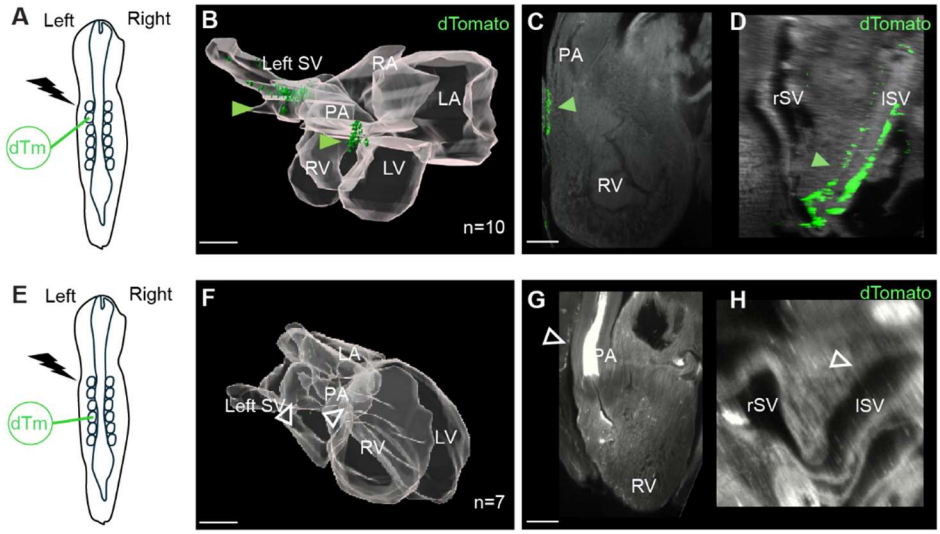

(A–D) Electroporation of the left 2nd somite. (A) A membrane-bound-dTomato-expressing plasmid (mem-dTomato) and transposase-expressing plasmid were injected into the somitocoel of the left 2nd somite at the 5- to 9-somite stage and electroporated on the lateral side. (B) 3D light-sheet reconstruction at HH32–34 after whole-mount RFP immunostaining (green arrowheads). (C,D) Light-sheet sections confirm RFP+ cells at the PA (C) and at the left sinus venosus (lSV, D). (E–H) Electroporation of the left 4th somite. (E) Same procedure applied to the left 4th somite. (F) 3D reconstruction shows the absence of RFP+ signal at the left SV and PA (open white arrowheads). (G,H) Light-sheet sections confirm the absence of RFP+ cells at the PA (G) and at the left SV (H). Abbreviations: RA, right atrium; LA, left atrium; RV, right ventricle; LV, left ventricle; PA, pulmonary artery; SV, sinus venosus (rSV, lSV). Scale bar = 500µm.

Figure 3.S3. Cardiac development and the somitic contribution to the heart are not affected in embryos grafted with cyclopamine-treated right somite and SAG-bead-treated left somite

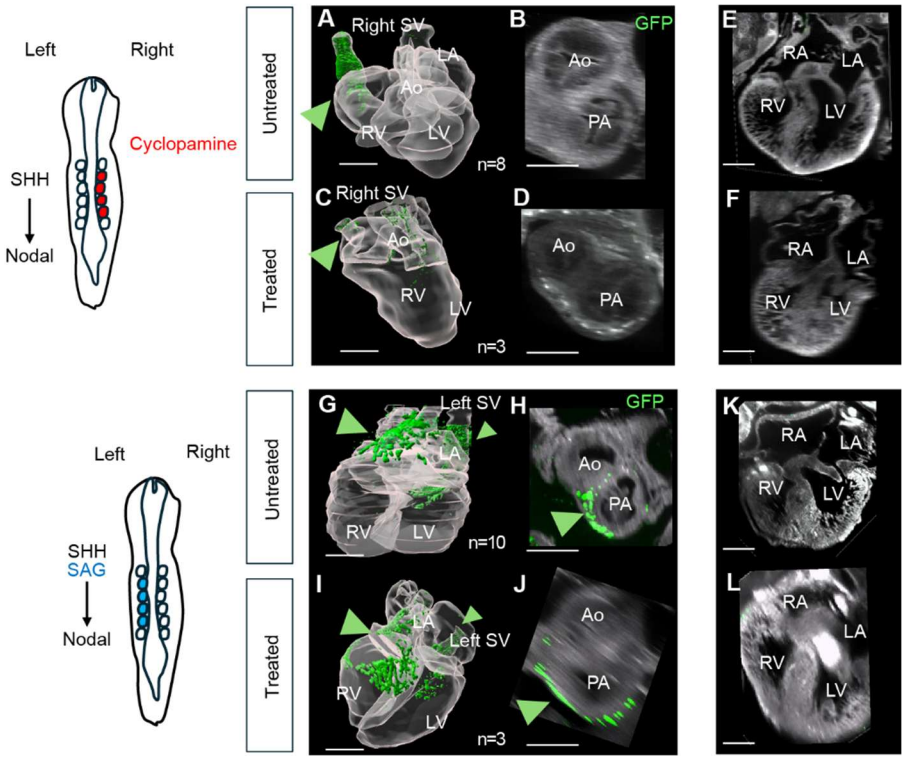

(A–F) Right somite grafts with cyclopamine-treated donor. GFP+ cells contribute to the right sinus venosus in both untreated (A,B) and treated (C,D) conditions, with normal cardiac morphology (E,F). (G–L) Left somite grafts with SAG-bead-treated donor. GFP+ cells contribute to the left sinus venosus and pulmonary artery in both untreated (G,H) and treated (I,J) conditions, with normal cardiac morphology (K,L). Abbreviations: RA, right atrium; LA, left atrium; RV, right ventricle; LV, left ventricle; PA, pulmonary artery; Ao, aorta; SV, sinus venosus. Scale bars = 500μm